2017

# Extending the record of lacustrine phases beyond the last interglacial for Lake Eyre in central Australia using luminescence dating

Xiao Fu
*University of Wollongong*, xiaofu@uow.edu.au

Tim J. Cohen
*University of Wollongong*, tcohen@uow.edu.au

Lee J. Arnold
*University of Adelaide*

## Publication Details

Fu, X., Cohen, T. J. & Arnold, L. J. (2017). Extending the record of lacustrine phases beyond the last interglacial for Lake Eyre in central Australia using luminescence dating. Quaternary Science Reviews: the international multidisciplinary research and review journal, 162 88-110.

# Extending the record of lacustrine phases beyond the last interglacial for Lake Eyre in central Australia using luminescence dating

**Abstract**

We show with multiple luminescence dating techniques that the sedimentary record for Lake Eyre, Australia's largest lake, extends beyond 200 thousand years (ka) to Marine Isotope Stage (MIS) 7. Transgressive clayey sand and finely laminated clays overlying the Miocene Etadunna Formation in Lake Eyre North document the deep-lake phases of central South Australia in the past. Until now, unresolved chronology has hampered our ability to interpret these sedimentary records, which are important for understanding the timing of the wettest phase of central Australia's late Quaternary climate. In this study, we apply quartz optically stimulated luminescence (OSL) dating, thermally-transferred OSL (TT-OSL) dating and K-feldspar post infrared infrared stimulated luminescence (pIRIR) dating to lake-floor sediments near Williams Point in Madigan Gulf to provide new age constraint for the lacustrine sediments of Lake Eyre. Methodological studies on quartz and K-feldspar demonstrate that these luminescence dating procedures are suitable for the Lake Eyre lacustrine samples and produce consistent replicate ages. A Bayesian model applied to the new dating results provides a chronological model of lacustrine deposition and shows that the transgressive clayey sand were deposited 221 ± 19 ka to 201 ± 10 ka and that the deep-water sediments were laid down in early MIS 6 (191 ± 9 ka to 181 ± 9 ka). We also find evidence for a potential depositional hiatus in mid MIS 6 and the likely formation of a palaeo-playa later in MIS 6 from 158 ± 11 ka to 143 ± 15 ka. In contrast, the MIS 5 sediments are characterised by oscillating deep- and shallow-water lacustrine units deposited 130 ± 16 ka to 113 ± 20 ka. This study is the first of its kind to provide evidence for a wet desert interior in Australia beyond the last glacial cycle using comprehensive numerical dating. Our results show that past deep-lake episodes of central South Australia, which were previously thought to represent peak interglacial conditions, are actually associated with both warm interglacial and cold glacial periods, with all the wettest episodes generally coinciding with the intervening periods between the glacial and interglacial maximums. We assume from these results that orbital forcing is not a first order control for the long-term dynamics of the Lake Eyre basin and the Indo-Australian monsoon. The high lake-level events of Lake Eyre are well correlated with millennial-scale cooling events and stadials of the North Atlantic, and coincide with weakened episodes/events for the East Asia summer monsoon. This may imply an important role for the northern high latitudes in influencing the Indo-Australian monsoon, which may be associated with a southward migration of the Intertropical Convergence Zone (ITCZ) during cooling periods in the North Atlantic.

**Disciplines**

Medicine and Health Sciences | Social and Behavioral Sciences

**Publication Details**

Fu, X., Cohen, T. J. & Arnold, L. J. (2017). Extending the record of lacustrine phases beyond the last interglacial for Lake Eyre in central Australia using luminescence dating. Quaternary Science Reviews: the international multidisciplinary research and review journal, 162 88-110.

# Extending the record of lacustrine phases beyond the last interglacial for Lake Eyre in central Australia using luminescence dating

Xiao Fu [a] *, Tim J. Cohen [a, b], Lee J. Arnold [c]

[a] *GeoQuEST Research Centre, School of Earth and Environmental Sciences, University of Wollongong, Wollongong, NSW 2522, Australia*

[b] *ARC Centre of Excellence for Australian Biodiversity and Heritage, University of Wollongong, Wollongong, NSW 2522, Australia*

[c] *School of Physical Sciences, Environment Institute, and Institute for Photonics and Advanced Sensing (IPAS), University of Adelaide, North Terrace Campus, Adelaide, SA, 5005, Australia*

**Corresponding author: xiaofuled@gmail.com; xiaofu@uow.edu.au*

**Abstract:**

We show with multiple luminescence dating techniques that the sedimentary record for Lake Eyre, Australia's largest lake, extends beyond 200 thousand years (ka) to Marine Isotope Stage (MIS) 7. Transgressive clayey sand and finely laminated clays overlying the Miocene Etadunna Formation in Lake Eyre North document the deep-lake phases of central South Australia in the past. Until now, unresolved chronology has hampered our ability to interpret these sedimentary records, which are important for understanding the timing of the wettest phase of central Australia's late Quaternary climate. In this study, we apply quartz optically stimulated luminescence (OSL) dating, thermally-transferred OSL (TT-OSL) dating and K-feldspar post infrared infrared stimulated luminescence (pIRIR) dating to lake-floor sediments near Williams Point in Madigan Gulf to provide new age constraint for the lacustrine sediments of Lake Eyre. Methodological studies on quartz and K-feldspar demonstrate that these luminescence dating procedures are suitable for the Lake Eyre lacustrine samples and produce consistent replicate ages. A Bayesian model applied to the new dating results provides a chronological model of lacustrine deposition and shows that the transgressive clayey sand were deposited 221 ± 19 ka to 201 ± 10 ka and that the deep-water sediments were laid down in early MIS 6 (191 ± 9 ka to 181 ± 9 ka). We also find evidence for a potential depositional hiatus in mid MIS 6 and the likely formation of a palaeo-playa later in MIS 6 from 158 ± 11 ka to 143 ± 15 ka. In contrast, the MIS 5 sediments are characterised by oscillating deep- and shallow-water lacustrine units deposited 130 ± 16 ka to 113 ± 20 ka. This study is the first of its kind to provide evidence for a wet desert interior in

Australia beyond the last glacial cycle using comprehensive numerical dating. Our results show that past deep-lake episodes of central South Australia, which were previously thought to represent peak interglacial conditions, are actually associated with *both* warm interglacial *and* cold glacial periods, with all the wettest episodes generally coinciding with the intervening periods between the glacial and interglacial maximums. We assume from these results that orbital forcing is not a first order control for the long-term dynamics of the Lake Eyre basin and the Indo-Australian monsoon. The high lake-level events of Lake Eyre are well correlated with millennial-scale cooling events and stadials of the North Atlantic, and coincide with weakened episodes/events for the East Asia summer monsoon. This may imply an important role for the northern high latitudes in influencing the Indo-Australian monsoon, which may be associated with a southward migration of the Intertropical Convergence Zone (ITCZ) during cooling periods in the North Atlantic.

**Keywords:** Lake Eyre, Williams Point, lacustrine sediments, luminescence dating, Indo-Australian monsoon; Quaternary

## 1. Introduction

Australia's dry interior spans two-thirds of the entire continent, but these desert landscapes used to be much wetter. Long-term floristic and landscape evidence across much of the arid zone indicates a progressive drying of the continent since the Miocene (Fujioka and Chappell, 2010) and especially over the last 350 ka (e.g. Bowler, 1982; Kershaw et al. 2007b; Hocknull et al., 2007; Nanson et al., 2008). However, the timing and causes of Australia's climatic extremes, as well as the characteristics of these past variations, remain unclear. Unlike many parts of the world where tectonic and glacial processes overprint terrestrial palaeoclimate records, Australia's landscapes record this long and potentially punctuated shift in aeolian, fluvial and lacustrine sediment archives (e.g. Bowler et al., 1976; Nanson et al., 1992, 2008; Hesse et al., 2004; Fitzsimmons et al. 2013; Reeves et al., 2013). Of these archives, lakes and their related sediments (e.g. lake-floor sediments, palaeolake shorelines, or shore margin deposits, such as lunettes) are particularly important for hydrological and climatic reconstructions of Quaternary Australia, because they can often provide longer records compared to many other types of terrestrial sediments. Geographically distinct lakes can record the long-term behaviour of different synoptic conditions that bring precipitation to the

Australian continent, such as the Indo-Australian monsoon and the fronts and depressions associated with the mid-latitude westerlies. Given this importance, large playa lakes have been the subject of numerous palaeoenvironmental investigations across the continent in the past few decades (e.g. Bowler et al., 1998, 2003; Zheng et al., 2003; Magee et al., 2004; Cupper, 2006; Cohen et al., 2011, 2012; May et al., 2015).

Deriving a reliable chronology is a key element for interpreting Australian palaeo-lake records. Although most early studies of Australian lakes were focused on the Holocene and the last glacial-interglacial cycle, well dated records beyond the last interglacial (~130 ka) remain rare, mainly because of the absence of suitable dating techniques. Radiocarbon ($^{14}C$) dating was widely used in early studies for dating lacustrine and lakeshore sediments (e.g. Magee et al., 1995), but the upper dating range of this method is limited (~50 ka) and the reservoir effect can be severe for lake deposits (e.g. Hua, 2009). Other dating techniques such as amino acid racemisation (AAR) and uranium-series dating need specific dating materials that are not easily encountered in palaeo-lacustrine records. In the last three decades, thermoluminescence (TL, Aitken, 1985) and optically stimulated luminescence (OSL, Aitken, 1998) dating techniques, which measure the burial ages of clastic minerals in sediments such as quartz and feldspar, have become commonly used geochronological methods for dating late Quaternary shoreline and lacustrine sediments in Australia. Many studies have demonstrated that TL and OSL dating can provide ages with good accuracy and precision for lake samples within the last 130 ka (e.g. Magee et al., 1995; 2004; Cupper, 2006; Cohen et al., 2012; 2015). The use of TL or OSL however has its limitations because the conventional quartz signals (325$^{o}$C TL peak and the 'fast' OSL component) saturate early (~100 – 200 Gy) in most samples, and therefore become less applicable when dating Middle Pleistocene deposits (e.g. English et al., 2001), unless the dose rates are especially low (e.g. Bowler et al., 2001; Nanson et al., 2008).

Recently, various extended-range luminescence dating procedures have emerged which utilise dating signals with higher dose saturation levels (Yoshida et al., 2000; Fattahi and Stokes, 2000; Jain et al., 2007; Jain, 2009; Wang et al., 2006; Thomsen et al., 2008). One of these techniques, termed post infrared infrared stimulated luminescence (pIRIR) dating of K-feldspars (Thomsen et al., 2008; Li and Li, 2011; Buylaert et al., 2012), has received particular attention as it has been shown to minimise or even completely remove the malign effect of anomalous fading (Wintle, 1973; Spooner, 1994) and has yielded accurate ages up to ~300-400 ka (Li et al., 2014a; Arnold et al., 2015). Another increasingly used extended-range dating method for quartz is the thermally transferred OSL (TT-OSL) procedure (Wang et al., 2006, 2007), which has been shown to be applicable over age ranges that are an order of magnitude higher than conventional quartz OSL (Duller and Wintle, 2012; Arnold et al., 2015). These dating procedures hold great potential for extending the dating range of lacustrine sediments in Australia over late and middle Pleistocene timescales; however, neither has been applied in Australian palaeo-lacustrine contexts previously.

In this study, we have applied a range of luminescence dating techniques to establish a detailed chronology for the undated lake floor (lacustrine) sediments of Lake Eyre (officially named Kati Thanda-Lake Eyre), the largest playa lake in Australia. Lake Eyre is the depocentre for Australia's largest internally-draining basin, which covers one seventh of the Australian continent (Habeck-Fardy and Nanson, 2014). The lake is mainly fed by runoff derived from monsoon-watered northern Australia. Its sedimentary history and palaeohydrology therefore constitutes a record of monsoon runoff and allows investigation of the Australian monsoon throughout the Quaternary (Croke et al., 1999). Previous chronological studies of the lake have focused on the palaeoshoreline deposits, which have demonstrated marked high lake stands in Marine Isotope Stage (MIS) 5 and a drying tendency since the last interglacial and especially after ~ 48 ka (Magee et al., 2004; Cohen et al., 2015). Magee et al. (1995) inferred that the deep-water lacustrine sediments on the lake floor, which represent the wettest phase of Lake Eyre during the late Quaternary, might be MIS 5e in age (the warm peak of the last interglacial). In this study, we apply K-feldspar pIRIR and quartz TT-OSL dating procedures together with conventional quartz OSL dating to the lacustrine sediments near Williams Point at Madigan Gulf (Magee et al., 1995). Our results refine previous interpretations as to when the now dry interior was experiencing peak wet intervals in the late Quaternary. The new chronology of the lake floor obtained in this study is combined with the recently published palaeo-shoreline chronology (Cohen et al., 2015) to reconstruct a lake-full history of Lake Eyre since MIS 7. This reconstruction provides new insights into how the Indo-Australian monsoon has responded to glacial-interglacial cycles and the potential driving force for the intensification of Indo-Australian monsoon in the late Quaternary.

## 2. Study site

### 2.1. Regional setting

Modern Lake Eyre is an ephemerally flooded playa in central South Australia (28° 22′S, 137° 22′E), located at the southwestern margin of the Australia's largest endoreic drainage system, the Lake Eyre Basin (LEB, $1.2\times10^6$ $km^2$, Fig. 1a). Lake Eyre has a total area of 9690 $km^2$, and is composed of two basins, Lake Eyre North and Lake Eyre South connected by the Goyder Channel (Fig. 1b). The climate near the lake is hot and dry. The mean monthly maximum and minimum temperatures are 28.8°C and 13.3°C, respectively (Bureau of Meteorology (http://www.bom.gov.au/water/hrs)), and the average annual rainfall and evaporation are <150 mm and >3600 mm, respectively (Magee et al., 1995). The maximum depth of the playa is −15.2 m Australian Height Datum (AHD), which represents the lowest point on the Australian continent (Kotwicki and Allan, 1998).

As the terminus of the LEB, Lake Eyre is dominantly fed by inflows from the northeastern rivers−the Cooper Creek and the Georgina-Diamantina River, and less frequently from the western tributaries of the Neales and Macumba rivers (Figs. 1a and 1b). Since the main tributaries receive precipitation from the tropics, driven by Indo-Australian summer monsoon, the filling and drying of Lake Eyre is mainly a reflection of tropical monsoon intensity. The modern hydrological regime of Lake Eyre is normally dry due to the great difference between local evaporation and precipitation, and also due to significant transmission loss of surface water runoff given the low-gradient flow path through Australia's central deserts and dunefields (Habeck-Fardy and Nanson, 2014). Lake Eyre fills today only at times of monsoon enhancement, with the maximum historical filling recorded in 1974 when the lake level reached ~5 m above the lowest point. During the late Quaternary, the lake was much wetter than present and the lake level has periodically reached maximum depths of 25 m (i.e. +10 m AHD) in MIS 5 (Magee et al., 2004; Cohen et al., 2015) and 20 m (i.e. +5 m AHD) in mid-late MIS 4 (Magee et al., 2004) or early MIS 5 (Cohen et al., 2015). During some of these high lake stands, Lake Eyre was joined to the Lake Frome-Callabonna-Blanche-Gregory system via the Warrawoocara channel, forming a megalake approximately ten times larger in area than modern Lake Eyre (Nanson et al., 1998; Cohen et al., 2011, 2012, 2015). This megalake, however, was last recorded at 48 ± 2 ka, and was followed by a major hydrological change resulting in the shift to playa-dominated conditions (Cohen et al., 2015). Between the wet phases or lake high-stands, the lake was dry and it has been inferred that the formation of the ground water-controlled playa resulted in widespread lake-floor deflation, lowering the lake-floor by more than 4 m below the present floor (Magee et al., 1995; Magee and Miller, 1998).

Madigan Gulf is the largest bay at the southern end of Lake Eyre North (Fig. 2a). The centre of the gulf lies below -15 m AHD and Williams Point, which is the focus of this study, is located at the southern portion of Madigan Gulf (Fig. 2a). Williams Point is represented by a wave-cut cliff of Quaternary sediments overlying the lake floor (Fig. 2b). The cliff and the morpho-stratigraphic relationships at Madigan Gulf have been interpreted in the past by King (1955), Magee et al. (1995) and Magee and Miller (1998) as having been incised by lake-floor deflation during dry lake periods.

### 2.2. Stratigraphy of Williams Point and the existing chronology

The Williams Point sequence and the lake-floor stratigraphy of Madigan Gulf have been logged thoroughly by Magee et al. (1995). These authors divided the sequence into three broad sedimentary units from the bottom to the top, which correspond to a deep-water lacustrine environment, an oscillating deep- and shallow-water lacustrine environment and lake or playa margin deposits (aeolian sediments), respectively (see Fig. 12 of Magee et al., 1995).The deep-water phase is discriminated from the shallow-water phase based on the laminated lacustrine clays and the interpreted presence of salinity stratification with predicted depths beyond wave base. Here, we refine the original description of the lake margin by Magee et al., (1995) with additional field observations and supplementary cores, as shown in Fig. 2b. Based on the new cores and the existing interpretation from core 83/6 (see Fig.4 of Magee et al., 1995), the stratigraphy of Williams Point can be described by three phases from the bottom to the top:

*Phase 1—lacustrine-dominated phase (-17.4 m to -9.9 m AHD)*: This sequence is characterised by a range of facies that extends from the lake-floor into the base of the cliff outcrop. The lower most part of this sequence *(-17.4 m to -13.6 m AHD)* is represented by lake-floor deposits which are composed mainly of thick (decimetre) lacustrine sediments that directly overly the Etadunna Formation (Miocene in age) and can be divided into three sub-units. From -17.4 m to -16.7 m AHD, the sediments are mainly composed of grey to light-grey clayey sand bedding which represent the basal transgressive sediments deposited when the lake began to receive sediment input (units M1 to M3 of Magee et al. 1995); Between -16.7 m and -14.0 m AHD, the sediments are mainly composed of finely laminated (sub mm) dark-grey or grey clay, which are interpreted to represent deep-water conditions when the lake was perennially full and to depths that allowed salinity stratification (Unit L3 of Magee et al., 1995); Between -14.0 m and -13.6 m AHD, the sediments mainly consist of poorly laminated red brown clay with gypsum layers present and the grain size of this sub-unit is slightly coarser than the underlying deep water facies. This thin oxidised sub-unit is interpreted to represent a playa phase when the lake was commonly dry and was not described in the original 83/6 core by Magee et al., (1995). Above this muddy playa sub-unit is 3.7 m *(-13.6 m to -9.9 m AHD)* of light-green grey to light-blue grey clay with facies with either fine or poor lamination and gypsum horizons periodically present. This sequence represents the upper portion of the lacustrine sequence and extends from the base of the cliff outcrop to the lake floor (Fig.2b; units L2 to L1 of core 83/6 in Magee et al., 1995). The varying light and dark colour of sediments in this part of the lacustrine sequence indicates oxidising conditions and the thinner laminated lake deposits compared to the lower section. These sediments are interpreted to represent a mix of deep- and shallow-water lacustrine environments (mainly shallow-water).

*Phase 2—oscillating deep-water and shallow-water phase (-9.9 m to -3.1 m AHD)*: Sediments in this part of the sequence consist mostly of yellow to olive yellow sandy clay or sand with poor lamination, with occasional interludes of deep-water clay. This unit indicates a lake or a fluvio-deltaic setting with oscillating water depth. This includes the platy dolomite and the cliff section lacustrine units of Magee et al., (1995).

*Phase 3—aeolian deposition phase (-3.0 m to +3.8 m AHD)*: The top stratigraphic unit of the Williams Point cliff is composed of light-yellow to light-grey gypseous aeolian sand, which is heavily pedogenically overprinted. Pelletal clays have been found in the aeolian deposits. This unit, termed the Williams Point aeolian unit in Magee and Miller (1998), has been interpreted to represent a period when the lake was dry or drying and the aeolian deposits were formed due to lake-floor deflation events.

Our stratigraphic division indicates a variable lake level and a general drying tendency for Lake Eyre in the late Quaternary. Magee et al. (1995) chronologically constrained the Williams Point sequence using multiple dating methods. Based on $^{14}C$, AAR, U-series and TL dating, they argued that the Williams Point aeolian unit formed 60-50 ka, and the base of oscillating deep- and shallow-water phase (phase 2 in this study) corresponded to an age of 92 ka. These authors also provided five $^{14}C$ ages for the deep-water lacustrine phase (phase 1 in this study) between 20 and 45 ka. However, these ages are considered to be unreliable (or minimum ages at best) since the age of this sedimentary unit greatly exceeds the upper limit of radiocarbon dating. Magee et al. (1995) tentatively correlated the deep-water lacustrine phase with the +10 m AHD palaeoshorelines nearby. Based on the OSL ages of these shorelines, Magee et al. (1995) deduced that the deep-water lacustrine unit was early MIS 5 (i.e. MIS 5e, ~123-130 ka) in age. This initial interpretation now seems unlikely following recent redating of the +10 m AHD palaeoshorelines. Cohen et al. (2015) have shown that these high shorelines formed 108 ± 5 ka and 94 ± 4 ka, and were followed by a period at 79 ± 4 ka when Lake Eyre attained its maximum 25m depth. Therefore, the question remains as to the exact time period represented by the 'deep-water' facies of Lake Eyre and in this paper we address this by focussing on *Phase 1* – the lacustrine-dominated phase.

### 2.3. The studied core

In order to provide a reliable chronology for the undated lacustrine phase of the Lake Eyre sequence, we have retrieved a core from the playa floor adjacent to Williams Point cliff. This 4 m core named LEWP1, ranges from the top of the Etadunna Formation (-17.4 m AHD) to the modern playa surface (-13.4 m AHD), is also supplemented by LEWP2 (-9.2 m to -13.3 m AHD, a core that links the playa floor core in this study to the exposed sediments in the cliff, Fig. S1). When combined, these two cores replicate the original core 83/6 from Magee et al., (1995). We note that no co-ordinates have been provided for the Magee et al. (1995) 83/6 core as it was collected prior to GPS usage. We have therefore estimated the distance between our core positions and those of 83/6 based on published figures. There is 100 m between LEWP1 and LEWP2 and we assume that 83/6 is very close to our LEWP 2 core. The main investigated core (LEWP1) incorporates three sub-units of the deep-water lacustrine dominated phase (*Phase 1,* as mentioned above) and also includes a thin modern playa sediment layer at the top of the core. From the bottom to the top, the core is composed of basal transgressive clayey sand (Unit E), deep-water lacustrine clay (Unit D), red brown playa sediments (Unit C) and surface modern playa sediments (Unit B). Fig. 3 shows a photo and schematic log of the core. A detailed log of the core is summarised in Table 1.

## 3. Sampling and methods

### 3.1. Sample collection and preparation

We collected eleven luminescence dating samples in a vertical sequence from the LEWP1 core (samples LEWP 0.50 to LEWP 3.82 in Fig. 3). The inner non-light exposed sediments of the core were collected for palaeodose measurements under safe (dim-red) light conditions. We sampled homogeneous sedimentary units >5 cm and tried to avoid thick gypsum layers and lithological boundaries within 30 cm of the samples to maximise uniformity for gamma dose rate calculations. For some samples it was not possible to avoid laminae or lithological boundaries within the surrounding 30 cm; hence we have incorporated gamma dose rate contributions from different laminae in the final dose-rate calculations where necessary (see Supplementary Information (SI)). In addition to the LEWP1 core samples, we collected one sample (LE14-1) from the base of the Williams Point cliff outcrop with an AHD depth of -10.74 m, which is equivalent to the middle section of the LEWP2 core. This sample is used to constrain the age of the finely laminated shallow-water lacustrine sub-unit (-13.6 m to -9.9 m AHD), which is denoted here as Unit A (Fig.S1). A summary of all the dating samples are given in Table 2. Besides the above mentioned dating samples, two replicate modern samples (LE-M and LE14-MA1) were also collected from a modern playa layer (Unit B in Fig. 3) for residual dose evaluation (assuming the samples are water-lain) and one sample LEWP 1.96 was collected in the middle of the LEWP1 core for dose rate evaluation for adjacent samples (Fig. 3).

Quartz and K-feldspar grains for equivalent dose ($D_e$) evaluation were prepared using standard separation method (Aitken, 1998, see details in SI). For the LEWP1 core samples, coarse grains (63-90, 90-180 μm) and medium grains (45-63 μm) were separated, but the former was only successfully recovered from a few samples. We mainly used medium grain size quartz and/or K-feldspar for single-aliquot $D_e$ measurements using medium aliquots (~4 mm). This was in exception to five K-feldspar samples for which the coarse grain size were measured for detecting partial bleaching using small aliquots (~1 mm, ~40-100 grains, which are expected to be dominated by < 20 grains, e.g. Reimann et al., 2012). For LE14-1, we were able to separate sufficient sand-sized (212-250 μm) quartz grains, and hence it was possible to perform single-grain measurements for this sample.

### 3.2. Dose rate and equivalent dose determination

Dose rates and $D_e$ values were measured in the luminescence dating laboratories of the University of Wollongong (LEWP1 core samples) and the University of Adelaide (sample LE14-1) in parallel. Details of the luminescence dating procedures and instrumentation employed in this study are provided in the SI. Environmental dose rates were determined using a combination of ICP-OES and ICP-MS for the LEWP1 core samples, and in situ field gamma-ray spectrometry and low-level beta counting for sample LE14-1. Grain-size attenuation and long-term moisture content have been taken into consideration in the dose rate calculations (see SI). In order to detect any secular disequilibrium for the Lake Eyre samples, we additionally measured the specific activities of radionuclides in the $^{238}$U and $^{232}$Th decay series for seven samples using high resolution gamma spectrometry (HRGS, Murray et al. 1987).

We have applied a range of complementary dating procedures for quartz and K-feldspar $D_e$ estimation, using procedures specified in Table S3. For the LEWP1 core samples, we began with OSL dating of quartz using conventional single-aliquot regeneration (SAR) procedure (Murray and Wintle, 2000; 2003) (Table S3a). However, due to the antiquity of the LEWP1 core sediments, single-aliquot quartz OSL dating was only applicable to four of the samples, for which the natural OSL signals are non-saturated (samples LEWP 0.50, 0.89, 1.40 and 3.63). Compared to quartz, K-feldspars generally have much higher saturation dose limits (Aitken, 1998), and therefore offer greater potential for dating older samples. We have employed a multi-elevated temperature pIRIR procedure (MET-pIRIR, Li and Li, 2011) (Table S3b) for single-aliquot K-feldspar dating of all LEWP1 core samples. The $pIRIR_{250}$ signal, which has been shown to be thermally stable (Li and Li, 2011; Fu et al., 2012), was used to derive the K-feldspar $D_e$ values for final age calculation. It is noted that in order to save machine time, we have applied the standard growth curve (SGC) method of Li et al.

(2015a, b) for quick $D_e$ estimation in single-aliquot quartz OSL dating and single-aliquot K-feldspar pIRIR dating. Besides the aforementioned two procedures, we have also applied single-aliquot TT-OSL dating to six samples from the LEWP1 core for cross checking purposes (employing the dating procedure of Ademiac et al., 2010; Table S3c). For sample LE14-1, single-grain OSL dating and single-grain TT-OSL dating were conducted using procedures shown in Tables S3d and S3e, respectively. The single-grain TT-OSL dating approach follows on from the reliable application of this procedure at a range of sites (Arnold et al., 2013, 2015; Arsuaga et al., 2014; Demuro et al., 2014, 2015).

## 4. Results

### 4.1. Dosimetry

The dose rates of all the samples are summarised in Table S1 and the observed U, Th and K contents for the LEWP1 core samples are plotted against their depth in Figure 4a-c. Generally, the concentrations of Th and K show small variations through the core, with the exception of the two bottom samples collected from the basal transgressive sediments (LEWP 3.63 and 3.82). These two samples show lower Th and K contents compared to other samples, which might be attributed to a difference in lithology. In contrast to Th and K, the U content shows a large variation in the middle part of the core. Unusually high U contents were observed for two samples at depth of 1.58 m (LEWP 1.58, ~20 ppm) and 1.77 m (LEWP 1.77, ~9 ppm), which are 2-5 times greater than the adjacent samples (4-5 ppm) (Table 2). As a consequence, the external dose rate of these two samples is 1.5-2.5 times higher than their neighbouring samples.

Based on the sedimentological properties of the deposits at these depths, we interpret the U content of samples LEWP 1.58 and LEWP 1.77 as uncharacteristically high. The lithology of the two U-rich samples in the middle part of the core are identical in grain size and structure to samples above and below. Our dating results (section 4.3) show that the apparent ages of the two U-rich samples are stratigraphically reversed compared to other samples. Given that the $D_e$ estimates for these samples are considered to be robust (section 5.1), it implies the modern dose rates may not represent the long-term average dose rate for these two samples.

It is possible that the high U concentration for these two samples is caused by complex post-depositional uptake of nuclides in the uranium decay series, which is difficult to resolve from our dosimetric assessments. Different geochemical processes such as carbonate precipitation, organic accumulation and post-depositional groundwater movement are known to cause mobile uranium isotopes and their daughter products to move into or out of certain lacustrine systems (e.g. Krbetschek et al., 1994; Olley et al., 1996, 1997; Preusser and Degering, 2007); indeed, uptake of U isotopes has been observed elsewhere for playa sediments in Australia (e.g. Cupper, 2006). In order to investigate the possible impact of carbonate precipitation, we used X-ray diffraction (XRD) to quantify the carbonate contents of five samples from different depths of the core. The results show that the two U-rich samples have similar carbonate content (4-14%) compared to other equivalent sedimentary units. Furthermore, there are no obvious signs that the organic contents of these two samples are uncharacteristically high.

We speculate that groundwater movement may play an important role in the uptake of unsupported or partially supported U series nuclides for samples LEWP 1.58 and LEWP 1.77, consistent with the interpretations of Preusser and Degering (2007). It is noteworthy that there are several large uranium mines <300 km to the south and southeast of Lake Eyre (e.g. the Beverly Uranium Mine, the Olympic Dam Mine). It is possible that, at certain times in the past, highly U-rich ground water could have migrated to our study site (the lowest point on the continent) and resulted in transferral of radionuclides to sediments lying in the vadose zone. Since several of the long-lived uranium series nuclides are soluble, and can be readily dissolved by groundwater circulation, any such post-depositional uptake is likely to complicate dose rate assessments. This type of open system behaviour typically manifests itself as present-day disequilibrium in the U decay series chain when undertaking HRGS measurements (e.g., Olley et al., 1996; Stokes et al., 2003; Guibert et al., 2009). Figs. 4d and 4e summarise the HRGS specific activity ratios of $^{226}$Ra/$^{238}$U and $^{210}$Pb/ $^{226}$Ra for the seven LEWP1 core samples (also see Table S2 for detailed data). Interestingly, it can be seen that the daughter-parent isotopic ratios are consistent with unity for all samples, including the two U-rich samples, which confirms that their uranium decay chains are in present-day equilibrium. The fact that these two samples have very high $^{238}$U, $^{226}$Ra and $^{210}$Pb activities but do not display uranium series disequilibrium could imply a more complex post-depositional uptake history involving influxes of partially supported U series nuclides or multiple influxes of unsupported nuclides from both the top and bottom of the decay series. Such complexities could act to partly or completely mask present-day parental U-series excesses, depending on the nature, timing and activities of the various radionuclide influxes in the past. These interpretations remain speculative until further dosimetric measurements are performed on LEWP 1.58 and LEWP 1.77. However, the uncharacteristically high U series activities of these two samples provide reasonable grounds for treating their resultant luminescence chronologies with caution.

Fig. 4f confirms that the ratio between $^{228}$Th and $^{228}$Ra, which are two daughters of $^{232}$Th, overlap with unity at 2σ for all samples (i.e., the Th chain is in present-day equilibrium). The final dose rates calculated for each sample using HRGS measurements are also consistent with the corresponding results obtained from ICP-MS and ICP-OES measurements (Fig. S2).

The measured moisture contents are given in Fig. 4g. For all the samples, the moisture contents are relatively high (~36-50%) and show small variations with depth. We interpret the relatively uniform moisture content throughout the core to indicate rapid compaction after accumulation of the deposit. Thus, the variation of moisture content with time is not expected to be large and should be sufficiently covered by the associated water content uncertainty term (relative uncertainty = 25%).

Since eight of our samples were collected from laminated deposits that are surrounded by inhomogeneous sedimentary matrices (within 30 cm) (e.g. Fig.S3), we have considered the effects of spatial heterogeneity in gamma dose rates in our age calculations. Special attention has been paid to gypsum layers thicker than 1 cm, which are likely to impart significant gamma dose rate effects on adjacent samples. We corrected the gamma dose rate of the eight samples based on the model of Aitken (1985, p. 289-293, see detail in SI). The water attenuated gamma dose rates account for ~30-35% of the total environmental dose rates for these samples. The variation of the gamma dose rate due to the above correction is ~2-25% (Table S1). Therefore, the gamma dose rate correction changes the total environmental dose rates by ~1-7% for quartz and ~1-6% for K-feldspar.

### 4.2. Luminescence characteristics and $D_e$ distributions

### 4.2.1. Single-aliquot quartz OSL dating

A representative quartz OSL decay curve is shown in Fig.S4, which can be seen to exhibit a dominant fast component. An average recycling ratio consistent with unity at 1$\sigma$ and an average recuperation of <1% was observed for all of the samples. These results suggest the sensitivity correction is effective and the impact of charge transfer is negligible. A dose recovery test (Murray and Wintle, 2003) (see details in SI) yielded a recovered-to-given dose ratio of 0.95 ± 0.05 (n=20) (Fig.5a), supporting the appropriateness of the selected measurement conditions. Fig.S5c shows a comparison of the $D_e$ values obtained using the SGC method and the conventional SAR method. For all of the four samples, the SGC method yielded $D_e$ values consistent with those of the SAR method. This suggests that the SGC method can be effectively used for single-aliquot OSL $D_e$ determination in this study (see further details about the SGC method in SI).

The overdispersion (OD) value of the four measured samples, calculated using the central age model (CAM, Galbraith et al., 1999), varies between 16 and 29% (see an example in Fig. 5b). These values are slightly higher than the global average value of 9 ± 3% published for well-bleached large sized aliquots (Arnold and Roberts, 2009). However, given that the single-aliquot OSL dose recovery test also gives a higher than average OD value of 17% (Fig. 5a), it is suggested that a large part of this OD originates from intrinsic $D_e$ scatter associated with inherent luminescence characteristics and experimental conditions (e.g., Arnold et al., 2012a, Demuro et al., 2013), rather than issues such as partial bleaching or post-depositional mixing (e.g., Bailey and Arnold, 2006; Arnold et al., 2008, 2013).

### 4.2.2. Single-aliquot K-feldspar pIRIR dating

Figs.S6a and b show typical IRSL/pIRIR signal decays and corresponding dose response curves (DRCs) for the five IRSL/pIRIR signals of the MET-pIRIR procedure. For all the LEWP1 core samples, the sensitivity-corrected natural signals lie far below the signal saturation levels, and are therefore within the reliable dating range of the pIRIR protocol. The average recycling ratios for all samples are consistent with unity at 1 $\sigma$ and the average recuperation values are <2%. A dose recovery test (see details in SI) yielded recovered-to-given dose ratios within 10% of unity for all of the five signals (n=5) (Fig. 6a). These results confirm the suitability of the MET-pIRIR procedure when applied to a solar bleached and non-thermally treated sample. Figs. S8a-e compare the $D_e$ values obtained using the SGCs and using the full MET-pIRIR. For all signals, the $D_e$ values derived from the two methods agree with each other at 1σ (see further details in SI).

The capability of the MET-pIRIR procedure to isolate a non-fading K-feldspar signal has been demonstrated across a range of different depositional contexts (Li and Li, 2011; Fu et al., 2015, 2017; Gong et al., 2014; Li et al., 2014b; Fu, 2014). To confirm the stability of the pIRIR signal in this study, we measured the anomalous fading rates (Huntley and Lamothe, 2001) for three of our samples following the method of Auclair et al. (2003). These results reveal an obvious decrease in the anomalous fading rate (g-value normalised to a delay time of 2 days) with higher IR stimulation temperature, with the average g-value decreasing from ~6-2%/decade for 50°C to ~0-1 %/decade for 250 °C (Fig. 6b). The small fading rate of ~0-1% for the $pIRIR_{250}$ signal agrees with previous published values for high temperature pIRIR signals (e.g. Thiel et al., 2011; Buylaert et al., 2012; Arnold et al., 2015). This low fading rate is commonly regarded as a laboratory artefact rather than an indicator of signal instability (Buylaert et al., 2012) on the basis of comparisons made with independent age control and replicate quartz OSL ages. Therefore, we suggest that the $pIRIR_{250}$ signal in our MET-pIRIR procedure is unlikely to suffer from fading and that fading correction is not warranted for age calculation.

The extent of signal resetting for the K-feldspar samples was evaluated by measuring the residual dose of a modern analogue sample LE-M (Fig.3). The measured residual doses increase with higher IR stimulation temperatures, and vary from 1.6 Gy to 10.5 Gy for the 50°C to 250°C MET-pIRIR signals (Fig. 6c). These residual doses are relatively small compared to the natural $D_e$ of the LEWP1 core samples (~250-630 Gy), and are consistent with previously reported values for well-bleached samples (e.g. Buylaert et al., 2011; Li and Li, 2011; Arnold et al., 2015). Such residuals are suggested to mainly originate from thermal transfer or non-bleachable signals rather than incomplete bleaching (e.g. Buylaert et al., 2011). The minor residual dose for the MET-$pIRIR_{250}$ signal was subtracted from the measured $D_e$ before age calculation, although it has insignificant impact on the final ages. It is also possible to assess the extent of signal resetting using the $D_e$ distribution characteristics of the five coarse grain samples measured using small aliquots. The OD values for the

$pIRIR_{250}$ $D_e$ range from 9% to 16% (n=9-16) (e.g., Fig.7a), which are within the common range for well-bleached multi-grain aliquot samples (Arnold and Roberts, 2009). $D_e$-T plots, in which the $D_e$ values are plotted against the IR stimulation temperatures (Li and Li, 2011), were additionally used to detect any potential partial bleaching problems with these samples. For all the LEWP1 core samples, a plateau is observed in the $D_e$-T plot between 200 and 250°C (see examples for coarse and medium grains in Figs. 7b and c), suggesting that these samples were well-bleached before deposition. The presence of age plateaus in the $D_e$-T plot also indicates the non-fading signal has been isolated using the MET-pIRIR procedure (Li and Li, 2011).

#### 4.2.3. Single-aliquot TT-OSL dating

Representative single-aliquot TT-OSL signal decay curve and corresponding DRC are given in Fig. S10. The sensitivity-corrected natural TT-OSL signal lies within the linear range of the DRC (Fig. S10c). For the six measured samples, the recycling ratios are consistent with unity at 1$\sigma$ and the recuperation values are all <2%. A dose recovery test (see details in SI) yielded a recovered-to-given dose ratio of 0.96 ± 0.07 (n=3) for the single-aliquot TT-OSL procedure.

The OD values for the six samples measured vary from 4% to 13% (n=5-7). This small OD is expected given that medium grain size and 4 mm aliquots were used for $D_e$ determination. The inferior bleachability of the TT-OSL signal is borne out by the larger residual dose of 45.6 Gy measured for the modern analogue sample. This residual dose is slightly larger than published values for aeolian sediments (5-30 Gy, Duller and Wintle, 2012), but it is much smaller than the value reported for highly turbid fluvial sediments (e.g., Hu et al., 2010; 200-300 Gy). The residual dose of the modern analogue samples is subtracted from the TT-OSL $D_e$ before age calculation for all of the samples. The appropriateness of this residual dose correction is supported by the consistency between the final single-aliquot TT-OSL, OSL and pIRIR ages (see Section 5.1).

#### 4.2.4. Single-grain OSL and TT-OSL dating

The SAR quality-assurance criteria of Arnold et al. (2013, 2014) were applied for single-grain OSL and TT-OSL dating of sample LE14-1. Fig.S11 shows that the majority of accepted grains display rapidly decaying OSL and TT-OSL curves (reaching background levels within 0.5 s). Dose recovery tests (see details in SI) attest to the general suitability of the single-grain OSL and TT-OSL SAR procedures, yielding recovered-to-given dose ratios of 1.06 ± 0.03 (OD=15 ± 4%) and 1.07 ± 0.09 (OD=27 ± 6%) for the single-grain OSL and TT-OSL procedures, respectively (Figs. 8a and 8b).

The single-grain OSL and TT-OSL $D_e$ distributions of sample LE14-1 are shown as radial plots in Figs. 8c and 8d. The OSL $D_e$ dataset is characterised by moderate dose dispersion (relative range 2.5), a single dose population that is centred on the weighted mean $D_e$ value, and normally distributed $D_e$ scatter (when tested using the criterion of Arnold and Roberts, 2009; Arnold et al., 2011). The OD value (24 ± 4%) is consistent with that obtained in the single-grain OSL dose recovery test at 2σ, as well as the global average value for fully bleached and undisturbed single-grain $D_e$ datasets (20 ± 1%; Arnold and Roberts, 2009). The single-grain TT-OSL $D_e$ dataset shares similar characteristics to its single-grain OSL counterpart (relative range = 2.3, absence of statistically significant skewness, single dose population) and a consistent OD value of 34 ± 6% at 2σ. The latter is also comparable to OD values reported elsewhere for ideal (well-bleached and unmixed) single-grain TT-OSL samples (e.g., Arnold et al., 2014, 2015; Demuro et al., 2014, 2015; Ollé et al., 2016). These $D_e$ characteristics suggest complete resetting of both the OSL and TT-OSL signals before burial, and they do not reveal any obvious signs of contamination by mixed grain populations.

A single-grain TT-OSL residual $D_e$ value of 10.8 ± 2.1 Gy was obtained for a modern analogue sample (LE14-MA1) collected ~5 cm beneath the present-day lake floor. This residual $D_e$ value is significantly lower than the residual dose obtained for the multi-grain TT-OSL modern analogue sample (45.6 Gy), suggesting that the latter largely arises from grain types that are routinely rejected by the single-grain quality assurance criteria. This is confirmed by examining 'synthetic aliquots' created from all of the accepted and rejected grain types present on each of the LE14-MA1 single-grain discs (equivalent to creating multi-grain aliquots containing 100-grains each). The synthetic aliquot $D_e$ value of the modern analogue sample increases by a factor of four (47.9 ± 7.3 Gy) and is indistinguishable from that obtained using traditional multi-grain TT-OSL dating (45.6 Gy).

The single-grain TT-OSL residual $D_e$ value is significantly smaller than the 2σ TT-OSL $D_e$ uncertainties for LE14-1, and there are no obvious signs of partial bleaching in the natural $D_e$ distribution of this sample. It is also unclear whether an average residual dose subtraction is directly applicable to individual grains that are likely to have been variably affected by different sources and amounts of $D_e$ overdispersion. Given these issues and complexities at the single-grain scale, we have opted not to include an additional residual dose subtraction in the single-grain TT-OSL age estimate of LE14-1. We note, however, that application of an average residual $D_e$ subtraction would only decrease the final TT-OSL age of this sample by ~8 ka, which is well within the existing 1σ uncertainty range (Table 2).

### 4.3. Chronology

The final single-aliquot OSL, TT-OSL and K-feldspar pIRIR ages for the LEWP1 core samples are plotted against depth in Fig. 9, and all dating results are summarised in Table 2. All the single-aliquot and single-grain ages were calculated using the CAM on the basis of their $D_e$ distribution characteristics. In general, the ages of all samples are in stratigraphical order, except for three samples, LEWP 1.40, 1.58 and 1.77, which are stratigraphically reversed compared to other samples from Unit D (Fig. 9). Sample LE14-1 (Fig.2) collected from the upper part of the lacustrine sequence (Unit A) yields OSL and TT-OSL age of 126 ± 10 ka and 141 ± 12 ka and sample LEWP 0.50 (Fig.3) collected from the playa layer in the LEWP1 core (Unit C) produces OSL, pIRIR and TT-OSL ages of 130-148 ka. Five samples within the finely laminated deep-water lacustrine unit (Unit D), excluding samples LEWP 1.40, 1.58 and 1.77, gave OSL, pIRIR and TT-OSL ages of 168 to 217 ka, and two samples collected from the basal transgressive sediments (Unit E) yielded OSL, pIRIR and TT-OSL ages of 175 to 223 ka. The ages of the samples from the finely laminated deep-water lacustrine and transgressive sediments units (Units D-E) are statistically consistent at 2σ. These consistent ages suggest relatively rapid deposition in a short timeframe for the two sedimentary phases.

The OSL, pIRIR and TT-OSL ages of samples LEWP 1.40, 1.58 and 1.77 are between 102 and 168 ka, and are systematically younger than other samples in the same sedimentary unit (Fig. 9). The latter two samples, which show the youngest ages, also exhibited abnormally high U contents in their dose rate evaluations, as detailed earlier (section 4.1). We consider these two ages to be underestimated due to potential overestimation of long-term dose rates when calculated using present-day uranium contents. As such, we have cautiously omitted these two samples from our final chronological discussions. Sample LEWP 1.40 does not display a particularly high uranium content, but its gamma dose rate is significantly affected by the adjacent uranium rich sediments of sample LEWP 1.58. This is illustrated by comparing the age obtained using the 'uncorrected' gamma dose rate for sample LEWP 1.40 (i.e. calculated using bulk sediment from the sample position rather than additional sediment from the surrounding matrix, Table S1). In this case, the OSL and pIRIR ages of LEWP 1.40 increase to 151 ± 14 ka and 175 ± 15 ka, respectively, which are consistent with the ages obtained for reliable adjacent samples at 2σ. However, since use of an 'uncorrected' gamma dose rate is considered sub-optimal in spatially heterogeneous sediments, we have also chosen to reject this sample from further consideration.

## 5. Discussion

### 5.1. Reliability of different luminescence dating procedures

The reliability of the multiple dating procedures used in this study can be assessed by considering the internal diagnostic criteria of the SAR procedures and by inter-comparison of the replicate dating results. For the three single-aliquot dating procedures listed in Table S3, the three routine SAR tests — recycling ratio, recuperation and dose recovery (Wintle and Murray, 2006) — have yielded satisfactory results for all the samples. This indicates the chosen dating procedures are internally robust. The single-grain dating procedures are similarly supported by reliable dose recovery test results and the application of comprehensive SAR quality assurance criteria (Table S4). Inter-comparison of ages obtained using multiple luminescence dating procedures is increasingly being used as a means to assess methodological validity and to yield insights into potential issues such as signal instability and incomplete signal resetting (e.g. Murray et al., 2012; Zander and Hilgers, 2013; Arnold et al., 2015; Demuro et al., 2015; Fu et al., 2015). The latter issue can warrant particular attention when undertaking multi-grain dating of water-lain sediments. In these settings, luminescence signals may be more difficult to bleach due to subaqueous sunlight attenuation, especially for the more slowly bleached pIRIR and TT-OSL signals (e.g. Lowick et al., 2012; Kars et al., 2014; Hu et al., 2010). A comparison of three single-aliquot dating procedures in this study (Fig. 9) shows that the replicate quartz OSL, K-feldspar pIRIR and quartz TT-OSL ages are all consistent at 1 or 2$\sigma$. It provides support that the quartz OSL signal and K-feldspar pIRIR signal are sufficiently bleached, and that the multi-grain residual dose for TT-OSL has been effectively corrected for in our dating procedure. Further support for sufficient bleaching of the pIRIR signal comes from the homogenous $D_e$ distributions (Fig. 7a) and the presence of plateaus in the $D_e$-T plots (Figs. 7b and c). Based on these results, it is concluded that partial bleaching is unlikely to be a significant problem for the multi-grain Lake Eyre samples.

It is worth noting that many of the aliquots measured in our quartz OSL dating study exhibited relative high natural doses that were close to, or above, the $2D_0$ (characteristic saturation dose) limit. According to the suggestion of Wintle and Murray (2006), such aliquots may exceed the upper limit of precise OSL dating if the DRCs are fitted using a single saturating exponential growth function (but see discussions in Arnold et al., 2016). Importantly, however, Fig.S5b indicates that the single-aliquot OSL DRCs of our samples are better fitted using a saturating exponential plus linear function, which permits reasonably precise $D_e$ calculation over high dose ranges exceeding the $2D_0$ limit. An additional linear or second exponential growth component has been widely observed in previous studies, but the reliability of multi-grain OSL dating over high dose ranges is still debated (e.g., Arnold et al., 2016). For instance, Murray et al. (2008) and Pawley et al. (2008) reported ages derived from an additional linear component in the high dose region ($D_e$values up to 400 Gy), which were consistent with independent age control. In contrast, several other studies have reported significant multi-grain OSL age underestimation when deriving natural doses from the linear high dose region (e.g. Lowick et al., 2010; Timar et al., 2010; Chapot et al., 2012). These variable outcomes suggest that the reliability of multi-grain OSL dating over high dose ranges is sample dependent. The consistent replicate ages obtained using quartz OSL and other single-aliquot protocols in this study (Fig. 9) seems to suggest that suitable OSL ages can be derived from the linear high dose region for the Lake Eyre samples. This is further supported by the single-grain dating study performed on sample LE14-1. The single-grain

TT-OSL age of 141 ± 12 ka for this sample is statistically indistinguishable from the corresponding single-grain OSL age of 126 ± 10 ka. The agreement between these two single-grain techniques suggests that the OSL age is not limited by either the effects of dose saturation (consistent with the low proportion of rejected saturated grains in this sample; Table S4) or inaccurate $D_e$ estimation over mean dose ranges of 150-200 Gy.

There is some debate about the thermal stability of the multi-grain TT-OSL signal over extended burial periods, with current evidence potentially suggesting inter-sample variations in electron retention lifetimes. Adamiec et al. (2010) reported a laboratory measured lifetime of 4.5 Ma at 10 °C for the TT-OSL signal of their samples. A similar TT-OSL lifetime was reported by Li and Li (2006; 3.9 Ma at 10 $^{o}$C), though both higher and lower multi-grain TT-OSL lifetimes have been reported elsewhere for different samples and different laboratory techniques (e.g., Shen et al., 2011: 0.24 Ma at 10 $^{o}$C; Brown and Forman, 2012: 943 Ma at 10 $^{o}$C). Several of these lifetime assessments suggest that, for some samples at least, the multi-grain TT-OSL signal is insufficiently stable for reliable dating over late or middle Pleistocene timescales, and thus it may be worth considering a thermal stability correction when calculating final TT-OSL ages. However, recently Arnold et al. (2015) summarised a global TT-OSL database of 82 known-age samples up to 1000 ka and found that the thermally uncorrected TT-OSL ages show good overall agreement with independent age control or comparative ages. This implies that the laboratory-derived TT-OSL trap parameters may not necessarily be representative for a large number of empirical dating samples; thus the need for a TT-OSL thermal instability correction should be assessed on a sample-by-sample basis.

In this study we did not directly measure the TT-OSL trap lifetime of our samples and we have not applied a pre-existing thermal stability correction to the final single-aliquot TT-OSL ages, owing to the large (typically unreported) uncertainties associated with published laboratory lifetime calculations and difficulties in assessing long-term average burial temperatures. However, for illustrative purposes, it is worth considering the effect of applying a hypothetical thermal stability correction to our TT-OSL datasets based on the trap parameters of Ademiec et al. (2010). The modern annual ground temperature at the Williams Point at depth of 1-5m is ~23-24°C according to Baggs (1983) (based on maximum and minimum average). Considering a lower average temperature during the last 230 ka, an assumed long-term average burial temperature of 20 °C was used for TT-OSL thermal stability correction, using a first order equation of Adamiec et al. (2010) and Duller et al. (2015) (see details in SI). The thermally corrected TT-OSL ages obtained using this method are ~10-25% higher than the corresponding uncorrected TT-OSL ages, but they are still consistent with the uncorrected TT-OSL ages at 1 or 2σ. Moreover, both the corrected and uncorrected TT-OSL ages are statistically indistinguishable from the replicate pIRIR ages of each sample at 2σ (Table S5). Therefore, these results appear to support the overall validity of our uncorrected multi-grain TT-OSL ages. It is acknowledged that the TT-OSL residual dose subtraction and thermal stability correction exert opposing effects on the final age; hence overestimation of the residual dose combined with over-correction of thermal instability may yield an apparently reliable age, and vice versa. However, we consider it unlikely that these potentially opposing effects could counteract each other for all six samples, particularly as the samples span a relatively broad age range.

Likewise, we have not applied a thermal stability correction to the single-grain TT-OSL age of LE14-1 because we cannot be confident that existing (multi-grain aliquot) laboratory lifetime predictions are of direct relevance to the specific grain populations isolated in our single-grain analysis. Arnold and Demuro (2015) have shown that multi-grain assessments of TL signal loss may provide limited insights into single-grain TT-OSL source trap lifetimes due to averaging effects, the dominance of grain populations that do not produce TT-OSL, and interference from slowly bleaching OSL components. Single-grain TT-OSL studies performed on known-age samples that contain thermally unstable grain populations have also revealed the presence of multiple dose components and enhanced $D_e$ scatter (e.g., Arnold et al., 2015; Arnold and Demuro, 2015); neither of these problems are apparent in the single-grain TT-OSL $D_e$ dataset of LE14-1.

In contrast to the single-aliquot OSL and TT-OSL dating results, the pIRIR ages are relatively straightforward to interpret vis-à-vis potential issues of signal saturation and long-term signal stability. For all of the LEWP1 core samples, the natural pIRIR signals lie well below the DRC saturation levels (e.g., Fig. S6b). The anomalous fading problem is also shown to be effectively circumvented by applying the MET-pIRIR procedure, as indicated by the negligible g-values for the 250 °C MET-pIRIR signal (Fig. 6b) and the presence of a $D_e$ plateau in the $D_e$-T plots (Figs. 7b and c). Based on these considerations, and the fact that the pIRIR procedure is the only technique that was systematically applied to all eleven of the

LEWP1 core samples, we place greatest emphasis on the pIRIR dating results for age evaluation purposes. However, we reiterate that, in general, the three multi-grain dating procedures used in this study all yield reliable dating results, and the quartz OSL and TT-OSL ages provide suitable cross-checks for the pIRIR ages. In addition to the multi-grain pIRIR ages for core LEWP1, we have included both the single-grain OSL and TT-OSL ages of sample LE14-1 in our final age considerations since (i) both are based on $D_e$ assessments made at the most fundamental (individual grain) scale and therefore have been exclusively derived from grain types that have demonstrably suitable luminescence characteristics, and (ii) both the OSL and TT-OSL methods are considered to provide equally reliable single-grain age estimates for this particular sample.

### 5.2. Refining the age framework using Bayesian modelling

In order to improve the precision of our chronological framework and to derive combined ages and sedimentation rates for individual depositional units, we have constructed a Bayesian age-depth model for the lacustrine sequence using OxCal v4.2 (Bronk Ramsey, 2009a). The Bayesian modelling approach incorporates relative stratigraphic information (priors) and numerical dating distributions (likelihoods) to generate combined (posterior) chronological datasets for specified events, depths, and units (e.g. Rhodes et al., 2003; Bronk-Ramsey et al., 2015). The Lake Eyre Williams Point Bayesian model was constructed using a Poisson process depositional model (*P_Sequence* model: Bronk-Ramsey, 2009a; Bronk-Ramsey and Lee, 2013), which allows for randomly variable deposition rates through the age-depth profile. For our sedimentary sequence, the base rigidity parameter ($k_0$ – which controls the ability of the model to respond to variations in the prior and likelihood data, and hence variations in deposition rate) was set to be 1 event per cm of sedimentation. This parameter was allowed to vary over a factor of $10^{-2}$ to $10^{2}$ (i.e., 0.01 to 100 events per cm) to accommodate any major fluctuations in deposition rate supported by the data. To generate a high-resolution age-depth model, posterior dated events were automatically interpolated at 1 cm intervals throughout the sequence. The *P_Sequence* model was run with the general *outlier* function (Bronk-Ramsey, 2009b), and prior outlier probabilities of 5% were equally assigned to all dating samples to identify potentially significant statistical outliers. Likelihood estimates that yielded posterior outlier probabilities >5% were not excluded from the final model but were proportionally down-weighted in the iterative Monte Carlo runs, thereby producing an averaged chronological model (Bronk-Ramsey, 2009b). As detailed in Section 5.1, the K-feldspar pIRIR ages of eight LEWP1 core samples were included as likelihoods (excluding samples LEWP 1.40 1.58 and 1.77, which exhibited potentially complicating dose rates), along with the weighted average single-grain OSL and TT-OSL age of LE14-1. The latter was calculated using the *combine* function after excluding all shared systematic error terms, following Hammet al. (2016). The additional component of shared systematic uncertainty was subsequently added in quadrature to the combined age for LE14-1, yielding a weighted average optical age of 131.6 ± 9.1 ka for Bayesian modelling purposes.

Two modelling scenarios were tested for the lacustrine sequence: Model 1 (continuous deposition scenario) assumes continuous lacustrine deposition through time without any major hiatuses or erosional events between identified sedimentary units; whereas Model 2 (non-continuous deposition scenario) does not presume continuous lacustrine deposition, and is able to accommodate potential hiatuses and / or erosional discontinuities between the various sedimentary units. Unit boundary depths were kept the same in both models for consistency (as in Table 1). The OxCal *date* and *difference* functions (Bronk-Ramsey, 2009a) were used to calculate the age / duration of each stratigraphic unit and potential hiatuses between sedimentary deposits (Model 2), using the posterior probabilities of the upper and lower boundaries. Further details about running the two models are given in SI.

The calculated age ranges of each stratigraphic unit reveal relatively minor differences between the two modelling scenarios (results for Model 1are summarised in Table S6, Table S7 and Fig.S12; results for Model 2 are summarised in Table 3, Fig. 10 and Table S7). The main difference between the two modelling results is the identification of a potential 23 ka depositional hiatus between Units D and C (181-158 ka) in Model 2 (see below). In order to assess the statistical validity of the modelling results, we have used the model agreement index ($A_{model}$), which measures the overlap between the measurement data and the modelled posterior distributions as a whole, and the overall agreement index ($A_{overall}$), which is a product of the individual agreement indices ($A_i$: correspondence between individual likelihood and posterior distributions) for each modelled dating sample (Bronk-Ramsey, 2009a) (see details in SI). The higher $A_{model}$ and $A_{overall}$ values of 71 and 76% for Model 2 compared to corresponding values of 46 and 55% for Model 1 indicate the former has a better agreement with the original chronological data.

We favour Model 2 for reconstructing the final lacustrine chronological sequence at Williams Point based on its superior diagnostic indicators, and the fact that the stratigraphic assumption of this model (a probable discontinuous deposition) is in better accordance with sedimentological interpretations for the LEWP1 core and the broader Lake Eyre record (Magee et al., 1995; Cohen et al., 2015). The Bayesian modelling results for Model 2 (Table 3, Fig. 10) show that the 1σ ranges of the posterior likelihood distributions are reduced by an average of 34% for this model when compared with the original dating sample uncertainties. Minor stratigraphic reversals in the original likelihood distributions have also been refined in accordance with the specified modelling priors. The model returned mean boundary ages of 221.3 ± 18.8 ka to 200.6 ± 10.3 ka for the basal transgressive sediments (Unit E), 191.1 ± 8.6 ka to 180.8 ± 9.0 ka for the finely laminated deep-water lacustrine phase (Unit D), 157.8 ± 10.9 ka to 142.8 ± 14.5 ka for the palaeo-playa deposits (Unit C), and 130.0 ± 16.4 ka to 113.1 ± 19.8 ka for the upper part of the lacustrine unit, representing shallowing water conditions (Unit A) (Table 3). It is noteworthy that Model 2 has identified several potential gaps between different sedimentary units (Fig. 10 and Table 3). However, only one of these time gaps (the gap between Units C and D) is considered statistically significant at the 95% confidence level according to the OxCal *difference* query. The other age gaps are not statistically significant at the 95% CI, and thus represent potential periods of non-deposition that cannot be resolved beyond our existing dating uncertainties and / or reflect gaps in the temporal coverage of our empirical likelihood datasets. The changes in stratigraphy and presence of a sharpstratigraphic/sedimentological boundary between Units D and C (Fig.3) support the general validity of the temporal gap identified by Model 2. From a geological perspective, it has been suggested previously that deflation events can happen at Lake Eyre, which would result in a discontinuous preserved sedimentary record (e.g. Magee et al., 1995, 2004). In contrast to the Unit C and Unit D boundary, the upper boundary of Units E and the lower boundary of Unit D are considered to be chronologically consistent at 68% CI. Again, this modelling outcome is consistent with field observations as the core sediments suggest a gradual transition from the previous transgressive phase into the deep-water lacustrine stage (Fig. 3), as previously highlighted by Magee et al. (1995). Therefore, we interpret that deposition between Unit E and Unit D was either broadly continuous, or was separated by a relatively minor hiatus that was shorter than the uncertainties on our likelihoods and posterior boundary age distributions.

The average sedimentation rates of these four units (from bottom to top) are 0.04, 0.26, 0.03 and 0.22 m/ka using the posterior boundary age distributions, suggesting that deposition was relatively fast during both the deep-water and shallow-water lacustrine phases (Fig. 10).

### 5.3. Chronology and correlation of lacustrine sequences in Lake Eyre

To date, the most comprehensive sedimentological study of the Madigan Gulf was undertaken by Magee et al. (1995), as part of the decade-long Salt Lakes, Evaporites and Aeolian Deposits (SLEADS) program. In that study, Magee et al. (1995) attempted correlation of different lacustrine cores on sedimentological grounds (see positions of the cores in Fig. 2a). However, they identified the need for direct numerical dating of lacustrine sediments in the Madigan Gulf – an issue that has been addressed in the current study for part of the original research area. A number of fundamental insights into Lake Eyre were provided by the SLEADS program, including the depth to the Miocene Etadunna Formation, the presence of finely laminated lacustrine sediment sequences, and the presence and thickness of a buried halite layer in the central part of the playa. Earlier interpretations invoked that the buried halite layer (0.5 – 1.0 m thick) was Last Glacial Maximum (LGM) in age and that the underlying laminated lacustrine sequences were MIS 5 in age. Our numerical dating study has shown that the transgressive clayey sand that overlies the Miocene Etadunna Formation are 221 – 201 ka (MIS 7). These latest chronological results suggest that earlier $^{14}C$ ages obtained on the lacustrine sequences were most likely contaminated with modern carbon.

Deflation has previously been presented as an important mechanism for explaining the morpho-stratigraphic relationships in Lake Eyre, including the raised elevation of lacustrine sequences on the playa margin (King, 1955; Magee et al., 1995) and the uniformity of the truncated laminated lacustrine sequence in the playa at – 17.4 m AHD (Magee et al., 1995). It is possible that the playa muds dated in the upper part of LEWP1 core (late MIS 6; 158-143 ka) correlate with playa muds recorded at other core locations in Madigan Gulf. These playa muds in central Madigan Gulf also underlie a one metre halite crust, which suggest that one or both of these units correspond to the drying of Lake Eyre in late MIS 6. The lack of laminated lacustrine material in the central playa and the absence of the halite unit in LEWP1 or LEWP2 suggests that the upper part of the lacustrine sequence (Unit A: -9.9 m to -13.6 m

AHD; 130-113 ka) may have been removed from the central playa in subsequent deflationary episodes, potentially during the LGM when the buried halite was formed. This scenario however would require up to 6 – 7 m of deflation since the deposition of the upper part of the lacustrine sequence.

It is clear, however, that our ages of the transgressive clayey sand (Unit E) suggest that any deflation to the Miocene Etadunna formation occurred prior to MIS 7. This implies either a major erosional event in MIS 8–7 that removed pre-existing lacustrine material or, alternatively, there was a period of non-deposition lasting from ~5 Ma to ~220 ka. The latter, however, seems improbable based on the presence of the widespread fluvio-lacustrine sequences of both the Tirari, Kutjitara and Katipiri formations that are Pliocene-Pleistocene in age (Tedford et al., 1992; Nanson et al., 2008). Indeed, the presence of lacustrine material > 264 ± 26 ka (Miller et al., 2016) at the nearby Fly Lake (30 km NNE of our core location; Fig. 2a) suggests that lacustrine facies of the same age, or older than those we examined, overly the Etadunna Formation. The question therefore becomes whether Madigan Gulf obtained its modern position and geometry in MIS 8–7 onwards or whether indeed widespread deflation/erosion of the lacustrine material occurred in MIS 8.

Our new chrono-stratigraphic sequence, particularly the absence of preserved post-MIS 5 lacustrine deposits on the playa margin at Madigan Gulf, also support the interpretation that playa deposition within the last glacial cycle would have been restricted to the central playa alone or elsewhere in Lake Eyre. The lack of evidence for lake-floor deposition during the MIS 5 – 3 mega-lake phases of Magee et al., (2004) or Cohen et al. (2015) may suggest that these high lake-stands were either short-lived mega-lake phases or that deposition in these intervals occurred in other localities (either Belt Bay or proximal to the main tributaries of the Warburton and Cooper Creek; *sensu* Dulhunty, 1989). Alternatively, a third possibility is that lake-floor deposits from MIS 5 – 3 have subsequently been removed from the central playa in MIS 2 during any lake-floor deflation.

### 5.4. Late Quaternary palaeohydrological history for Lake Eyre based on the Williams Point records and Cohen et al. (2015)

The new chronostratigraphy of the Williams Point sequence can be combined with the recently published palaeo-shoreline chronology (Cohen et al., 2015) to reconstruct a new lake-full history of Lake Eyre in the late Quaternary. These results suggest a highly variable palaeohydrological history since the onset of lake deposition, which can be broadly divided into six stages based on fluctuating lake/water depth (Figs. 11a-f, Figs.12a and b).

***MIS 7 transgressive stage*** *(221 ± 19 ka to 201 ± 10 ka, Fig. 11a)*: The onset of a major lacustrine phase is marked by the deposition of the basal transgressive clayey sand at Williams Point estimated to have occurred between 221 ± 19 ka to 201 ± 10 ka. The poorly laminated structure and coarser grain size of the transgressive sediments, together with the absence of a coeval high palaeoshore record for Lake Eyre, potentially indicate a shallow water deposition environment at this time. During the same period, alluvial activity in the Lake Eyre Basin and northern Australia was pronounced, as indicated by abundant dated alluvium deposits in the region (Katipiri Formation, Nanson et al., 1992; 2008). The relatively wet climate and increased runoff may have triggered a transition from lake-floor deflation to accretion after 220 ka, forming the late Quaternary and Miocene unconformity at the bottom of the Williams Point sequence.

***Early MIS 6 deep-water lacustrine stage*** *(191 ± 9 ka to 181 ± 9 ka, Fig. 11b):* From late MIS 7 to early MIS6, the sediments at the Williams Point represent a transition from transgressive phase into a deep-water lacustrine phase. The presence of a major lacustrine phase in early MIS 6 was marked by deposition of a thick sequence of finely laminated clay (Unit D3-D1) at Williams Point between 191 ± 9 ka and 181 ± 9 ka. The thickness and uniqueness of this sedimentary layer suggests perennial lacustrine conditions of sufficient depths to allow salinity stratification. Currently there are no dated palaeo-shorelines of Lake Eyre correlating to this lacustrine phase, which may well be due to poor preservation of these shoreline sediments (now masked by an aeolian mantle). However, it is feasible that the undated shorelines around the lake, such as those near Muloorina at ~25 m and ~35 m AHD (Nanson et al., 1998), may correlate to the MIS 6 lacustrine phase recorded at Williams Point. In monsoon-influenced northern Australia, Bowler et al. (1998, 2001) have reported lake expansion periods for Lake Woods and Lake Gregory at 180 ka and 200 ka, respectively. Both of these lake expansion events are comparable in age with the lacustrine sediments in Lake Eyre.

***__Late MIS 6 playa stage__*** *(158 ± 11 ka to 143 ± 15 ka, Fig. 11c):* The Bayesian modelling in this study has identified a potential depositional hiatus in mid MIS 6. The presence of the muddy playa unit (Unit C), which we term the palaeo-playa, indicates that the late MIS 6 lake level was much lower than during early MIS 6. The absence of high beach ridges in Lake Eyre (Cohen et al., 2015), Lake Woods (Bowler et al., 1998) and Lake Gregory (Bowler et al., 2001) during this period all suggest that late MIS 6 was a relatively dry interval in monsoon-influenced northern Australia.

***__MIS 5 deep- and shallow-water oscillating stage 1__*** *(130 ± 16 ka to 69 ± 10 ka, Fig. 11d):* A synthesis of the Williams Point sequence (Unit A) and published palaeo-shoreline records indicate that the lake-level of Lake Eyre was highly variable during MIS 5; although the available chronological data remain discrete, and the resolution of existing age control is not sufficient enough to further precisely differentiate the timing of individual wet and dry phases. The earliest sub-stage of MIS 5 (MIS 5e), which represents the temperature and sea level maxima of the last interglacial, is characterised by a shallow-water lacustrine unit at the bottom of the Williams Point cliff (Unit A) however no high palaeoshorelines of equivalent age have been dated in this time interval.. During MIS 5b to MIS 5a, Williams Point records an oscillating deep- and shallow-water lacustrine or fluvio-deltaic phase (TL/AAR dated between 92 ± 7 ka and 69 ± 10 ka by Magee et al., 1995). Three lake-full phases in MIS 5d to MIS 5a were marked by around +10 m AHD beach ridges aged at 108 ± 5 ka, 94 ± 4 ka and 79 ± 4 ka respectively (Fig. 12b), indicating the lake has attained high-stand lake-full status (~25 m deep) during middle to late MIS 5. The high lake-levels of Lake Eyre in middle to late MIS 5 are in accordance with the highest beach ridges of Lake Woods at 96 ka (Bowler et al., 1998), Lake Gregory at 100 ka (Bowler et al., 2001) and Lake Frome at 110-88 ka (Cohen et al., 2011; 2012). Reeves et al. (2008) also reported marked fluvial activity at the Gulf of Carpentaria during MIS 5d and 5a. Similarly, Nanson et al. (2008) reported that the most widespread fluvial deposition event in northern Australia during the last glacial cycle occurred between 120 and ~ 80 ka (another phase of the Katipiri Formation). These results collectively indicate that the wettest phase of the last glacial cycle was between middle and late MIS5, rather than early MIS 5 as has been previously suggested (e.g. Magee et al., 1995).

***Early MIS 3 deep- and shallow-water oscillating stage 2*** *(60 ± 2 ka to 48 ± 2 ka, Fig. 11e):* Sedimentary records for MIS 4 are relatively rare for Lake Eyre itself, which may indicate a variable climate or one dominated by shorter-lived extremes. A range of +5 m AHD beach ridges have been dated to 60 ± 2 ka, 56 ± 2 ka and 48 ± 2 ka (Fig. 12b), suggesting that the lake had reached high levels in early MIS 3, but not as high as that of MIS 5. Beach ridges formed during early MIS 3 have also been discovered at Lake Woods and Lake Gregory (Bowler et al., 1998, 2001), while there is also evidence for a pluvial episode in northern Australia at this time (Nanson et al., 2008). For all of these lake catchments, the early MIS 3 palaeoshoreline levels are lower than their middle to late MIS 5 counterparts, indicating that early MIS 3 was not as wet as middle to late MIS 5 and was also characterised by widespread dune building phases in the Strzelecki and Tirari Deserts (Fitzsimmons et al., 2007).

***Middle MIS 3 and onwards – playa dominated stage*** *(<48 ka, Fig. 11f):* After early MIS 3, the lake entered a prolonged drying phase. There is no evidence for beach ridges significantly above the modern lake filling range after 48 ka, and the lake appears to have been dominated by playa conditions until the present, with only minor episodic filling events (Cohen et al., 2015).

In summary, the palaeohydrological history of Lake Eyre reflects an overall drying trend with oscillating wet phases since MIS 7, which agrees well with various landscape and floristic records on or around the continent (e.g. Bowler, 1982; Kershaw et al. 2003; 2007b; Nanson et al., 2008). Importantly, our results show that Australia's wet episodes can be linked to both glacial and interglacial periods. This represents a significant advancement in understanding over early studies, which have suggested that aridity in Australia is generally associated with glacial intervals whereas humidity is associated with interglacials (e.g. Nanson et al., 1992; Croke et al., 1999; Hesse et al., 2004; Magee et al., 2004; Kershaw et al., 2003; 2007a). In the last two decades, an expanding dataset has shown that the wetting and drying of northern and central Australia are not necessarily in phase with temperature changes (e.g. Kershaw and Nanson, 1993; van der Kaars et al., 2006; Moss and Kershaw, 2007; Nanson et al., 2008; Fitzsimmons et al., 2013; Cohen et al., 2015). The most distinct evidence for this trend is a lack of substantial lake expansion in MIS 5e and the Holocene, the two warmest time periods recorded in the last 200 ka. This growing evidence suggests a more complicated driving force for moisture delivery to north and central Australia and highlights the long-term dynamics of the Indo-Australian monsoon.

### 5.5. Implications for the drivers of Indo-Australian monsoon

The main driving force of the Indo-Australian monsoon remains controversial. Some palaeoclimate model experiments (Chappell and Syktus, 1996; Wyrwoll and Valdes, 2003; Wyrwoll et al., 2007) and pollen records (Kershaw et al., 2003) have suggested a dominant control of Southern Hemisphere summer insolation on the intensity of the monsoon. In contrast, other modelling studies (e.g. Miller et al., 2005) have argued for a Northern Hemisphere insolation dominant pattern, which takes effect through the strengthening and weakening of air out flowing from the Siberian High. The importance of variations in sea-level and sea surface temperature has also been identified by some studies as a fundamental driver for the strength of the monsoon (Marshall and Lynch, 2008; Griffiths et al., 2009; Denniston et al., 2013). At a millennial timescale, high resolution records from stalagmite and marine sediments in Indonesia (Griffiths et al., 2009; Muller et al., 2012; Ayliffe et al., 2013), northwest Australia (Denniston et al., 2013) and records from Lynch's Crater in northeast Australia (Turney et al., 2004; Muller et al., 2008) have documented several Indo-Australian monsoon intensification events coinciding with cold intervals in the North Atlantic (such as Henrich stadials and the Younger Dryas), a response that is anti-phased with the East Asian summer monsoon. This phenomenon was explained as a result of a southward shift of the Intertropical Convergence Zone (ITCZ) during the cooling episodes of the high northern latitudes, leading to an austral displacement of the Indo-Australian monsoon and a weakening (strengthening) of the East Asian summer (winter) monsoon (e.g. Muller et al., 2008; Griffiths et al., 2009; Denniston et al., 2013).

The new chronology for Lake Eyre allows for a more robust and absolute comparison of peak wet phases with other long climate records, and to assess the possible driving force for the Indo-Australian monsoon. These new chronologies are compared with the January insolation at 15°S (a latitude that represents current oceanic moisture sources for the Indo-Australian monsoon), the Antarctic temperature record, and the East Asian summer monsoon stalagmites records in China (which records both orbital forcing of the north hemisphere and sub-orbital millennial-scale events) in Fig. 12. Enhanced monsoon events, as indicated by the deep-water lacustrine sediments at Williams Point or the elevated palaeoshorelines (grey bars in Fig. 12), correlate poorly with summer insolation maxima in tropical Australia (Fig. 12c), suggesting Southern Hemisphere summer insolation is a poor predictor for the Indo-Australian monsoon. When compared with the Antarctic temperature record (Fig. 12 d), both the early deep-water phase (MIS 6) and the later megalake episodes suggest the wettest periods are broadly in accordance with the intervening periods between the glacial and interglacial maximums, and that peak inter-glacial conditions show limited evidence of peak effective runoff. This observation implies that the Sothern Hemisphere temperature may have an impact on the Indo-Australian monsoon, but clearly it is not the first order forcing. The correlation with the East Asian summer monsoon minima or maxima, which are mainly controlled by the Northern Hemisphere forcing, is also apparently ambiguous (Fig. 12e).

One interesting observation is that when comparing the high lake-level episodes with millennial-scale events, all of the six high megalake episodes are very well correlated with cold intervals in the North Atlantic, as recorded by weakened summer monsoon in Chinese stalagmite records (Fig. 12e). From young to old, the six palaeoshoreline records coincide with Heinrich Stadial 5, ice rafted debris (IRD) layer C-14 registered in North Atlantic marine sediment cores, Heinrich Stadial 6, IRD layer C-20, IRD layer C-22 and IRD layer C-23, respectively (Chapman and Shackleton, 1999; Rasmussen et al., 2003). The deep-water lacustrine layer at Williams Point is also synchronous with an episode when the East Asia summer monsoon was generally weak. This situation is consistent with other tropical Southern Hemisphere high resolution records from the last glacial cycle (Griffiths et al., 2009; Muller et al., 2012; Ayliffe et al., 2013; Denniston et al., 2013), demonstrating a linked, coeval but anti-phased reaction of the bi-hemispheric monsoon systems to the North Atlantic cooling and southward displacement of ITCZ. The results in Fig.12 may indicate that the Indo-Australian monsoon (or potentially just the Lake Eyre record) might be more sensitive to abrupt millennial-scale climate change than orbital forcing. Although the current dataset is not large enough to draw a definitive conclusion, our results highlight the potential role of the Northern Hemisphere high latitudes and the global monsoon system in influencing the Indo-Australian monsoon is an area warranting further primary evidence.

It is also interesting to note that the Lake Eyre lake-full or wet episodes also show some consistency with high precipitation episodes in southern Australia, a region considered less influenced by the monsoon system. In southeast Australia, speleothems from Naracoorte have documented high precipitation periods between 40-50 ka, 70-85 ka, 90-100 ka, 105-115 ka and 155-220 ka (Ayliffe et al., 1998), which are generally coincident with the lake expansion episodes for Lake Eyre. Ayliffe et al. (1998) also argued that the highest effective precipitation for the southeastern interior of Australia occurred during stadials and cool interstadials of the past four glacial cycles, consistent with the palaeohydrological records of Lake Eyre. These coincidences may indicate a close connection between the precipitation driving forces for the north and south of the continent. Expanding this latitudinal investigation of Australia's now dry lakes will allow a better examination of coupling or lack thereof across regions of the Australian continent.

## 6. Summary and Conclusions

Luminescence dating of lake-floor and cliff exposure sediments at Williams Point has shown that the sedimentary record for Lake Eyre extends back to MIS 7. Our new chronology indicates that the thick deep-water lacustrine sediments near Williams Point, which are interpreted as representing an extreme wet phase of Lake Eyre, were deposited in early MIS 6 (181-191 ka), rather than during the last interglacial maximum (MIS 5e) as previously assumed. Our results show that the wet phases of Australia's arid interior occurred during both glacial and interglacial periods, and reflect enhancement of the Indo-Australian monsoon. Our data, based on an improved chronology, shows that Southern Hemisphere orbital forcing may not be a first order driving force for the long-term dynamics of the Lake Eyre basin or the Indo-Australian monsoon. Rather, the high lake-level events of Lake Eyre exhibit a stronger correlation with millennial-scale cooling events and stadials of the North Atlantic, and coincide with weakened episodes/events for the East Asia summer monsoon. This implies an important role for the north high latitudes in influencing the Indo-Australian monsoon, which may take effect through the boreal or austral replacement of the ITCZ during warm and cool periods in the north Atlantic.

From a methodological perspective, our results demonstrate that K-feldspar pIRIR and quartz TT-OSL procedures have excellent potential for reconstructing the timing of wet and dry events in Australia during the late and middle Pleistocene. These approaches open up new possibilities for establishing expanded and higher resolution chronological dataset for the

Lake Eyre basin, and could form an important foundation for improved understanding of Quaternary climate change patterns and driving forces in Australia.


## Acknowledgements

This research was funded by the ARC (grant DP1096911 to TC and grant FT130100195 to LA). We thank Jan-Hendrik May for field assistance for the collection of LEWP1 and to Gerald Nanson, Richard Roberts, Zenobia Jacobs, Brian Jones, John Jansen, Bo Li and John Magee for constructive discussions. The LEWP2 core was part of an Honours thesis at the University of Wollongong by Jessica Couri.


## References


Adamiec, G., Duller, G.A.T., Roberts, H.M., Wintle, A.G., 2010. Improving the TT-OSL SAR protocol through source trap characterisation. Radiat. Meas. 45, 768–777.

Aitken, M.J., 1985. Thermoluminescence Dating. Academic Press, London.

Aitken, M.J., 1998. An Introduction to Luminescence Dating. Oxford University Press, London

Arnold, L.J., Demuro, M., 2015. Insights into TT-OSL signal stability from single-grain analyses of known-age deposits at Atapuerca, Spain. Quat. Geochronol. 30,472–478.

Arnold, L.J., Demuro, M., Navazo Ruiz, M., 2012a. Empirical insights into multi-grain averaging effects from ‘pseudo’ single-grain OSL measurements. Radiat. Meas. 47, 652–658.

Arnold, L.J., Demuro, M., Navazo Ruiz, M., Benito-Calvo, A., Pérez-González, A., 2013. OSL dating of the Middle Palaeolithic Hotel California site, Sierra de Atapuerca, north-central Spain. Boreas 42, 285–305.

Arnold, L.J., Demuro, M., Parés, J.M., Arsuaga, J.L., Aranburu, A., Bermúdez de Castro, J.M., Carbonell, E., 2014. Luminescence dating and palaeomagnetic age constraint on hominins from Sima de losHuesos, Atapuerca, Spain. J. Hum.Evol.67, 85–107.

Arnold, L.J., Demuro, M., Parés, J.M., Pérez-González, A., Arsuaga, J.L., Bermúdez de Castro, J.M., Carbonell, E., 2015. Evaluating the suitability of extended-range luminescence dating techniques over early and Middle Pleistocene timescales: Published datasets and case studies from Atapuerca, Spain. Quat. Int. 389, 167–190.

Arnold, L.J., Duval, M., Demuro, M., Spooner, N.A., Santonja, M., Pérez-González, A., 2016. OSL dating of individual quartz 'supergrains' from the Ancient Middle Palaeolithic site of Cuesta de la Bajada, Spain.Quat. Geochronol. 36, 78–101.

Arnold, L.J., Duval, M., Falguères, C., Bahain, J.-J., Demuro, M. 2012b. Portable gamma spectrometry with cerium-doped lanthanum bromide scintillators: Suitability assessments for luminescence and electron spin resonance dating applications. Radiat. Meas. 47, 6–18.

Arnold, L.J., Roberts, R.G., 2009. Stochastic modelling of multi-grain equivalent dose ($D_e$) distributions: Implications for OSL dating of sediment mixtures. Quat. Geochronol. 4, 204–230.

Arnold, L. J., Roberts, R. G., MacPhee, R. D. E., Haile, J. S., Brock, F., Möller, P., Froese, D. G., Tikhonov, A. N., Chivas, A. R., Gilbert, M. T. P., Willerslev, E., 2011. Paper II – Dirt, dates and DNA: OSL and radiocarbon chronologies of perennially frozen sediments in Siberia and their implications for sedimentary ancient DNA studies. Boreas 40, 417–445.

Arnold, L.J., Roberts, R.G., Macphee, R.D.E., Willerslev, E., Tikhonov, A.N., Brock, F., 2008. Optical dating of perennially frozen deposits associated with preserved ancient plant and animal DNA in north-central Siberia. Quat. Geochronol. 3, 114–136.

Arsuaga, J.L., Martínez, I., Arnold, L.J., Aranburu, A., Gracia-Téllez, A., Sharp, W.D., Quam, R.M., Falguères, C., Pantoja-Pérez, A., Bischoff, J., Poza-Rey, E., Parés, J.M., Carretero, J.M., Demuro, M., Lorenzo, C., Sala, N., Martinón-Torres, M., García, N., Alcázar de Velasco, A., Cuenca-Bescós, G., Gómez-Olivencia, A., Moreno, D., Pablos, A., Shen, C.-C., Rodríguez, L., Ortega, A.I., García, R., Bonmatí, A., Bermúdez de

Castro, J.M., Carbonell, E. 2014., Neanderthal roots: Cranial and chronological evidence from Sima de los Huesos. Science, 344, 1358–1363.
Auclair, M., Lamothe, M., Huot, S., 2003. Measurement of anomalous fading for feldspar IRSL using SAR. Radiat. Meas. 37, 487–492.
Ayliffe, L.K., Gagan, M.K., Zhao, J., Drysdale, R.N., Hellstrom, J.C., Hantoro, W.S., Griffiths, M.L., Scott-Gagan, H., Pierre, E.S., Cowley, J.A., Suwargadi, B.W., 2013. Rapid interhemispheric climate links via the Australasian monsoon during the last deglaciation. Nat.Commun. 4, 2908.
Ayliffe, L.K., Marianelli, P.C., Moriarty, K.C., Wells, R.T., McCulloch, M.T., Mortimer, G.E., Hellstrom, J.C., 1998. 500 ka precipitation record from southeastern Australia: Evidence for interglacial relative aridity. Geology 26, 147–150.
Baggs, S.A., 1983. Remote prediction of ground temperature in Australian soils and mapping its distribution. Solar Energy 30, 351–366.
Bailey, R.M., Arnold, L.J., 2006. Statistical modelling of single grain quartz De distributions and an assessment of procedures for estimating burial dose. Quat. Sci. Rev. 25, 2475–2502.
Berger, A., 1992, Orbital variations and insolation database: IGBP PAGES (International Geosphere Biosphere Programme Past Global Changes)/World Data Center for Paleoclimatology Data Contribution Series 92–007: Boulder, Colorado, National Oceanic and Atmospheric Administration/National Geophysical Data Center, World Data Center for Paleoclimatology Data,http://gcmd.nasa.gov/records/GCMD_EARTHLAND_NGDC_PALEOCLIM_INSOL.html
Bowler, J.M., 1982. Aridity in the late Tertiary and Quaternary of Australia. In W.R. Barker, W.R. & Greenslade, P. J. W. (eds) Evolution of the Flora and Fauna of Arid Australia. Peacock Publications, Adelaide, South Australia, pp. 35– 45.
Bowler, J.M., Duller, G. A. T., Perret, N., Prescott, J.R., Wyrwoll, K.-H., 1998. Hydrologic changes in monsoonal climates of the last glacial cycle: stratigraphy and luminescence dating of Lake Woods, N.T. Australia.Palaeoclimates3:179-207.
Bowler, J.M., Hope, G.S., Jennings, J.N., Singh, G., Walker, D., 1976. Late Quaternary climates of Australia and New Guinea. Quat. Res. 6, 359–394.
Bowler, J.M., Johnston, H., Olley, J.M., Prescott, J.R., Roberts, R.G., Shawcross, W., Spooner, N.A., 2003. New ages for human occupation and climatic change at Lake Mungo, Australia. Nature 421, 837–840.
Bowler, J.M., Wyrwoll, K.-H., Lu, Y., 2001. Variations of the northwest Australian summer monsoon over the last 300,000 years: the paleohydrological record of the Gregory (Mulan) Lakes System. Quat. Int. 83–85, 63–80.
Bronk Ramsey, C., 2009a. Bayesian analysis of radiocarbon dates. Radiocarbon 51, 337–360.
Bronk Ramsey, C., 2009b. Dealing with outliers and offsets in radiocarbon dating. Radiocarbon51, 1023–1045.
Bronk Ramsey, C., Lee, S., 2013. Recent and Planned Developments of the Program OxCal. Radiocarbon 55, 720–730.
Bronk Ramsey, C., Albert, P.G., Blockley, S.P.E., Hardiman, M., Housley, R.A., Lane, C.S., Lee, S., Matthews, I.P., Smith, V.C., Lowe, J.J., 2015. Improved age estimates for key Late Quaternary European tephra horizons in the RESET lattice. Quat. Sci. Rev. 118, 18–32.
Brown, N.D., Forman, S.L., 2012. Evaluating a SAR TT-OSL protocol for dating fine-grained quartz within Late Pleistocene loess deposits in the Missouri and Mississippi river valleys, United States. Quat. Geochronol. 12, 87–97.
Buylaert, J.P., Jain, M., Murray, A.S., Thomsen, K.J., Thiel, C., Sohbati, R., 2012. A robust feldspar luminescence dating method for Middle and Late Pleistocene sediments. Boreas 41, 435–451.
Buylaert, J.P., Thiel, C., Murray, A.S., Vandenberghe, D.A.G., Yi, S., Lu, H., 2011. IRSL and post-IR IRSL residual doses recorded in modern dust samples from theChinese Loess Plateau. Geochronometria 38, 432–440.
Chapman, M.R., Shackleton, N.J., 1999. Global ice-volume fluctuations, North Atlantic ice-rafting events, and deep-ocean circulation changes between 130 and 70 ka. Geology 27, 795–798.
Chappell, J., Syktus, J., 1996. Palaeoclimaticmodelling: A western Pacific perspective, in Giambelluca, T.W., and Henderson-Sellers, A., eds., Climate change: Developing Southern Hemisphere perspectives: Chichester, England, John Wiley and Sons, p. 175–194.
Chapot, M.S., Roberts, H.M., Duller, G.A.T., Lai, Z.P., 2012. A comparison of natural- and laboratory-generated dose response curves for quartz optically stimulated luminescence signals from Chinese Loess. Radiat. Meas. 47, 1045–1052.
Cheng, H., Edwards, R.L., Broecker, W.S., Denton, G.H., Kong, X., Wang, Y., Zhang, R., Wang, X., 2009. Ice Age Terminations. Science 326, 248–252.
Cohen, T.J., Nanson, G.C., Jansen, J.D., Jones, B.G., Jacobs, Z., Larsen, J.R., May, J.-H., Treble, P., Price, D.M., Smith, A.M., 2012. Late Quaternary mega-lakes fed by the northern and southern river systems of

central Australia: Varying moisture sources and increased continental aridity. Palaeogeogr. Palaeoclimatol. Palaeoecol., 356–357, 89–108.
Cohen, T.J., Jansen, J.D., Gliganic, L.A., Larsen, J.R., Nanson, G.C., May, J.-H., Jones, B.G., Price, D.M., 2015. Hydrological transformation coincided with megafaunal extinction in central Australia. Geology 43, 195–198.
Cohen, T.J., Nanson, G.C., Jansen, J.D., Jones, B.G., Jacobs, Z., Treble, P., Price, D.M., May, J.-H., Smith, A.M., Ayliffe, L.K., Hellstrom, J.C., 2011. Continental aridification and the vanishing of Australia's megalakes. Geology 39, 167–170.
Croke, J.C., Magee, J.W., Wallensky, E.P., 1999. The role of the Australian Monsoon in the western catchment of Lake Eyre, central Australia, during the Last Interglacial. Quat. Int. 57, 71–80.
Cupper, M.L., 2006. Luminescence and radiocarbon chronologies of playa sedimentation in the Murray Basin, southeastern Australia. Quat. Sci. Rev. 25, 2594–2607.
Demuro, M., Arnold, L.J., Parés, J.M., Sala, R., 2015. Extended-range luminescence chronologies suggest potentially complex bone accumulation histories at the Early-to-Middle Pleistocene palaeontological site of Huéscar-1 (Guadix-Baza basin, Spain). Quat. Int. 389, 191–212.
Demuro, M., Arnold, L.J., Parés, J.M., Pérez-González, A., Ortega, A.I., Arsuaga, J.L., Bermúdez de Castro, J.M., Carbonell, E., 2014. New luminescence ages for the Galería Complex archaeological site: Resolving chronological uncertainties on the Acheulean record of the Sierra de Atapuerca, northern Spain. PLOS ONE 9, e110169.
Demuro, M., Arnold, L.J., Froese, D.G., Roberts, R.G., 2013. OSL dating of loess deposits bracketing Sheep Creek tephra beds, northwest Canada: Dim and problematic single-grain OSL characteristics and their effect on multi-grain age estimates. Quat. Geochronol. 15, 67–87.
Denniston, R.F., Wyrwoll, K.-H., Asmerom, Y., Polyak, V.J., Humphreys, W.F., Cugley, J., Woods, D., LaPointe, Z., Peota, J., Greaves, E., 2013. North Atlantic forcing of millennial-scale Indo-Australian monsoon dynamics during the Last Glacial period. Quat. Sci. Rev. 72, 159–168.
Dulhunty, J.A. 1989. Levels, salt crusts and lake instability. In: Boynthon, C.W. and Fraser, A.S. (Eds) The great filling of Lake Eyre in 1974. Royal Geographical Society of Australasia (South Australia Branch), Adelaide, 56-59.
Duller, G.A.T., Tooth, S., Barham, L., Tsukamoto, S., 2015. New investigations at Kalambo Falls, Zambia: Luminescence chronology, site formation, and archaeological significance. J. Hum. Evol. 85, 111–125.
Duller, G.A.T., Wintle, A.G., 2012. A review of the thermally transferred optically stimulated luminescence signal from quartz for dating sediments. Quat. Geochronol. 7, 6–20.
English, P., Spooner, N.A., Chappell, J., Questiaux, D.G., Hill, N.G., 2001. Lake Lewis basin, central Australia: environmental evolution and OSL chronology. Quat. Int. 83–85, 81–101.
Fattahi, M., Stokes, S., 2000. Extending the time range of luminescence dating using red TL (RTL) from volcanic quartz. Radiat. Meas. 32, 479–485.
Fitzsimmons, K.E., Cohen, T.J., Hesse, P.P., Jansen, J., Nanson, G.C., May, J.-H., Barrows, T.T., Haberlah, D., Hilgers, A., Kelly, T., Larsen, J., Lomax, J., Treble, P., 2013. Late Quaternary palaeoenvironmental change in the Australian drylands. Quat. Sci. Rev. 74, 78–96.
Fitzsimmons, K.E., Rhodes, E.J., Magee, J.W., Barrows, T.T., 2007. The timing of linear dune activity in the Strzelecki and Tirari Deserts, Australia. Quat. Sci. Rev. 26, 2598–2616.
Fu, X., 2014. The De (T, t) plot: A straightforward self-diagnose tool for post-IR IRSL dating procedures. Geochronometria 41, 315–326.
Fu, X., Li, B., Li, S.H., 2012. Testing a multi-step post-IR IRSL dating method using polymineral fine grains from Chinese loess. Quat. Geochronol.10, 8–15.
Fu, X., Li, S.H., Li, B., 2015. Optical dating of aeolian and fluvial sediments in north Tian Shan range, China: Luminescence characteristics and methodological aspects. Quat. Geochronol. 30, 161–167.
Fu, X., Li, S.H., Li, B., Fu, B.H., 2017. A fluvial terrace record of late Quaternary folding rate of the Anjihai anticline in the northern piedmont of Tian Shan, China. Geomorphology 278, 91–104.
Fujioka, T., Chappell, J., 2010. History of Australian aridity: chronology in the evolution of arid landscapes. In: Bishop, P., Pillans, B. (Eds.), Australian Landscapes. Geological Society, London, pp. 121–139.
Galbraith, R.F., Roberts, R.G., Laslett, G.M., Yoshida, H., Olley, J.M., 1999. Optical Dating of Single and Multiple Grains of Quartz from Jinmium Rock Shelter, Northern Australia: Part I, Experimental Design and Statistical Models. Archaeometry 41, 339–364.
Gong, Z., Li, S.-H., Li, B., 2014. The evolution of a terrace sequence along the Manas River in the northern foreland basin of Tian Shan, China, as inferred from optical dating. Geomorphology 213, 201–212.
Griffiths, M.L., Drysdale, R.N., Gagan, M.K., Zhao, J., Ayliffe, L.K., Hellstrom, J.C., Hantoro, W.S., Frisia, S., Feng, Y., Cartwright, I., Pierre, E.S., Fischer, M.J., Suwargadi, B.W., 2009. Increasing Australian–Indonesian monsoon rainfall linked to early Holocene sea-level rise. Nature Geosci. 2, 636–639.

Guibert, P., Lahaye, C., Bechtel, F., 2009. The importance of U-series disequilibrium of sediments in luminescence dating: A case study at the Roc de Marsal Cave (Dordogne, France). Radiat. Meas. 44, 223–231.
Habeck-Fardy, A., Nanson, G.C., 2014. Environmental character and history of the Lake Eyre Basin, one seventh of the Australian continent. Earth Sci. Rev. 132, 39–66.
Hamm, G., Mitchell, P., Arnold, L.J., Prideaux, G.J., Questiaux, D., Spooner, N.A., Levchenko, V.A., Foley, E.C., Worthy, T.H., Stephenson, B., Coulthard, V., Coulthard, C., Wilton, S., Johnston, D., 2016. Cultural innovation and megafauna interaction in the early settlement of arid Australia. Nature, doi:10.1038/nature20125.
Hesse, P.P., Magee, J.W., van der Kaars, S., 2004. Late Quaternary climates of the Australian arid zone: a review. Quat. Int. 118–119, 87–102.
Hocknull, S.A., Zhao, J.X., Feng, Y.X, Webb, G.E., 2007. Responses of Quaternary rainforest vertebrates to climate change in Australia. Earth Planet. Sci. Lett. 264, 317–331.
Hu, G., Zhang, J.-F., Qiu, W.-L., Zhou, L.-P., 2010. Residual OSL signals in modern fluvial sediments from the Yellow River (HuangHe) and the implications for dating young sediments. Quat. Geochronol.5, 187–193.
Hua, Q., 2009. Radiocarbon: A chronological tool for the recent past. Quat. Geochronol. 4, 378–390.
Huntley, D.J., Lamothe, M., 2001. Ubiquity of anomalous fading in K-feldspars and the measurement and correction for it in optical dating. Can. J. Earth Sci. 38, 1093–1106.
Jain, M., 2009. Extending the dose range: Probing deep traps in quartz with 3.06 eV photons. Radiat. Meas. 44, 445–452.
Jain, M., Duller, G.A.T., Wintle, A.G., 2007. Dose response, thermal stability and optical bleaching of the 310 °C isothermal TL signal in quartz. Radiat. Meas. 42, 1285–1293.
Jouzel, J., Masson-Delmotte, V., Cattani, O., Dreyfus, G., Falourd, S., Hoffmann, G., Minster, B., Nouet, J., Barnola, J.M., Chappellaz, J., Fischer, H., Gallet, J.C., Johnsen, S., Leuenberger, M., Loulergue, L., Luethi, D., Oerter, H., Parrenin, F., Raisbeck, G., Raynaud, D., Schilt, A., Schwander, J., Selmo, E., Souchez, R., Spahni, R., Stauffer, B., Steffensen, J.P., Stenni, B., Stocker, T.F., Tison, J.L., Werner, M., Wolff, E.W., 2007. Orbital and Millennial Antarctic Climate Variability over the Past 800,000 Years. Science 317, 793–796.
Kars, R.H., Reimann, T., Ankjærgaard, C., Wallinga, J., 2014. Bleaching of the post-IR IRSL signal: new insights for feldspar luminescence dating. Boreas 43, 780–791.
Kershaw, A.P., Bretherton, S.C., van der Kaars, S., 2007a. A complete pollen record of the last 230 ka from Lynch's Crater, north-eastern Australia. Palaeogeogr. Palaeoclimatol. Palaeoecol., 251, 23–45.
Kershaw, A.P., McKenzie, G.M., Porch, N., Roberts, R.G., Brown, J., Heijnis, H., Orr, M.L., Jacobsen, G., Newall, P.R., 2007b. A high-resolution record of vegetation and climate through the last glacial cycle from Caledonia Fen, southeastern highlands of Australia. J. Quaternary Sci. 22, 481–500.
Kershaw, A.P., Nanson, G.C., 1993. The last full glacial cycle in the Australian region. Glob. Planet. Change. 7, 1–9.
Kershaw, A.P., van der Kaars, S., Moss, P.T., 2003. Late Quaternary Milankovitch-scale climatic change and variability and its impact on monsoonal Australasia. Marine Geology 201, 81–95.
King, D. 1955. The Quaternary stratigraphic record at Lake Eyre North and the evolution of existing topographic forms. Trans. R. Soc. South Aust.79, 93-103.
Kotwicki, V., Allan, R., 1998. La Niña de Australia — contemporary and palaeo-hydrology of Lake Eyre. Palaeogeogr. Palaeoclimatol. Palaeoecol. 144, 265–280.
Krbetschek, M.R., Rieser, U., Zöller, L., Heinicke, J., 1994. Radioactive disequilibria in palaeodosimetric dating of sediments. Radiat. Meas. 23, 485–489.
Li, B.,Li,S.H., 2006. Studies of thermal stability of charges associated with thermal transfer of OSL from quartz. J. Phys. D Appl. Phys.39, 2941–2949.
Li, B., Li, S.H., 2011. Luminescence dating of K-feldspar from sediments: A protocol without anomalous fading correction. Quat. Geochronol. 6, 468–479.
Li, B., Roberts, R.G., Jacobs, Z., Li, S.-H., 2015a. Potential of establishing a "global standardised growth curve" (gSGC) for optical dating of quartz from sediments. Quat. Geochronol. 27, 94–104.
Li, B., Roberts, R.G., Jacobs, Z., Li, S.-H., Guo, Y.-J., 2015b. Construction of a "global standardised growth curve" (gSGC) for infrared stimulated luminescence dating of K-feldspar. Quat. Geochronol. 27, 119–130.
Li, B., Jacobs, Z., Roberts, R.G., Li, S.-H., 2014a. Review and assessment of the potential of post-IR IRSL dating methods to circumvent the problem of anomalous fading in feldspar luminescence. Geochronometria 41, 178–201.
Li, G., Jin, M., Wen, L., Zhao, H., Madsen, D., Liu, X., Wu, D., Chen, F., 2014b. Quartz and K-feldspar optical dating chronology of eolian sand and lacustrine sequence from the southern Ulan Buh Desert, NW China: Implications for reconstructing late Pleistocene environmental evolution. Palaeogeogr. Palaeoclimatol. Palaeoecol. 393, 111–121.

Lowick, S.E., Preusser, F., Pini, R., Ravazzi, C., 2010. Underestimation of fine grain quartz OSL dating towards the Eemian: Comparison with palynostratigraphy from Azzano Decimo, northeastern Italy. Quat. Geochronol. 5, 583–590.

Lowick, S.E., Trauerstein, M., Preusser, F., 2012. Testing the application of post IR-IRSL dating to fine grain waterlain sediments. Quat. Geochronol. 8, 33–40.

Magee, J.W., Bowler, J.M., Miller, G.H., Williams, D.L.G., 1995.Stratigraphy, sedimentology, chronology and palaeohydrology of Quaternary lacustrine deposits at Madigan Gulf, Lake Eyre, south Australia. Palaeogeogr. Palaeoclimatol. Palaeoecol. 113, 3–42.

Magee, J.W., Miller, G.H., 1998. Lake Eyre palaeohydrology from 60 ka to the present: beach ridges and glacial maximum aridity. Palaeogeogr. Palaeoclimatol. Palaeoecol. 144, 307–329.

Magee, J.W., Miller, G.H., Spooner, N.A., Questiaux, D., 2004. Continuous 150 k.y. monsoon record from Lake Eyre, Australia: Insolation-forcing implications and unexpected Holocene failure. Geology 32, 885.

Marshall, A.G., Lynch, A.H., 2008. The sensitivity of the Australian summer monsoon to climate forcing during the late Quaternary. J. Geophys. Res. 113, D11107. doi:10.1029/2007JD008981

Martinson, D.G., Pisias, N.G., Hays, J.D., Imbrie, J., Moore, T.C., Shackleton, N.J., 1987. Age dating and the orbital theory of the ice ages: Development of a high-resolution 0 to 300,000-year chronostratigraphy. Quat. Res. 27, 1–29.

May, J.H., Wells, S.G., Cohen, T.J., Marx, S.K., Nanson, G.C., Baker, S.E., 2015. A soil chronosequence on Lake Mega-Frome beach ridges and its implications for late Quaternary pedogenesis and paleoenvironmental conditions in the drylands of southern Australia. Quat. Res. 83, 150–165.

Miller, G.H., Fogel, M.L., Magee, J.W., Gagan, M.K., 2016. Disentangling the impacts of climate and human colonization on the flora and fauna of the Australian arid zone over the past 100 ka using stable isotopes in avian eggshell. Quat. Sci. Rev. 151, 27–57.

Miller, G., Mangan, J., Pollard, D., Thompson, S., Felzer, B., Magee, J., 2005. Sensitivity of the Australian Monsoon to insolation and vegetation: Implications for human impact on continental moisture balance. Geology 33, 65. doi:10.1130/G21033.1

Moss, P.T., Kershaw, A.P., 2007. A late Quaternary marine palynological record (oxygen isotope stages 1 to 7) for the humid tropics of northeastern Australia based on ODP Site 820. Palaeogeogr. Palaeoclimatol. Palaeoecol.251, 4–22.

Muller, J., Kylander, M., Wüst, R.A.J., Weiss, D., Martinez-Cortizas, A., LeGrande, A.N., Jennerjahn, T., Behling, H., Anderson, W.T., Jacobson, G., 2008. Possible evidence for wet Heinrich phases in tropical NE Australia: the Lynch's Crater deposit. Quat. Sci. Rev. 27, 468–475.

Muller, J., McManus, J.F., Oppo, D.W., Francois, R., 2012. Strengthening of the Northeast Monsoon over the Flores Sea, Indonesia, at the time of Heinrich event 1. Geology 40, 635–638.

Murray, A., Buylaert, J.-P., Henriksen, M., Svendsen, J.-I., Mangerud, J., 2008. Testing the reliability of quartz OSL ages beyond the Eemian. Radiat. Meas.43, 776–780.

Murray, A.S., Marten, R., Johnston, A., Martin, P., 1987. Analysis for naturally occuring radionuclides environmental concentrations by gamma spectrometry. J. Radioanal. Nucl. Chem. 115, 263–288.

Murray, A.S., Thomsen, K.J., Masuda, N., Buylaert, J.P., Jain, M., 2012. Identifying well-bleached quartz using the different bleaching rates of quartz and feldspar luminescence signals. Radiat. Meas. 47, 688–695.

Murray, A.S., Wintle, A.G., 2000.Luminescence dating of quartz using an improved single-aliquot regenerative-dose protocol. Radiat. Meas. 32, 57–73.

Murray, A.S., Wintle, A.G., 2003. The single aliquot regenerative dose protocol: potential for improvements in reliability. Radiat. Meas. 37, 377–381.

Nanson, G.C., Price, D.M., Jones, B.G., Maroulis, J.C., Coleman, M., Bowman, H., Cohen, T.J., Pietsch, T.J., Larsen, J.R., 2008. Alluvial evidence for major climate and flow regime changes during the middle and late Quaternary in eastern central Australia. Geomorphology101, 109–129.

Nanson, G.C., Price, D.M., Short, S.A., 1992. Wetting and drying of Australia over the past 300 ka. Geology 20, 791–794.

Ollé, A., Vergès, J.M., Rodríguez, X.P., Cáceres, I., Angelucci, D.E., Vallverdú, J., Demuro, M., Arnold, L.J.,Falguères, C., Bennàsar, M., López-García, J.M., Blain, H-.A., Bañuls-Cardona, S., Burjachs, F., Expósito, I., López-Polín1, L., López-Ortega, E., 2016. The Middle Pleistocene site of La Cansaladeta (Tarragona, Spain): Stratigraphic and archaeological succession. Quat. Int. 393, 137-157.

Olley, J.M., Murray, A., Roberts, R.G., 1996. The effects of disequilibria in the uranium and thorium decay chains on burial dose rates in fluvial sediments. Quat. Sci. Rev. 15, 751–760.

Olley, J.M., Roberts, R.G., Murray, A.S., 1997. Disequilibria in the uranium decay series in sedimentary deposits at Allen's cave, nullarbor plain, Australia: Implications for dose rate determinations. Radiat. Meas. 27, 433–443.

Pawley, S.M., Bailey, R.M., Rose, J., Moorlock, B.S.P., Hamblin, R.J.O., Booth, S.J., Lee, J.R., 2008. Age limits on Middle Pleistocene glacial sediments from OSL dating, north Norfolk, UK. Quat. Sci. Rev. 27, 1363–1377.
Preusser, F., Degering, D., 2007. Luminescence dating of the Niederweningen mammoth site, Switzerland. Quat. Int. 164–165, 106–112.
Reeves, J.M., Barrows, T.T., Cohen, T.J., Kiem, A.S., Bostock, H.C., Fitzsimmons, K.E., Jansen, J.D., Kemp, J., Krause, C., Petherick, L., Phipps, S.J., 2013. Climate variability over the last 35,000 years recorded in marine and terrestrial archives in the Australian region: an OZ-INTIMATE compilation. Quat. Sci. Rev. 74, 21–34.
Reeves, J.M., Chivas, A.R., García, A., Holt, S., Couapel, M.J.J., Jones, B.G., Cendón, D.I., Fink, D., 2008. The sedimentary record of palaeoenvironments and sea-level change in the Gulf of Carpentaria, Australia, through the last glacial cycle. Quat. Int. 183, 3–22.
Rasmussen, T.L., Oppo, D.W., Thomsen, E., Lehman, S.J., 2003. Deep sea records from the southeast Labrador Sea: Ocean circulation changes and ice-rafting events during the last 160,000 years. Paleoceanography 18, 1018.
Reimann, T., Thomsen, K.J., Jain, M., Murray, A.S., Frechen, M., 2012. Single-grain dating of young sediments using the pIRIR signal from feldspar. Quat. Geochronol.. 11, 28–41.
Rhodes, E.J., Bronk Ramsey, C., Outram, Z., Batt, C., Willis, L., Dockrill, S., Bond, J., 2003. Bayesian methods applied to the interpretation of multiple OSL dates: high precision sediment ages from Old Scatness Broch excavations, Shetland Isles. Quat. Sci. Rev. 22, 1231–1244.
Shen, Z.X., Mauz, B., Lang, A., 2011. Source-trap characterization of thermally transferred OSL in quartz. J. Phys. D: Appl. Phys. 44, 295405.
Spooner, N.A., 1994. The anomalous fading of infrared-stimulated luminescence from feldspars. Radiat. Meas. 23, 625–632.
Stokes, S., Ingram, S., Aitken, M.J., Sirocko, F., Anderson, R., Leuschner, D., 2003. Alternative chronologies for Late Quaternary (Last Interglacial–Holocene) deep sea sediments via optical dating of silt-sized quartz. Quat. Sci. Rev. 22, 925–941.
Tedford, R.H., Wells, R.T., Barghoorn, S.F., 1992. Tirari Formation and contained fossil faunas, Pliocene of the Lake Eyre Basin, South Australia. Records of the Northern Territory Museum of Arts and Sciences 9, 173–194.
Thiel, C., Buylaert, J.-P., Murray, A., Terhorst, B., Hofer, I., Tsukamoto, S., Frechen, M., 2011. Luminescence dating of the Stratzing loess profile (Austria) – Testing the potential of an elevated temperature post-IR IRSL protocol. Quat. Int. 234, 23–31.
Thomsen, K.J., Murray, A.S., Jain, M., Bøtter-Jensen, L., 2008. Laboratory fading rates of various luminescence signals from feldspar-rich sediment extracts. Radiat. Meas. 43, 1474–1486.
Timar, A., Vandenberghe, D., Panaiotu, E.C., Panaiotu, C.G., Necula, C., Cosma, C., van den haute, P., 2010. Optical dating of Romanian loess using fine-grained quartz. Quat. Geochronol.5, 143–148.
Turney, C.S.M., Kershaw, A.P., Clemens, S.C., Branch, N., Moss, P.T., Keith Fifield, L., 2004. Millennial and orbital variations of El Niño/Southern Oscillation and high-latitude climate in the last glacial period. Nature 428, 306–310.
van der Kaars, S., De Deckker, P., Gingele, F.X., 2006. A 100 000-year record of annual and seasonal rainfall and temperature for northwestern Australia based on a pollen record obtained offshore. J. Quat. Sci. 21, 879–889.
Wang, X.L., Lu, Y.C., Wintle, A.G., 2006. Recuperated OSL dating of fine-grained quartz in Chinese loess. Quat. Geochronol. 1, 89–100.
Wang, X.L., Wintle, A.G., Lu, Y.C., 2007. Testing a single-aliquot protocol for recuperated OSL dating. Radiat. Meas. 42, 380–391.
Wang, Y., Cheng, H., Edwards, R.L., Kong, X., Shao, X., Chen, S., Wu, J., Jiang, X., Wang, X., An, Z., 2008. Millennial- and orbital-scale changes in the East Asian monsoon over the past 224,000 years. Nature 451, 1090–1093.
Wang, Y.J., Cheng, H., Edwards, R.L., An, Z.S., Wu, J.Y., Shen, C.-C., Dorale, J.A., 2001. A High-Resolution Absolute-Dated Late Pleistocene Monsoon Record from Hulu Cave, China. Science 294, 2345–2348.
Wintle, A.G., 1973. Anomalous Fading of Thermo-luminescence in Mineral Samples. Nature 245, 143–144.
Wintle, A.G., Murray, A.S., 2006. A review of quartz optically stimulated luminescence characteristics and their relevance in single-aliquot regeneration dating protocols. Radiat. Meas. 41, 369–391.
Wyrwoll, K.-H., Liu, Z., Chen, G., Kutzbach, J.E., Liu, X., 2007. Sensitivity of the Australian summer monsoon to tilt and precession forcing. Quat. Sci. Rev. 26, 3043–3057.
Wyrwoll, K.-H., Valdes, P., 2003. Insolation forcing of the Australian monsoon as controls of Pleistocene mega-lake events. Geophys. Res. Lett. 30, 2279.

Yoshida, H., Roberts, R.G., Olley, J.M., Laslett, G.M., Galbraith, R.F., 2000. Extending the age range of optical dating using single “supergrains” of quartz. Radiat. Meas. 32, 439–446.
Zander, A., Hilgers, A., 2013. Potential and limits of OSL, TT-OSL, IRSL and pIRIR290 dating methods applied on a Middle Pleistocene sediment record of Lake El’gygytgyn, Russia. Clim. Past 9, 719–733.
Zheng, H., Powell, C.M., Zhao, H., 2003. Eolian and lacustrine evidence of late Quaternary palaeoenvironmental changes in southwestern Australia. Glob. Planet. Change 35, 75–92.

## Figure Caption

Fig.1. (a) Map showing the overview of the Lake Eyre Basin (LEB). Lake Eyre is located at the lowest point of the LEB. (b) Map showing that Lake Eyre can be divided into Lake Eyre North and Lake Eyre South. The highlighted square indicates the location of the Madigan Gulf.

Fig.2. (a) An aerial image of Madigan Gulf showing the location of Williams Point in Lake Eyre North. Black filled circles represent locations and names of cores from Magee et al., (1995). White circle shows location of cores LEWP1 and LEWP2. (b) Stratigraphic interpretation of Williams Point sequence, which can be broadly divided into three main sedimentary phases (see section 2.2). The circle shows the position of sample LE14-1.

Fig.3. A schematic sedimentary log of LEWP1 core and core photo. The black circles indicate the positions of the luminescence dating samples. The blue circle indicates the position of sample LEWP 1.96, which was collected only for dose rate evaluation. The yellow circle indicates the position of the modern sample LE-M, which is used for residual dose evaluation for the LEWP1 core samples. Note that a core disturbance layer (the white blank in the schematic profile) has been avoided during core logging and OSL sampling.

Fig.4. Summary of dosimetry information for the LEWP1 core samples. w.c. means water content. The circles and diamonds in (h) are final dose rates of quartz and K-feldspar, respectively. U, Th and K contents in (a)–(c) are based on ICP-MS/OES measurements.

Fig.5. Dose recovery results and representative $D_e$ distribution for single-aliquot quartz OSL dating. (a) Recovered to given dose ratios of 20 aliquots for sample LEWP 0.50, shown as a radial plot. See experimental details in SI. The grey shaded region is centred on a recovered to given dose ratio of 1. (b) $D_e$ values of 25 aliquots for sample LEWP 0.50, shown as a radial plot. The grey band is centred on the weighted mean $D_e$ value derived using the CAM.

Fig.6. Dose recovery results (recovered to given dose ratios) (a), g-values (b) and residual doses (c) for different IRSL and pIRIR signals in single-aliquot K-feldspar MET-pIRIR dating. Dose recovery test was measured on 5 discs of sample LEWP 3.63 (see SI for details).

Residual doses were measured using a modern sample LE-M (Fig.3). g-values (normalised to 2-days) were measured using three samples: LEWP 0.50 (triangles), LEWP 1.21 (circles) and LEWP 3.63 (diamonds).

Fig.7. (a) $pIRIR_{250}$ $D_e$ value distribution of 12 aliquots from sample LEWP 0.89, shown as a radial plot. The grey band is centred on the weighted mean $D_e$ value derived using the CAM. The measured grain size for this sample is 90-180 μm, and 1 mm aliquots were used for $D_e$ determination. (b) $D_e$ values of different IRSL and pIRIR signals for sample LEWP 0.89 plotted against IR stimulation temperatures. (c) $D_e$ values of different IRSL and pIRIR signals for sample LEWP 2.15 plotted against IR stimulation temperatures. The measured grain size for this sample is 45-63 μm, and 4 mm aliquots were used for $D_e$ determination.

Fig.8. Radial plots showing the single-grain OSL and TT-OSL $D_e$ results. (a) Recovered to given dose ratios obtained for a dose recovery test performed on individual quartz grains of LE14-1 (see SI for details). The grey shaded region on the radial plot is centred on the administered dose for each grain (recovered to given dose ratio of 1). (b) Dose-recovery test (natural + dosed) $D_e$ values obtained for individual quartz grains of LE14-1 (see SI for details). (c) Single-grain OSL natural $D_e$ distribution for LE14-1. (d) Single-grain TT-OSL natural $D_e$ distribution for LE14-1.The grey bands in b-d are centred on the weighted mean $D_e$ values derived using the CAM.

Fig.9. The final single-aliquot quartz OSL, TT-OSL and K-feldspar pIRIR ages plotted against sample depth for the LEWP1 core. The dashed lines indicate the boundaries of different sedimentary units (see Fig. 3 and Table 1). The block indicates three samples that exhibit potentially complicated dosimetry results which are excluded from final chronological discussions in this study (see discussions in section 4.3).

Fig.10. Bayesian age-depth modelling results for the Lake Eyre Williams Point sequence obtained using a non-continuous deposition modelling scenario (Model 2, see section 5.2). The likelihoods are based on the pIRIR dating results of eight core samples from LEWP1 (excluding three samples that exhibit potentially complicated dosimetry results) and the combined (weighted mean) single-grain OSL and TT-OSL ages of sample LE14-1 from the base of the Williams Point outcrop. The right-hand column shows the boundaries of different

sedimentary units (see Fig. 3 and Table 1). The prior age distributions for the dating samples (likelihoods) are shown in light blue. The modelled posterior distributions for the dating sample and unit boundaries are shown in dark blue and grey, respectively. Likelihood and posterior ages are shown on a calendar year timescale and are both expressed in years before sample collection (AD2014). The white circles and associated error bars represent the mean ages and $1\sigma$ uncertainty ranges of the PDFs. The 68.2% and 95.4% ranges of the posterior probabilities are indicated by the horizontal bars underneath the PDFs.

Fig.11. Schematic diagrams showing the palaeo-hydrological history of Lake Eyre since MIS 7, as recorded by the Williams Point sequence and palaeo-shoreline records. See detailed description in section 5.4.

Fig.12. Comparison of the combined Williams Point chronostratigraphic sequence record with other published climatic records. (a) Chronology of different sedimentary stages of Lake Eyre recorded at the Williams Point sequence. The ages >100 ka are based on the Bayesian modelled results from this study, and the ages <100 ka are based on TL/AAR ages of Magee et al. (1995). Note that the y-axis only represents a relative relationship between the depths of different phases. (b) Palaeoshoreline elevations and pooled ages of Lake Eyre cited from Cohen et al. (2015). The shoreline ages are based on single-grain quartz OSL dating; (c) January solar insolation at 15 °S (Berger, 1992); (d) the Antarctic temperature anomaly recovered from the Dome C ice core (Jouzel et al., 2007); (e) Stalagmite $\delta^{18}O$ records from Sanbao Cave (dark green, Wang et al., 2008; light green, Cheng et al., 2009) and Hulu Cave (pink, Wang et al., 2001) in central south China, which indicates the strength of the East Asia summer monsoon (EASM). The blue hatches indicate Heinrich events (Rasmussen et al., 2003), the orange hatches indicate the ice rafted debris (IRD) layers registered in North Atlantic marine sediment cores (Chapman and Shackleton, 1999). The grey bars indicate wet episodes of Lake Eyre characterised by deep-water lacustrine regime or high palaeoshorelines. Marine Isotope Stages after Martinson et al. (1987).

Table 1 Stratigraphic log of the LEWP1 core

| Unit | Sub-unit | Depth in the core (m) | AHD Depth (m) | Descriptions | Depositional environment |
|---|---|---|---|---|---|
| B (modern playa) | - | 0-0.13 | -13.43 to -13.56 | Light brown medium-coarse sand, no lamination | playa environment |
| C (muddy playa) | - | 0.13-0.57 | -13.56 to -14.00 | Poorly laminated red brown clay. Mottled with iron and manganese, gypsum layers up to 5 mm thick at 0.54 and 0.57 m. | playa environment |
| D (deep-water lacustrine) | D1 | 0.57-0.80 | -14.00 to -14.23 | Grey clay with some brown mottles. No visible lamination. Several gypsum horizons up to 4 cm thick (thickest occurring at 0.77-0.81 m). | deep-water lacustrine, with occasional dry conditions |
| | D2 | 0.80-2.47 | -14.23 to -15.90 | Dark-grey to grey clay (with the darkest colour observed at 1.51-1.58 m), sub mm lamination. Thin gypsum horizons appear occasionally. A thick gypsum layer appears at 1.66-1.68 m. | deep-water lacustrine |
| | D3 | 2.47-3.27 | -15.90 to -16.70 | Distinct brown clay and grey clay sub mm laminations. Gypsum horizons appear frequently. Between 3.00 m and 3.12 m is a core disturbance layer. | deep-water lacustrine with oscillating water depth |
| E (transgressive sediments) | - | 3.27-4.00 | -16.70 to -17.43 | Homogeneous grey clayey sand, no visible lamination. Only gypsum horizon appears at 3.72 m. | Shallow-water lacustrine |

Table 2 A summary of sample depth, measured chronometers, measurement procedures, radioactive element contents, moisture contents, $D_e$ values, dose rates and luminescence ages for all dating samples.

| Sample [a] | Depth below surface (m) | AHD Depth (m) | Mineral | Grain size (μm) | Method | Aliquot size [b] | U (ppm) [c] | Th (ppm) [c] | K (%) [c] | Moisture content (%) [d] | Dose rate (Gy/ka) [e] | $D_e$ (Gy) | Number of discs/grains | Age (ka) |
|---|---|---|---|---|---|---|---|---|---|---|---|---|---|---|
| **LE14-1** | 0.70 | -10.74 | Quartz | 212-250 | OSL | SG | 2.83±0.19 | 1.68±0.11 | 0.59±0.03 | 60 | 1.38±0.08 | 173.99±7.57 | 88 | 126.43±9.74 |
| | | | Quartz | 212-250 | TT-OSL | SG | | | | | 1.38±0.08 | 194.22±11.87 | 67 | 141.13±12.44 |
| **LEWP 0.50** | 0.50 | -13.93 | Quartz | 45-63 | OSL | MA | 1.83±0.09 | 4.60±0.23 | 1.03±0.06 | 47 | 1.49±0.10 | 194.59±13.33 | 25 | 130.39±12.27 |
| | | | Quartz | 45-63 | TT-OSL | MA | | | | | 1.49±0.10 | 198.06±17.43 | 5 | 132.71±14.48 |
| | | | K-feldspar | 45-63 | pIRIR | MA | | | | | 1.85±0.12 | 273.87±13.93 | 14 | 147.68±12.04 |
| **LEWP 0.89** | 0.89 | -14.32 | Quartz | 45-63 | OSL | MA | 3.48±0.17 | 4.57±0.23 | 1.04±0.05 | 36 | 1.84±0.11 | 323.36±23.00 | 19 | 175.39±16.36 |
| | | | Quartz | 45-63 | TT-OSL | MA | | | | | 1.84±0.11 | 399.64±23.07 | 7 | 216.76±18.10 |
| | | | K-feldspar | 90-180 | pIRIR | SA | | | | | 2.44±0.21 | 469.99±25.15 | 12 | 192.41±19.55 |
| **LEWP 1.21** | 1.21 | -14.64 | K-feldspar | 63-90 | pIRIR | SA | 2.82±0.14 | 6.49±0.32 | 1.22±0.06 | 49 | 2.26±0.15 | 460.12±22.13 | 13 | 203.35±16.55 |
| **LEWP 1.40** | 1.40 | -14.83 | Quartz | 45-63 | OSL | MA | 4.78±0.24 | 6.50±0.33 | 1.20±0.06 | 48 | 2.26±0.15 | 323.62±22.42 | 25 | 143.17±13.81 |
| | | | K-feldspar | 45-63 | pIRIR | MA | | | | | 2.72±0.20 | 456.31±31.18 | 16 | 167.92±16.80 |
| **LEWP 1.58** | 1.58 | -15.01 | Quartz | 45-63 | TT-OSL | MA | 19.98±1.00 | 6.36±0.32 | 1.23±0.06 | 50 | 4.40±0.33 | 448.50±37.10 | 5 | 101.89±11.35 |
| | | | K-feldspar | 45-63 | pIRIR | MA | | | | | 5.25±0.56 | 630.56±30.64 | 10 | 120.09±14.13 |
| **LEWP 1.77** | 1.77 | -15.20 | K-feldspar | 90-180 | pIRIR | SA | 8.93±0.45 | 6.42±0.32 | 1.19±0.06 | 50 | 3.41±0.28 | 500.10±29.62 | 9 | 146.49±14.80 |
| **LEWP 1.96** | 1.96 | -15.39 | - | - | - | - | 3.95±0.20 | 6.50±0.33 | 1.19±0.06 | 50 | - | - | - | - |
| **LEWP 2.15** | 2.15 | -15.58 | Quartz | 45-63 | TT-OSL | MA | 4.47±0.22 | 5.68±0.28 | 1.05±0.05 | 53 | 1.88±0.12 | 314.29±26.15 | 5 | 167.62±17.70 |
| | | | K-feldspar | 45-63 | pIRIR | MA | | | | | 2.31±0.17 | 420.93±19.88 | 9 | 182.30±15.83 |
| **LEWP 2.35** | 2.35 | -15.78 | K-feldspar | 90-180 | pIRIR | SA | 3.46±0.17 | 6.60±0.33 | 1.21±0.06 | 49 | 2.49±0.21 | 501.48±24.26 | 12 | 201.15±19.89 |
| **LEWP 2.73** | 2.73 | -16.16 | Quartz | 45-63 | TT-OSL | MA | 5.65±0.28 | 6.01±0.30 | 1.06±0.05 | 48 | 2.15±0.14 | 365.36±17.97 | 5 | 169.86±13.59 |
| | | | K-feldspar | 45-63 | pIRIR | MA | | | | | 2.63±0.20 | 479.29±25.42 | 12 | 182.58±16.82 |
| **LEWP 3.63** | 3.63 | -17.06 | Quartz | 45-63 | OSL | MA | 2.29±0.11 | 2.21±0.11 | 0.43±0.02 | 36 | 1.05±0.06 | 202.53±12.42 | 15 | 193.56±16.31 |
| | | | K-feldspar | 45-63 | pIRIR | MA | | | | | 1.41±0.10 | 246.23±10.11 | 16 | 174.71±17.95 |
| **LEWP 3.82** | 3.82 | -17.25 | Quartz | 45-63 | TT-OSL | MA | 3.20±0.16 | 2.83±0.14 | 0.59±0.03 | 37 | 1.32±0.08 | 249.00±27.35 | 5 | 188.18±23.70 |
| | | | K-feldspar | 63-90 | pIRIR | SA | | | | | 1.75±0.12 | 391.83±16.92 | 12 | 223.49±17.71 |

[a] Sample LEWP 1.96 was collected only for gamma dose rate correction for adjacent samples, therefore no $D_e$ value was measured for this sample.

[b] SG—single grain; MA—medium-sized single-aliquot (4 mm in diameter); SA—small-sized single-aliquot (1 mm in diameter).

[c] The U, Th and K contents of the LEWP1 core samples were measured using ICP-MS and ICP-OES. The U, Th and K contents of sampleLE14-1 are based on *in situ* gamma spectrometry results, and have been calculated using the 'windows approach' outlined in Arnold et al. (2012b). The total dose rate of this sample has been calculated using a combination of *in situ* gamma spectrometry (to calculate the gamma dose rate), and low-level beta counting (to calculate the beta dose rate).

[d] The relative uncertainty for moisture content is set to be 25%.

[e] Details of dose rate calculation are given in Table S1.

Table 3 Summary of Bayesian modelling results obtained using a non-continuous deposition modelling scenario (Model 2). The likelihood (unmodelled) and posterior (modelled) age ranges are presented for each of the numerical dating samples. Posterior (modelled) age ranges are also shown for the boundaries of each stratigraphic unit. Posterior ages are presented as the 68.2% and 95.4% highest probability density ranges. The mean and 1σ uncertainty ranges of the modelled posterior distributions are shown for comparison (assuming a normally distributed probability density function). The unmodelled and modelled age estimates have been rounded to the nearest 50 years.

| Boundary | Dating sample | Depth (cm AHD) | Unmodelled age (years before AD2014) | | | Modelled age (years before AD2014) | | | Agreement index ($A_i$) (%) | Posterior outlier probability (%) |
|---|---|---|---|---|---|---|---|---|---|---|
| | | | 68.2% range | 95.4% range | Mean ± 1σ | 68.2% range | 95.4% range | Mean ± 1σ | | |
| Unit A top | | -985 | | | | 107450 – 136050 | 71100 – 140150 | 113050 ± 19750 | | |
| | LE14-1 (SG OSL+SG TT-OSL) | -1074 | 122300 – 140800 | 113450 – 149700 | 131550 ± 9050 | 111850 – 138050 | 77600 – 142500 | 117500 ± 17200 | 75.1 | 24 |
| Unit A bottom | | -1356 | | | | 120150 – 148050 | 91550 – 158600 | 129900 ± 16350 | | |
| Unit C top | | -1356 | | | | 132050 – 158300 | 112900 – 169650 | 142750 ± 14500 | | |
| | LEWP 0.5 (pIRIR) | -1393 | 135400 – 159950 | 123600 – 171750 | 147700 ± 12050 | 145600 – 166050 | 134850 – 175700 | 155250 ± 10300 | 99.2 | 1 |
| Unit C bottom | | -1400 | | | | 146900 – 169150 | 136900 – 179100 | 157800 ± 10900 | | |
| Unit D top | | -1400 | | | | 172650 – 191000 | 162900 – 198050 | 180750 ± 8950 | | |
| | LEWP 0.89 (pIRIR) | -1432 | 172450 – 212350 | 153300 – 231500 | 192400 ± 19550 | 173950 – 190950 | 164750 – 198800 | 182000 ± 8400 | 117.5 | 4 |
| | LEWP 1.21 (pIRIR) | -1464 | 186450 – 220250 | 170250 – 236450 | 203350 ± 16550 | 175350 – 191600 | 167250 – 199050 | 183250 ± 7950 | 69.7 | 9 |
| | LEWP 2.15 (pIRIR) | -1558 | 166150 – 198450 | 150650 – 213950 | 182300 ± 15850 | 179250 – 194600 | 171350 – 201900 | 186800 ± 7500 | 128.4 | 1 |
| | LEWP 2.35 (pIRIR) | -1578 | 180850 – 221450 | 161350 – 240950 | 201150 ± 19900 | 179750 – 195650 | 172200 – 202850 | 187550 ± 7600 | 109.1 | 5 |
| | LEWP 2.73 (pIRIR) | -1616 | 165400 – 199750 | 148950 – 216200 | 182600 ± 16800 | 181400 – 196850 | 173000 – 204950 | 189000 ± 7900 | 125.4 | 1 |
| Unit D bottom | | -1670 | | | | 181550 – 199450 | 174900 – 208150 | 191050 ± 8600 | | |
| Unit E top | | -1670 | | | | 188300 – 210150 | 180500 – 220800 | 200550 ± 10300 | | |
| | LEWP 3.63 (pIRIR) | -1706 | 156400 – 193000 | 138800 – 210600 | 174700 ± 17950 | 199100 – 219000 | 190100 – 229750 | 209550 ± 9800 | 30.5 | 0 |
| | LEWP 3.82 (pIRIR) | -1725 | 205450 – 241550 | 188050 – 258900 | 223500 ± 17700 | 201850 – 226300 | 192250 – 239750 | 215150 ± 11950 | 110.0 | 4 |
| Unit E bottom | | -1743 | | | | 203000 – 232550 | 193300 – 252900 | 221300 ± 18800 | | |

Fig. 1.

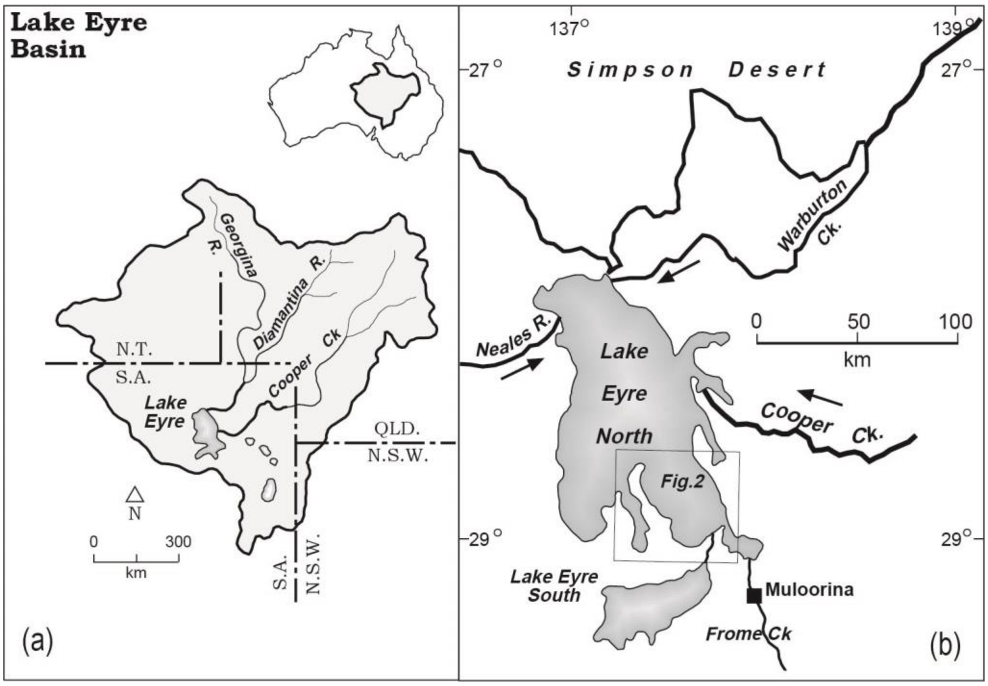
Lake Eyre Basin
Georgina R.
Diamantina R.
Cooper Ck
N.T.
S.A.
Lake Eyre
QLD.
N.S.W.
N
0
300
km
S.A.
N.S.W.
(a)
137°
139°
27°
27°
Simpson Desert
Warburton Ck.
Neales R.
Lake Eyre North
0
50
100
km
Cooper Ck.
Fig.2
29°
29°
Lake Eyre South
Muloorina
Frome Ck
(b)

Fig.2.

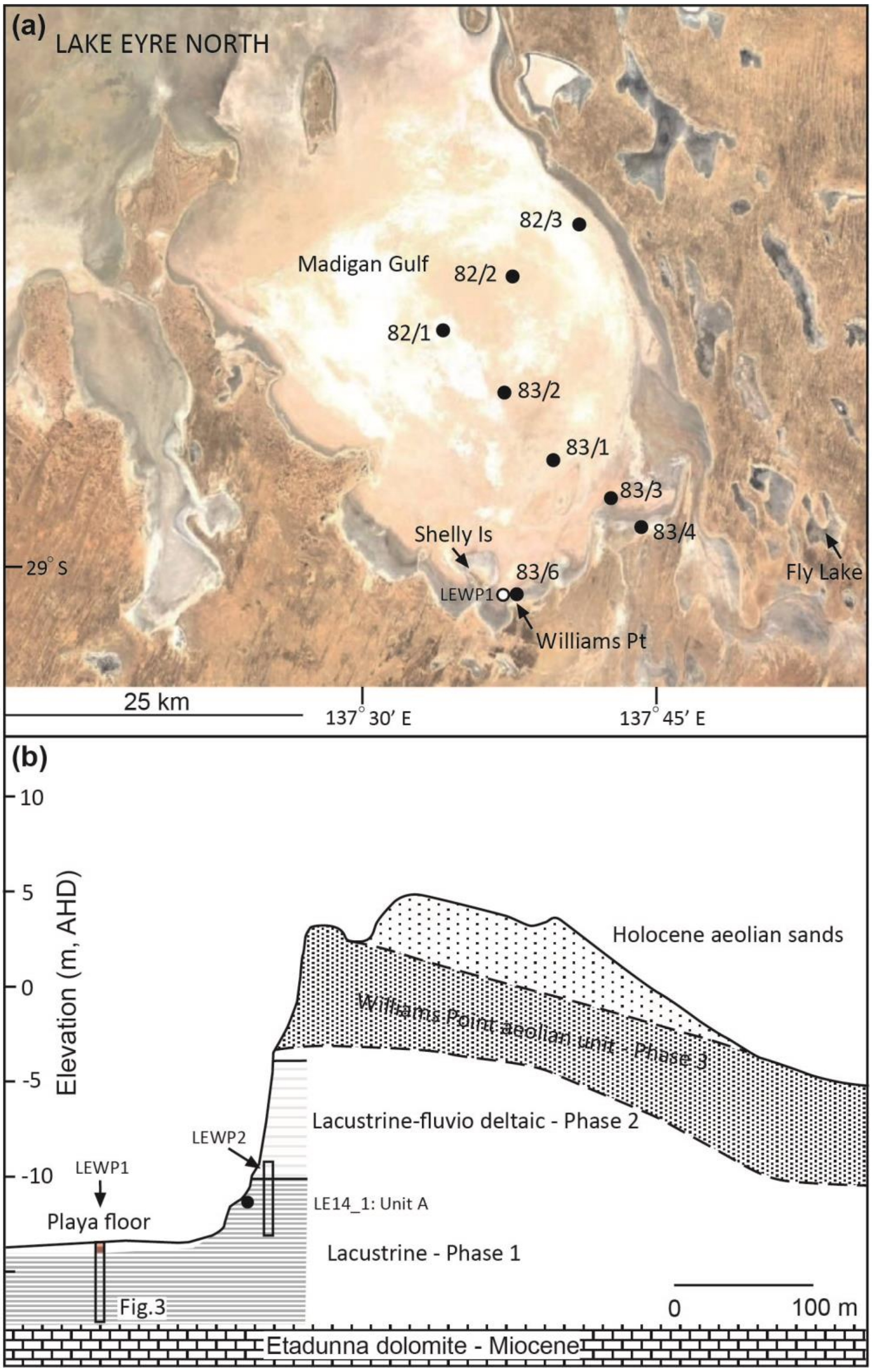
(a) LAKE EYRE NORTH
82/3
Madigan Gulf
82/2
82/1
83/2
83/1
83/3
83/4
Shelly Is
29° S
83/6
LEWP1
Williams Pt
Fly Lake
25 km
137° 30′ E
137° 45′ E
(b)
Elevation (m, AHD)
10
5
0
-5
-10
Holocene aeolian sands
Williams Point aeolian unit - Phase 3
Lacustrine-fluvio deltaic - Phase 2
LEWP2
LEWP1
Playa floor
LE14_1: Unit A
Lacustrine - Phase 1
Fig.3
0
100 m
Etadunna dolomite - Miocene

Fig.3.

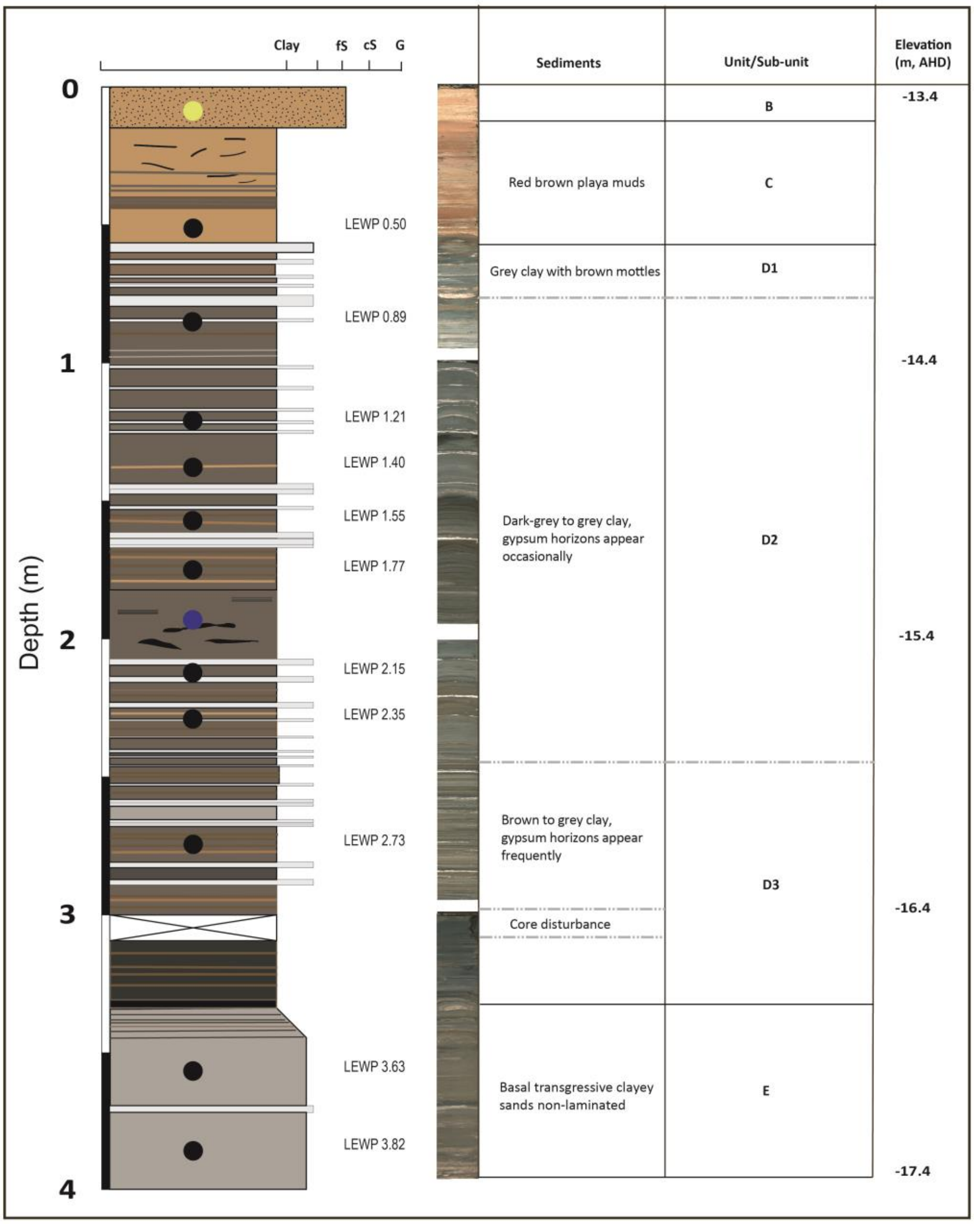
Clay
fS
cS
G
Depth (m)
0
1
2
3
4
LEWP 0.50
LEWP 0.89
LEWP 1.21
LEWP 1.40
LEWP 1.55
LEWP 1.77
LEWP 2.15
LEWP 2.35
LEWP 2.73
LEWP 3.63
LEWP 3.82
Sediments
Unit/Sub-unit
Elevation (m, AHD)
B
-13.4
Red brown playa muds
C
Grey clay with brown mottles
D1
-14.4
Dark-grey to grey clay, gypsum horizons appear occasionally
D2
-15.4
Brown to grey clay, gypsum horizons appear frequently
D3
Core disturbance
-16.4
Basal transgressive clayey sands non-laminated
E
-17.4

Fig. 4

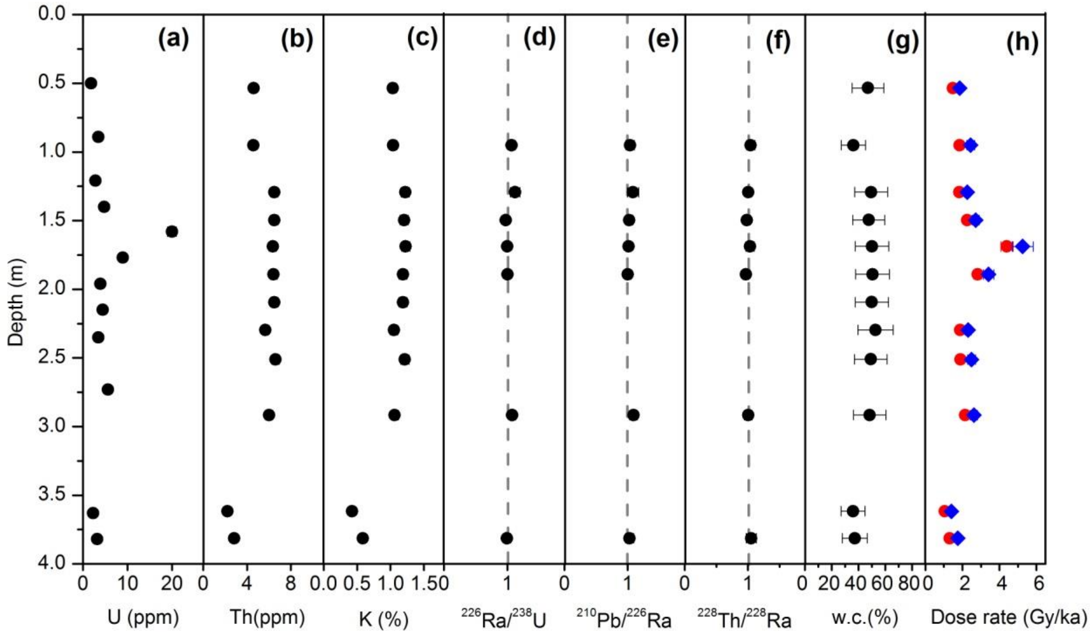

(a)
(b)
(c)
(d)
(e)
(f)
(g)
(h)
Depth (m)
U (ppm)
Th(ppm)
K (%)
$^{226}Ra/^{238}U$
$^{210}Pb/^{226}Ra$
$^{228}Th/^{228}Ra$
w.c.(%)
Dose rate (Gy/ka)

Fig.5.

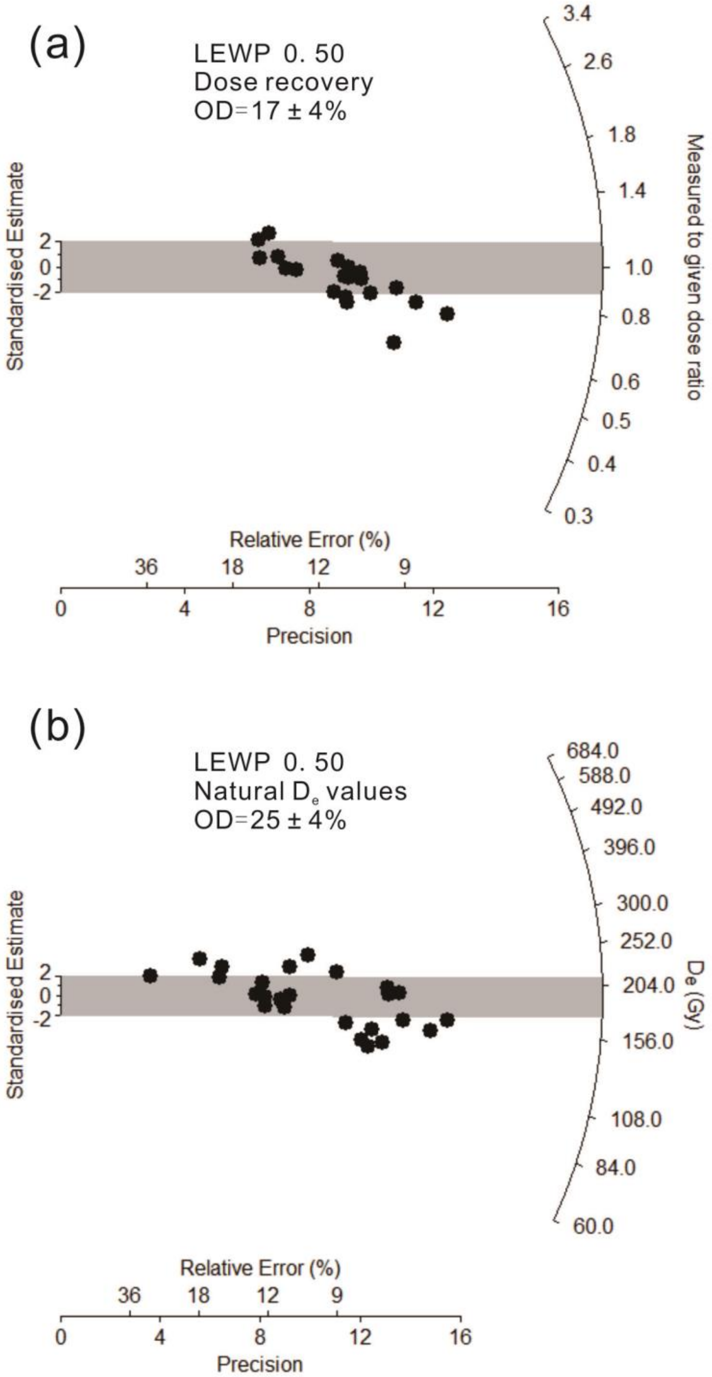
(a)
LEWP 0. 50
Dose recovery
OD=17 ± 4%
Standardised Estimate
2
0
-2
Measured to given dose ratio
3.4
2.6
1.8
1.4
1.0
0.8
0.6
0.5
0.4
0.3
Relative Error (%)
36
18
12
9
0
4
8
12
16
Precision
(b)
LEWP 0. 50
Natural $D_e$ values
OD=25 ± 4%
Standardised Estimate
2
0
-2
$D_e$ (Gy)
684.0
588.0
492.0
396.0
300.0
252.0
204.0
156.0
108.0
84.0
60.0
Relative Error (%)
36
18
12
9
0
4
8
12
16
Precision

Fig. 6.

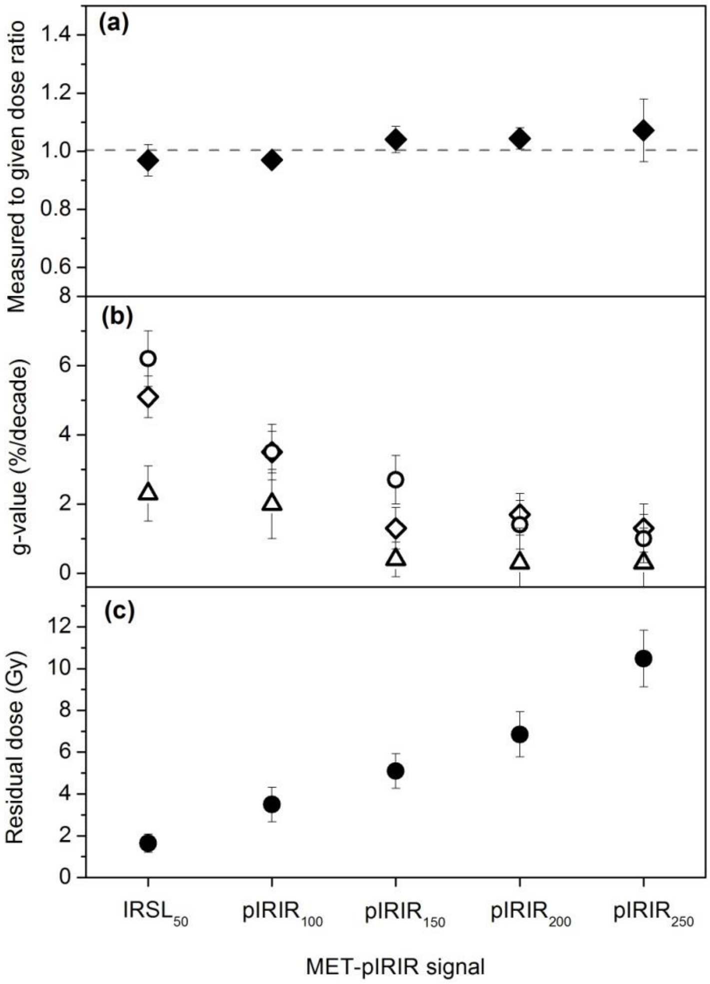

(a)
Measured to given dose ratio
1.4
1.2
1.0
0.8
0.6
(b)
g-value (%/decade)
8
6
4
2
0
(c)
Residual dose (Gy)
12
10
8
6
4
2
0
IRSL50
pIRIR100
pIRIR150
pIRIR200
pIRIR250
MET-pIRIR signal

Fig.7.

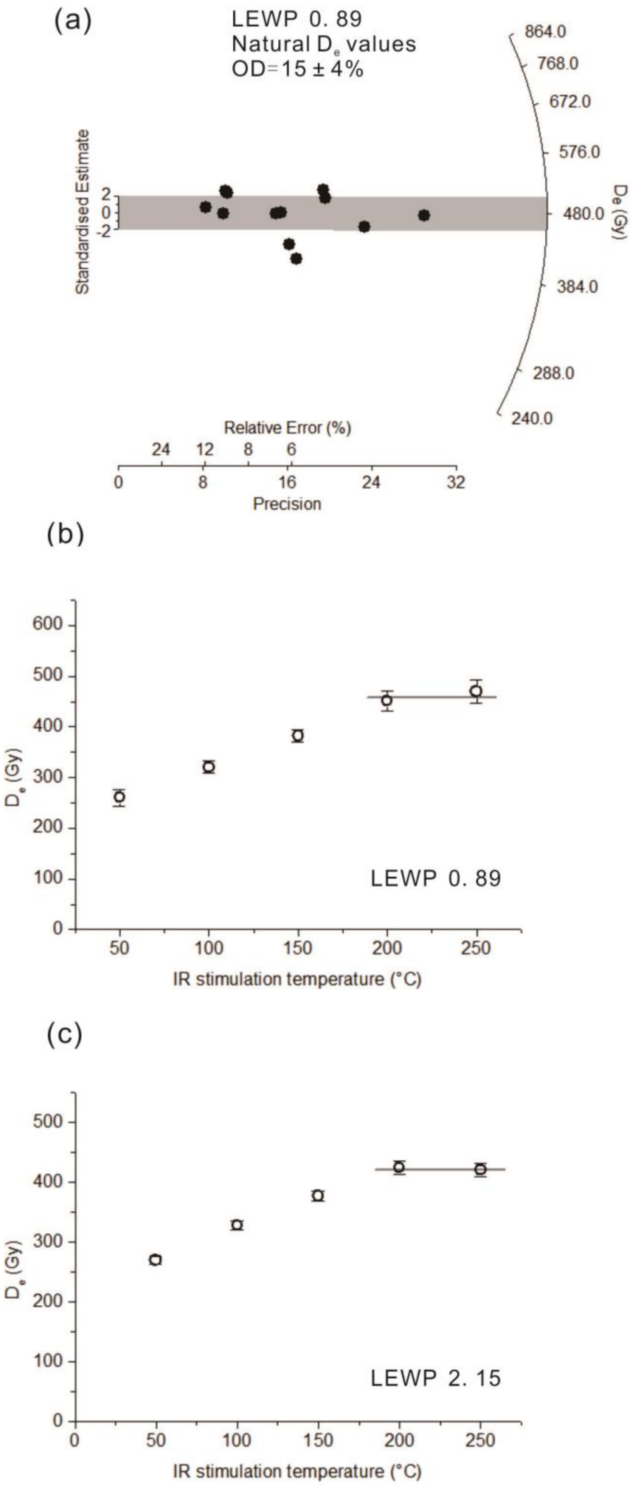
(a)
LEWP 0. 89
Natural $D_e$ values
OD=15 ± 4%
Standardised Estimate
2
0
-2
864.0
768.0
672.0
576.0
480.0
384.0
288.0
240.0
$D_e$ (Gy)
Relative Error (%)
24 12 8 6
0 8 16 24 32
Precision
(b)
$D_e$ (Gy)
600
500
400
300
200
100
0
LEWP 0. 89
50 100 150 200 250
IR stimulation temperature (°C)
(c)
$D_e$ (Gy)
500
400
300
200
100
0
LEWP 2. 15
0 50 100 150 200 250
IR stimulation temperature (°C)

Fig.8.

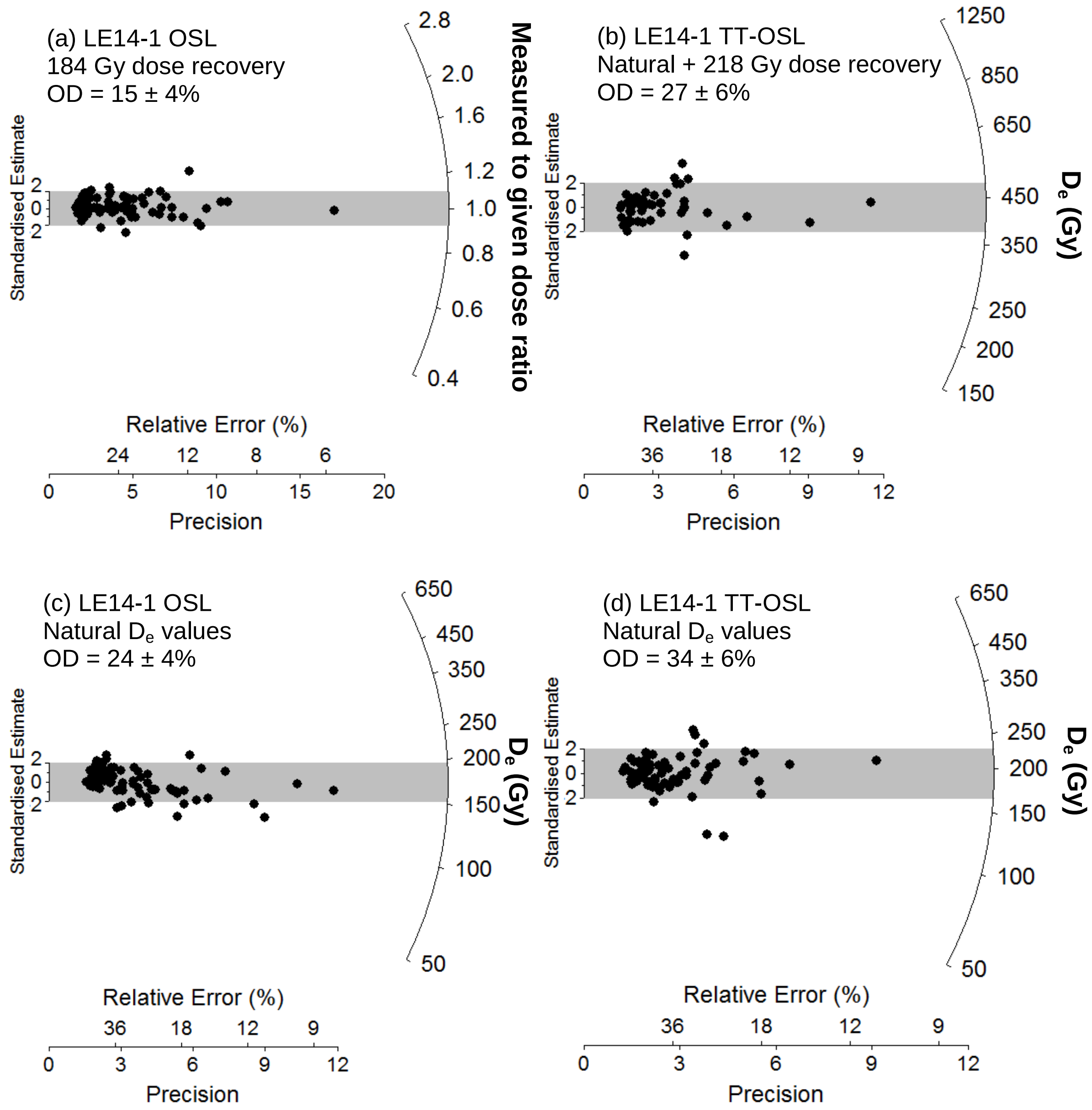

(a) LE14-1 OSL
184 Gy dose recovery
OD = 15 ± 4%
Standardised Estimate
2
0
2
2.8
2.0
1.6
1.2
1.0
0.8
0.6
0.4
Measured to given dose ratio
Relative Error (%)
24
12
8
6
0
5
10
15
20
Precision
(b) LE14-1 TT-OSL
Natural + 218 Gy dose recovery
OD = 27 ± 6%
Standardised Estimate
1250
850
650
450
350
250
200
150
De (Gy)
Relative Error (%)
36
18
12
9
0
3
6
9
12
Precision
(c) LE14-1 OSL
Natural De values
OD = 24 ± 4%
Standardised Estimate
650
450
350
250
200
150
100
50
De (Gy)
Relative Error (%)
36
18
12
9
0
3
6
9
12
Precision
(d) LE14-1 TT-OSL
Natural De values
OD = 34 ± 6%
Standardised Estimate
650
450
350
250
200
150
100
50
De (Gy)
Relative Error (%)
36
18
12
9
0
3
6
9
12
Precision

Fig. 9.

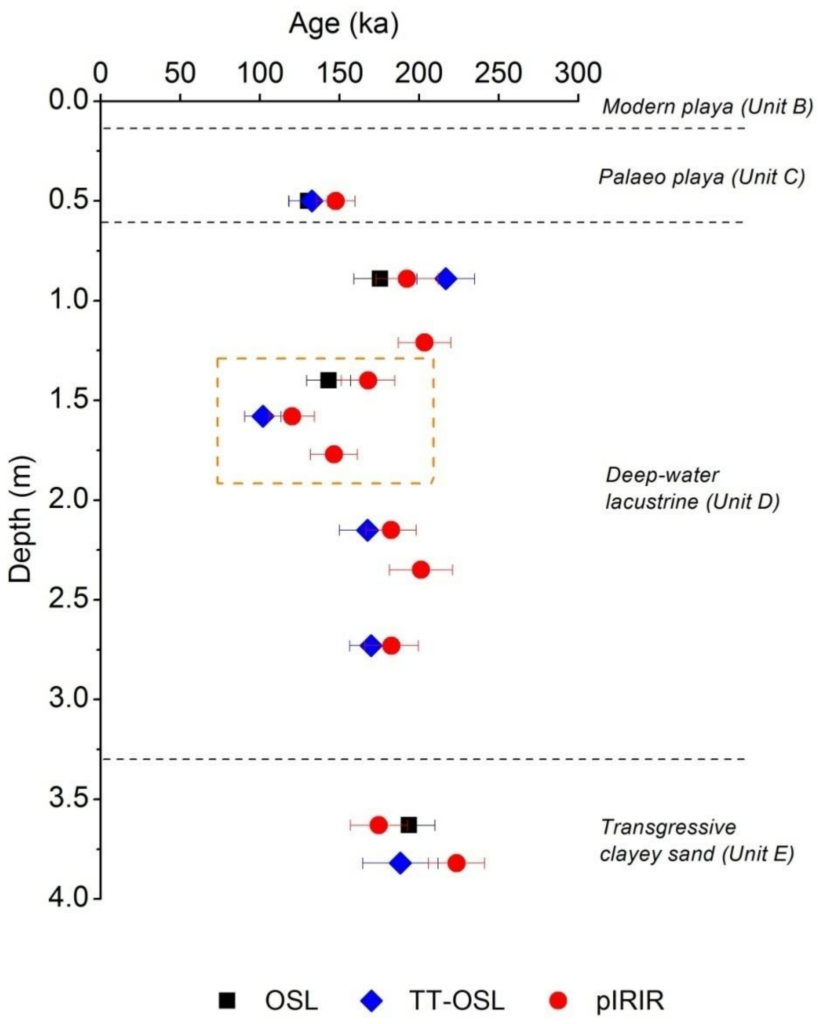

Age (ka)
0
50
100
150
200
250
300
0.0
0.5
1.0
1.5
2.0
2.5
3.0
3.5
4.0
Depth (m)
Modern playa (Unit B)
Palaeo playa (Unit C)
Deep-water
lacustrine (Unit D)
Transgressive
clayey sand (Unit E)
OSL
TT-OSL
pIRIR

Fig.10.

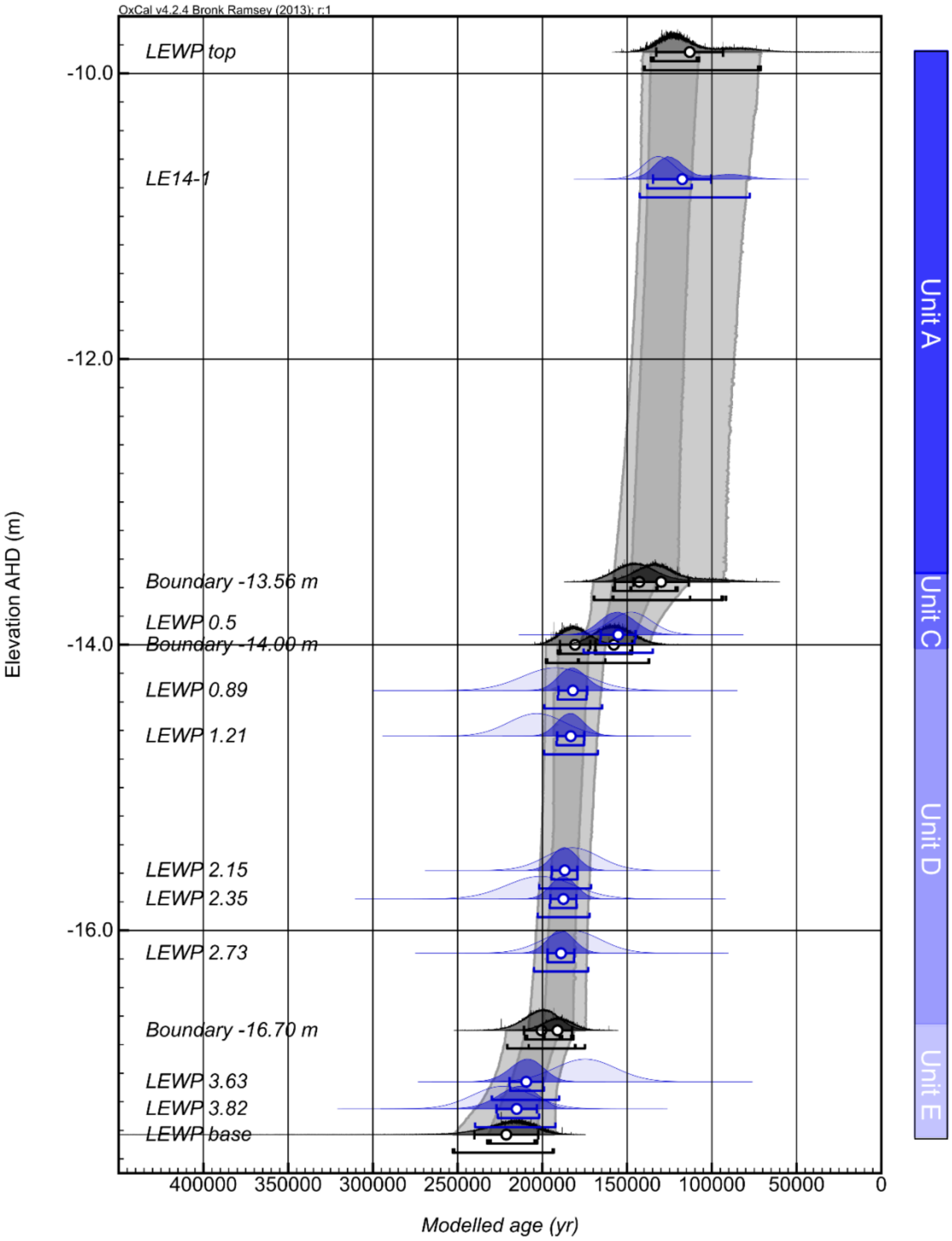
OxCal v4.2.4 Bronk Ramsey (2013); r:1
LEWP top
LE14-1
Boundary -13.56 m
LEWP 0.5
Boundary -14.00 m
LEWP 0.89
LEWP 1.21
LEWP 2.15
LEWP 2.35
LEWP 2.73
Boundary -16.70 m
LEWP 3.63
LEWP 3.82
LEWP base
-10.0
-12.0
-14.0
-16.0
Elevation AHD (m)
400000 350000 300000 250000 200000 150000 100000 50000 0
Modelled age (yr)
Unit A
Unit C
Unit D
Unit E

Fig. 11.

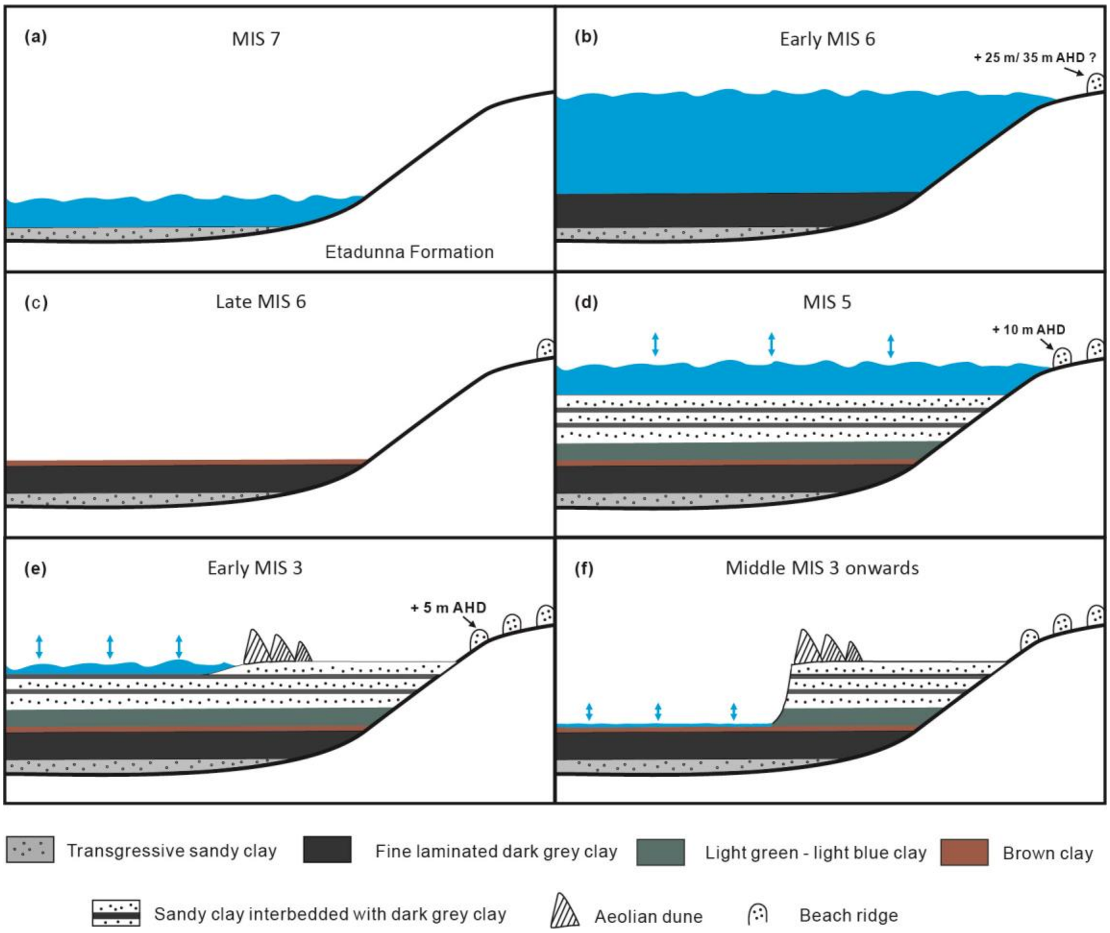
(a)
MIS 7
Etadunna Formation
(b)
Early MIS 6
+ 25 m/ 35 m AHD ?
(c)
Late MIS 6
(d)
MIS 5
+ 10 m AHD
(e)
Early MIS 3
+ 5 m AHD
(f)
Middle MIS 3 onwards
Transgressive sandy clay
Fine laminated dark grey clay
Light green - light blue clay
Brown clay
Sandy clay interbedded with dark grey clay
Aeolian dune
Beach ridge

Fig. 12.

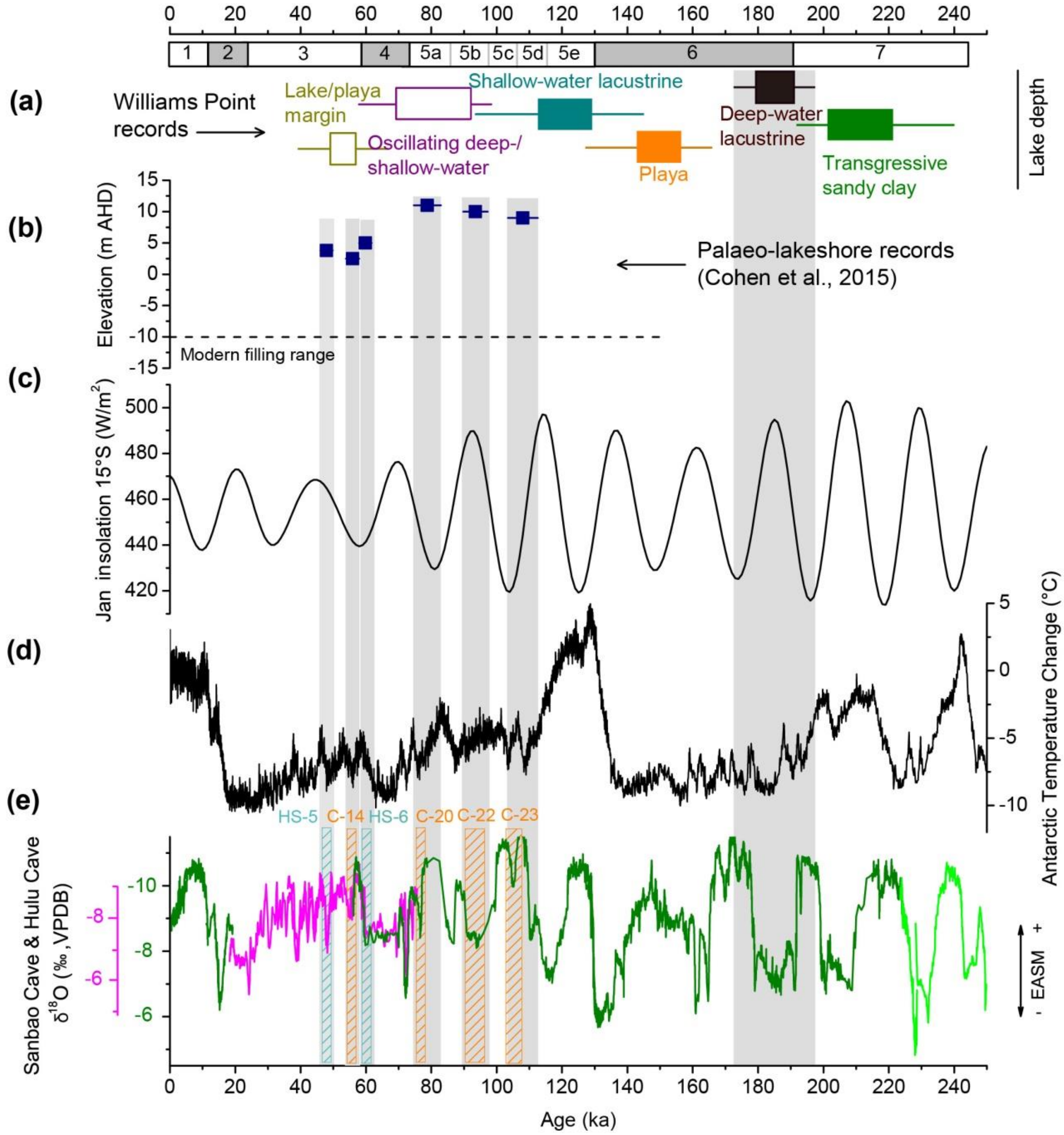

1
2
3
4
5a
5b
5c
5d
5e
6
7
(a)
Williams Point records
Lake/playa margin
Shallow-water lacustrine
Oscillating deep-/ shallow-water
Deep-water lacustrine
Playa
Transgressive sandy clay
Lake depth
(b)
Elevation (m AHD)
Palaeo-lakeshore records (Cohen et al., 2015)
Modern filling range
(c)
Jan insolation 15°S (W/m²)
(d)
Antarctic Temperature Change (°C)
(e)
HS-5
C-14
HS-6
C-20
C-22
C-23
Sanbao Cave & Hulu Cave δ¹⁸O (‰, VPDB)
EASM
Age (ka)

# Supplementary Information to “Extending the record of lacustrine phases beyond the last interglacial for Lake Eyre in central Australia using luminescence dating”

Xiao Fu [a], Tim J. Cohen [a, b], Lee J. Arnold [c]

[a] *GeoQuEST Research Centre, School of Earth and Environmental Sciences, University of Wollongong, Wollongong, NSW 2522, Australia*

[b] *ARC Centre of Excellence for Australian Biodiversity and Heritage, University of Wollongong, Wollongong, NSW 2522, Australia*

[c] *School of Physical Sciences, Environment Institute, and Institute for Photonics and Advanced Sensing (IPAS), University of Adelaide, North Terrace Campus, Adelaide, SA, 5005, Australia*

## S1. Information on facilities and methods

### S1.1. Sample preparation

11 LEWP1 core samples were prepared using standard separation methods (Aitken, 1998). The raw samples were first treated with 10% HCl and 30% $H_2O_2$ to remove carbonate and organics. For single-aliquot dating of the LEWP1 samples, coarse grains (63-90, 90-180 μm) and medium grains (45-63 μm) were separated by wet sieving, but the former was only successfully recovered from a few samples. Given the limitations of grain size availability, we mainly used medium grain size quartz and K-feldspar. This was in exception to five K-feldspar samples for which the coarse grain size were used to detect partial bleaching, using small aliquots. Quartz and K-feldspar extracts were separated using heavy liquids with densities of 2.58 and 2.62 g/cm$^3$. Fractions with density >2.62 g/cm$^3$ were checked for feldspar contamination using the OSL-IR depletion ratio test (Duller, 2003) and the resultant ratios are consistent with unity at 1$\sigma$ for all our samples. Therefore, this fraction is considered to be dominated by quartz. Due to the relatively small sample sizes, no HF etching was conducted on the LEWP1 core samples.

Multi-grain aliquots for the LEWP1 core samples were made by mounting quartz or K-feldspar grains as monolayers on stainless steel discs using Silkospray silicone oil. The size of aliquot is important to detect issues such as incomplete signal resetting or post-depositional mixing (Duller, 2008). For the five coarse grain K-feldspar samples, we used small aliquots (~1 mm) for $D_e$ measurements. For the medium grain size samples, even small aliquots are expected to contain hundreds of grains, thus the choice of aliquot size is meaningless for trying to minimise grain averaging effects. Therefore, for all the medium grain-size quartz and K-feldspar samples, we used ~4 mm medium aliquots for $D_e$ measurements.

Sample LE14-1, collected from Unit A of the Williams Point cliff exposure, yielded more abundant coarse-grained sedimentary material, and it was possible to isolate a sufficient quantity of 212-250 μm grains for single-grain OSL and TT-OSL dating. After 10% HCl and 30% $H_2O_2$ treatments and sieving, 212-250 μm grains were subjected to heavy liquid separation using densities of 2.67 g/cm$^3$ and 2.62 g/cm$^3$ to remove heavy minerals and feldspars, respectively. The remaining quartz grains were etched for 40 minutes in 48% hydrofluoric acid to remove their alpha irradiated external rinds, and to ensure the removal of any non-quartz material remaining after density separation. The etched grains were then washed in 10% hydrochloric acid to remove any precipitated fluorides, and re-sieved to obtain the 212-250 μm fraction. For single-grain measurement, 212-250 μm quartz grains were loaded in standard single-grain aluminium discs drilled with an array of 300 μm x 300 μm holes to ensure that true single-grain resolution was maintained (Arnold et al., 2012).

## S1.2. Dose rate measurement and calculation

The U and Th contents of dose rate samples from LEWP1 were measured using ICP-MS and the K contents were measured using ICP-OES. The U, Th and K contents were converted into alpha, beta and gamma dose rates using conversion factors reported by Guérin et al. (2011). For the alpha dose rate calculation of the LEWP1 core samples, the a-value was set to be 0.04 ± 0.01 for quartz OSL and TT-OSL signals (Rees-Jones, 1995), and 0.10 ± 0.05 for K-feldspar pIRIR signal (Kreutzer et al., 2014). The alpha and beta dose grain size attenuations were calculated following Brennan et al. (1991) and Guérin et al. (2012). The gamma and beta dose rates of sample LE14-1 have been calculated using a combination of *in situ* field gamma-ray spectrometry and low-level beta counting of dried and homogenised, bulk sediment collected directly from the OSL sampling position. Details of dose rate calculations are summarised in Table S1.

Moisture contents for the LEWP1 core samples and sample LE14-1 were measured by weighing the samples before and after drying in an oven at 100°C for three days. Since these sediment samples were sealed, refrigerated and opened soon after collection, the laboratory measured moisture contents are considered to be representative of the field water contents. A relative uncertainty of 25% was assigned to the moisture contents to make allowance for past hydrological variations. Water attenuation for external dose rate was calculated using the correction factors suggested by Aitken (1985).

The internal dose rate of quartz was calculated based on U and Th contents reported by Bowler et al. (2003), and assigned an uncertainty of 30%. The internal dose rate of K-feldspar was calculated assuming an internal K content of 13 ± 1% (Zhao and Li, 2005), an internal Rb content of 400 ± 100 ppm (Huntley and Hancock, 2001), and intrinsic U and Th concentrations of 0.15 ± 0.03 ppm and 0.35 ± 0.07 ppm, respectively (e.g. Arnold et al., 2015). Cosmic dose rates were estimated based on the altitude of the section and burial depth of the samples following Prescott and Hutton (1994).

### S1.3. High-resolution gamma spectrometry measurements

High-resolution gamma spectrometry measurements were performed on dried and powdered bulk sediments using a p-type, high-purity, germanium well detector owing to the limited sample masses available for the LEWP1 core (<15 g per sample). 5.0 – 5.8 g of each sediment sample was sealed in a plastic container for at least 30 days (the equivalent of ~8 half-lives of $^{222}$Rn; $t_{1/2}$ = 3.825 days) to enable the post-radon daughters of $^{214}$Pb and $^{214}$Bi to build up and reach equilibrium with parental $^{226}$Ra activities. Following re-establishment of equilibrium in the post-radon nuclides, we counted the sealed samples in the well detector for 4-6 days (in near 4π geometry to maximise detection efficiency). The specific activities of $^{238}$U (determined from $^{235}$U emissions after correcting for $^{226}$Ra interference, and $^{234}$Th emissions after correcting for $^{228}$Ra interference), $^{226}$Ra (derived from $^{214}$Pb and $^{214}$Bi emissions), $^{210}$Pb, $^{228}$Ra (derived from $^{228}$Ac emissions), $^{228}$Th (derived from $^{212}$Pb, $^{212}$Bi and $^{208}$Tl emissions) and $^{40}$K were measured for each sediment sample, and used to derive the daughter-to-parent isotope ratios for $^{226}$Ra:$^{238}$U, $^{210}$Pb:$^{226}$Ra and $^{228}$Th:$^{228}$Ra shown in Figure 4.

## S1.4. Facilities for $D_e$ measurement

Equivalent doses ($D_e$s) of quartz and K-feldspar were measured using Risø TL/OSL-DA-12 or TL/OSL-DA-20 readers equipped with calibrated $^{90}Sr/^{90}Y$ beta sources for artificial irradiation. For single-grain measurements, spatial variations in the beta dose rate across the disc plane were taken into account by undertaking hole-specific calibrations using gamma-irradiated quartz. Blue LEDs (470 nm, 80 mW/cm$^2$) and IR LEDs (870 nm, 135 mW/cm$^2$) are equipped in the readers for blue light and IR stimulations, respectively. Single grain measurements were made by stimulating individual grains using a focussed 10 mW green (532 nm) laser. Luminescence signals were collected using an EMI9235QA photomultiplier tube. Quartz luminescence signals were detected through 7.5 mm of Schott U-340 (UV) filter. K-feldspar luminescence signals were detected through a combination of Corning 7-59 and Schott BG-39 filters.

For quartz single-aliquot OSL dating, the signals derived from the integral of the first 0.48 s of the decay curve minus a background based on the last 5 s are used for $D_e$ estimation; for single-aliquot K-feldspar dating, the signals derived from the initial 5 s of the decay curve minus a background based on the last 10 s are used for $D_e$ estimation; for single-aliquot TT-OSL dating, signals derived from the integral of the first 0.4 s of the TT-OSL decay curve minus a background based on the last 2 s of the previous main OSL decay curve are used for $D_e$ estimation, in order to minimise the impact of slow components inherited from the previous OSL signal (see section S3.3). Single-grain OSL and TT-OSL dose response curves were constructed using the first 0.17 s of each green laser stimulation after subtracting a mean background count obtained from the last 0.25 s of the signal. The single-grain $D_e$ uncertainties include an empirically determined instrument reproducibility uncertainty of 1.9% for each single-grain measurement, and a dose-response curve fitting uncertainty determined using 1000 iterations of the Monte Carlo method described by Duller (2007).

In all relevant single-aliquot experiments, solar bleaching was carried out using a Dr Hönle UVACUBE 400 solar simulator.

## S1.5. $D_e$ measurement procedures

We have applied single-aliquot quartz OSL dating, single-aliquot K-feldspar pIRIR dating and single-aliquot TT-OSL dating to the LEWP1 core samples, and single-grain OSL and TT-OSL dating to sample LE14-1. Details of the measurement procedures are summarised in Table S3.

**1) *Single-aliquot quartz OSL dating*:** We have employed a conventional single-aliquot regeneration (SAR) procedure (Murray and Wintle, 2000) as detailed in Table S3a for quartz OSL dating. A preheat of 260°C for 10 s and a cutheat of 220°C were selected based on dose recovery tests (see section S3.1). In order to save machine time, we have applied the standard growth curve (SGC) method of Li et al. (2015a) for $D_e$ estimation. For each sample, we first measured the dose response curves (DRCs) of 8-10 discs using the full SAR, and then normalised the different DRCs using an identical regeneration dose (normalisation dose) to construct a SGC. This normalisation process is called re-normalisation (Li et al., 2015a, b) and the obtained SGC is termed the re-normalised SGC. After the establishment of the re-normalised SGC for each sample, we measured only the natural signal, one regenerative dose (normalisation dose) signal and the corresponding test dose signals for all additional discs. The re-normalised natural signals of these discs were then projected onto the SGC to derive their $D_e$s (Li et al., 2015a). It is noted, however, that due to the antiquity of the LEWP1 core sediments, single-aliquot quartz OSL dating was only applicable to four of the LEWP1 core samples, for which the natural OSL signals are non-saturated.

***2) Single-aliquot K-feldspar pIRIR dating:*** A multi-elevated temperature pIRIR (MET-pIRIR) procedure (Li and Li, 2011) was employed for single-aliquot K-feldspar dating of all of the 11 LEWP1 core samples (Table S3b). The MET-pIRIR procedure includes five IR stimulation steps at incrementally higher measurement temperature between 50 to 250°C, and is designed to isolate increasingly stable (none fading) signals through the measurement sequence. The $pIRIR_{250}$ signal, which has been shown to be athermally stable in previous studies (Li and Li, 2011; Fu et al., 2012; Fu, 2014), was used to derive the K-feldspar $D_e$ values from the LEWP1 samples. A re-normalised SGC method (Li et al., 2015b) has been employed in this study to save machine time. Similar to Li et al. (2015b), we observe a common SGC between different K-feldspar samples from the LEWP1 core. Therefore, we have used a uniform K-feldspar SGC, derived from the individual DRCs of different samples, for $D_e$ measurements.

***3) Single-aliquot TT-OSL dating:*** We have applied single-aliquot TT-OSL dating to six samples from the LEWP1 core. The dating procedure of Ademiac et al. (2010) was employed (Table S3c). In this procedure, the TT-OSL signal is induced by a preheat of 260 °C for 10 s. Sensitivity change of the TT-OSL signal is monitored by measuring the OSL signal of a subsequent test dose. The TT-OSL signal has been shown to bleach very slowly in nature (e.g., Demuro et al., 2015). To assess the residual dose for the LEWP1 samples, we measured the TT-OSL $D_e$ of a modern analogue sample collected from the surface of modern playa layer (see Fig. 3 in the main text). This modern sample was assumed to provide a representative residual dose for all the LEWP1 single-aliquot TT-OSL samples and was subtracted from the measured $D_e$ before all age calculations (see results in the main text).

***4) Single-grain OSL and TT-OSL dating:*** Single-grain OSL dating of sample LE14-1 was conducted independently and in parallel to the single-aliquot OSL dating study of the LEWP1 core. Single-grain OSL $D_e$ values were determined using the SAR procedure shown in Table S3d, which employs a preheat of 260°C for 10 s prior to measuring the natural and regenerative dose signals, and a preheat of 160°C for 10 s prior to undertaking the test dose OSL measurements. Single-grain TT-OSL was similarly applied to sample LE14-1 as a means of cross-checking the reliability of the single-grain OSL dating approach over dose ranges of >150 Gy. TT-OSL dating was applied to individual grains of quartz, following the reliable application of this approach at a range of sites (Arnold et al., 2013, 2015; Arsuaga et al., 2014, Demuro et al., 2014, 2015). The single-grain TT-OSL SAR procedure (Table S3e) uses a TT-OSL test dose measurement rather than an OSL test dose measurement to correct for sensitivity change, following single-grain suitability assessments performed by Arnold et al. (2014, 2015) and Demuro et al. (2014, 2015). The TT-OSL SAR procedure also includes two high temperature OSL treatments to prevent TT-OSL signal carry over from previous regenerative dose and test dose measurement cycles. 1000 and 1500 quartz grains were measured for OSL and TT-OSL $D_e$ assessments of LE14-1, respectively. Measured grains were only considered reliable for dating purposes if they satisfied the OSL and TT-OSL SAR quality assurance criteria outlined in Arnold et al. (2013, 2014). To assess the bleachability of the single-grain TT-OSL signal, a set of additional $D_e$ measurements was made on a modern analogue sample collected ~5 cm beneath the present-day lake floor and 20 m offshore from the Williams Point cliff (see results in the main text).

## S2. Additional information on dose rate evaluation for LEWP1 core samples

## S2.1. Comparison of dose rates evaluated using different techniques

In order to cross-check the reliability of our dose rate results, we have compared the dose rates obtained using ICP-MS/OES and HRGS techniques for seven samples. The results for quartz and K-feldspar are shown in Figs. S2a and S2b, respectively. For both minerals, the replicate dose rates obtained using the two approaches are consistent with each other within $1\sigma$ uncertainty ranges. This intrinsic consistency suggests that the dose rate obtained using the ICP-MS/OES technique is reliable for the LEWP1 core samples.

## S2.2. Correction for gamma dose rate heterogeneity

Care was taken during sampling of the LEWP1 core to avoid major lithological boundaries within the gamma dose rate range. However, for eight of our samples we still encountered laminae with varied gamma dose rates (>20% difference) within the surrounding 30 cm. For these samples, we have applied the model of Aitken et al. (1985, p. 289-293) to correct for the layer to layer difference in gamma dose rate. The model of Aitken is based on the principle of superposition. It states that the true gamma dose rate of a sample located in an active medium (medium I) with infinite matrix gamma dose rate of $D_{\gamma1,}$ and at a distance x from a boundary with another active medium (medium II; whose infinite matrix gamma dose rate is $D_{\gamma2}$), can be expressed as:

$$D_{\gamma} = F(x) \cdot D_{\gamma1} + [1-F(x)] \cdot D_{\gamma2}$$

where $D_{\gamma}$ is the true dose rate of the sample, F(x) is an average coefficient representing the contribution of medium I to the gamma dose rate (which can be read from Table H1 of Aitken, 1985), and 1-F(x) represents the contribution of medium II to the gamma dose rate.

Fig. S3 shows the stratigraphic setting of sample LEWP 1.77, which can be used as an example for the gamma dose rate heterogeneity correction in this study. LEWP 1.77 was collected at a depth of 1.77 m in the LEWP1 core from a clay layer whose dry gamma dose rate was measured to be 1.60 ± 0.06 Gy/ka using the elemental concentration data shown in Table 2 (L3, 1.68-1.88 m). Within the gamma dose range of this sample, there are three other sedimentary layers whose gamma dose rates are different from L3. L1 and L4 are two clay layers above and below L3, respectively, with boundaries at 1.66 and 1.88 m. Two samples (LEWP 1.58 and LEWP 1.96) collected from L1 and L4 show that the infinite matrix dry gamma dose rates of the two layers are 2.84 ± 0.11 Gy/ka and 1.05 ± 0.03 Gy/ka, respectively. Between L1 and L3, there is also a 2 cm thick gypsum layer (L2, 1.66-1.68 m) whose gamma dose rate is not directly measured, due to limited material availability. Previous studies have reported that the U, Th and K contents of gypsum in playa or lacustrine sediments are usually much lower than for clay sediments (e.g. Ikeya et al., 1997; Nagar et al., 2010; Mahan and Kay, 2012). Here, we have used the average U, Th and K contents of six gypsum samples from South Australia (U = 0.12 ± 0.03 ppm, Th = 0.17 ± 0.04 ppm, K = 0.63 ± 0.12%) as reported by Nagar et al. (2010) to calculate the gamma dose rate of gypsum layers in our core. These results gave a low dry gamma dose rate of 0.18 ± 0.04 Gy/ka for L2. Based on the model of Aitken, the fractional gamma dose rate contributions of L1 to L4 to sample LEWP 1.77 can be expressed as:

$C_{L1} = 1\text{-}F(1.77\text{-}1.66) = 0.107$
$C_{L2} = [1\text{-} F(1.77\text{-}1.68)] - [1\text{-}F(1.77\text{-}1.66)] = 0.028$
$C_{L3} = 1\text{-} C_{L1}\text{-} C_{L2}\text{-} C_{L4} = 0.759$
$C_{L4} = 1\text{-}F(1.88\text{-}1.77) = 0.107$

and the true dry gamma dose rate of sample LEWP 1.77 can be expressed as:

$$D_{\gamma} = C_{L1} \bullet D_{\gamma L1} + C_{L2} \bullet D_{\gamma L2} + C_{L3} \bullet D_{\gamma L3} + C_{L4} \bullet D_{\gamma L4} = 1.63 \pm 0.13 \text{ Gy/ka}$$

where the error is based on an uncertainty of 10% for $C_{L1}$ to $C_{L4}$. After moisture content attenuation correction, the final gamma dose rate of LEWP 1.77 is 1.04 ± 0.13 Gy/ka, which is only ~2% higher than the original gamma dose rate (uncorrected for gamma heterogeneity) (1.02 ± 0.10 Gy/ka).

The above correction method is applied to seven other samples from the LEWP1 core. The variation of the gamma dose rate due to the above correction is ~2-25% for these samples (Table S1). These gamma dose rate corrections have changed the total environmental dose rates by ~1-7% for quartz and ~1-6% for K-feldspar.

## S3. Luminescence characteristics and performance of procedures

### S3.1. Single-aliquot quartz OSL dating

***Luminescence characteristics:*** A representative quartz OSL decay curve is shown in Fig. S4, which can be seen to exhibit a dominant fast component. The inset of Fig. S4 shows a typical DRC for the quartz OSL signal. The suitability of the SAR procedure is examined using two internal quality assurance criteria: the recycling ratio and recuperation percentage (Murray and Wintle, 2000). An average recycling ratio consistent with unity at 1$\sigma$ and an average recuperation of <1% was observed for all of the samples. These results suggest the sensitivity correction is effective and the impact of charge transfer is negligible, and confirm the suitability of the SAR procedure. In order to validate the chosen preheat/cutheat combination, a dose recovery test (Murray and Wintle, 2003) was conducted. For this test, $\beta$ irradiations of 203 or 276 Gy were given to 20 discs of sample LEWP 0.50 after 1 hour of solar simulator bleaching, and then the discs were measured using the procedure shown in Table S3a. The observed average recovered-to-given dose ratio is 0.95 ± 0.05, supporting the appropriateness of the selected measurement conditions.

***Performance of the SGC method:*** Fig. S5a shows the effect of applying the SGC method to nine discs of sample LEWP 1.40. Prior to re-normalisation, the sensitivity-corrected regenerative signals display obvious inter-aliquot scatter. This scatter is significantly reduced after re-normalisation using a regenerative dose signal of 168 Gy. A similar reduction in scatter is also observed for the sensitivity corrected natural signals ($L_n/T_n$). Li et al. (2015a) suggested that for different samples, it may be possible to establish a "common SGC" that can be used to further save machine time. In order to test this approach, we have compared the SGCs of four non-saturated LEWP1 core samples. Fig. S5b shows that below ~100 Gy, the SGCs of the four samples are similar, supporting the feasibility of a common SGC in this dose range. However, this uniformity does not hold true over dose ranges higher than ~100 Gy, for which significant deviation in SGCs is observed between the four samples. Considering that the $D_e$ values of our samples are all distributed within 130-560 Gy, we have opted to use sample-specific SGCs rather than a common SGC for $D_e$ evaluation. Fig. S5c shows a comparison of the $D_e$ values obtained using the SGC method and the conventional

SAR method. For all of the four samples, the SGC method yields $D_e$ values consistent with that of the SAR method. This suggests that the SGC method can be effectively used for single-aliquot OSL $D_e$ determination in this study.

**S3.2. Single-aliquot K-feldspar pIRIR dating**

***Luminescence characteristics:*** In the MET-pIRIR procedure, five IRSL/pIRIR signals and five DRCs are obtained, corresponding to IR stimulation temperatures of 50, 100, 150, 200 and 250 $^{o}$C. Figs. S6a and S6b show typical IRSL/pIRIR signal decays and corresponding DRCs for the five IRSL/pIRIR signals. For all the LEWP1 core samples, the sensitivity-corrected natural signals lie far below the signal saturation levels, and are therefore within the reliable dating range of the pIRIR protocol. The average recycling ratios for all samples are consistent with unity at 1 σ and the average recuperation values are <2%. A dose recovery test was carried out on 5 discs of sample LEWP 3.63 by applying a β dose of 323 Gy after 4 hours of solar simulator bleaching, and then measuring the pIRIR $D_e$ value using the procedure in Table S3b. After subtraction of the residual dose (i.e., $D_e$ remaining after solar simulator bleaching), the dose recovery ratios for all of the five signals are within 10% of unity (Fig. 6a in the main text). These results confirm the suitability of the MET-pIRIR procedure when applied to a solar bleached and non-thermally treated sample.

***Performance of the SGC method:*** As with the single-aliquot quartz OSL dating procedure, a re-normalisation SGC method (Li et al., 2015b) was used to save machine time and reduce inter-aliquot scatter when deriving K-feldspar pIRIR $D_e$ values. The possibility of establishing a "common SGC" between samples was also explored by comparing the re-normalised IRSL/pIRIR signals for different samples. Figs. S7a-e show that over dose ranges of 0-650 Gy, the re-normalised IRSL and pIRIR DRCs of six samples (all normalised to 442 Gy) are highly reproducible, and can be well fitted using an exponential plus linear function. This suggests we are able to construct a common SGC that is applicable to different samples and further save on $D_e$ measurement time. This is confirmed in Figs. S8a-e, which compare the $D_e$ values obtained using the common SGCs and using the full MET-pIRIR for five IRSL and pIRIR signals of six samples. For all of the five signals, the $D_e$ values derived from the two methods agree with each other at 1σ. We have therefore applied the common SGCs in Fig. S7a-e to the $D_e$ measurements of all LEWP1 core samples.

It should be noted that in Fig. S7, common SGCs are constructed for five MET-pIRIR signals using six LEWP1 core samples. In order to test the applicability of these common SGCs to the other five LEWP1 core samples, which are not used in SGC establishment, we have applied a regenerative dose recovery test, as suggested by Burbidge et al. (2006). For this purpose, we first measured the natural signal and corresponding test dose signals of the five samples using multi-grain aliquots. Two regenerative doses were then given to these aliquots and their signals and corresponding test dose signals were measured. The first regenerative dose (R1) is a normalisation dose, whose signal is used for normalising all data points onto the re-normalised SGCs, as required by the method of Li and Li (2015a, b). The second regenerative dose (R2) is selected to be close to the expected natural dose. The signal of R2 is also re-normalised using the signal of R1, and this re-normalised regenerative signal is subsequently interpolated onto the SGC to calculate a recovered dose. If the recovered dose is consistent with the expected dose R2, it suggests that the common SGC is suitable for the measured sample.

The regenerative dose recovery results for the five samples are shown in Figs. S9a-e for different IRSL and pIRIR signals. For all of the five signals and all of the five samples, the ratios between the recovered doses and the true regenerative doses are within 0.9 to 1.1, and all dose recovery ratios are consistent with unity at the 1 $\sigma$ uncertainty range. These results indicate that the regenerative doses can be successfully recovered when applying the common SGCs. The results in Fig. S9 suggest that the shape of the individual re-normalised SGCs for the five samples are similar to the common SGCs shown in Figs. S7a-e. Thus, it is feasible to use the common SGCs for $D_e$ measurements for these five samples.

### S3.3. Single-aliquot quartz TT-OSL dating

***Luminescence characteristics:*** Representative single-aliquot TT-OSL signal decay curves and corresponding DRC are given in Figs. S10a and S10c. The TT-OSL signal is several orders of magnitude weaker than the previously measured OSL signal, yet strong enough for $D_e$ determination. The sensitivity-corrected natural TT-OSL signals of these samples lie within the linear range of the DRC (Fig. S10c). For the six measured samples, the recycling ratios are consistent with unity at 1$\sigma$ and the recuperation values are all <2%. It is noteworthy that for all samples, a remnant of the main OSL signal (the slow component) underlies the following TT-OSL signal (Fig. S10b) (e.g., Wang et al., 2006). It has been reported that significant slow components can adversely affect single-aliquot TT-OSL dating reliability, particularly when thermally unstable slow components are identified (e.g. Tsukamoto et al., 2008; Brown and Forman, 2012; Demuro et al., 2015). Therefore, removing the influences of slow component TT-OSL is often seen as beneficial for obtaining more accurate ages. To test the impact of this slow component and also to validate the TT-OSL measurement procedure, we conducted a 304 Gy dose recovery test on aliquots of LEWP 0.50 after 8 hours of solar simulator bleaching. We calculated the dose recovery ratio using three background (BG) subtractions methods: a late BG evaluated from the last 5 s of the TT-OSL signal, an early BG evaluated from the 2 s immediately follows the initial 0.4 s TT-OSL signal, and a BG evaluated from the last 2 s of the preceding OSL signal. The latter two methods are both expected to remove the contribution of slow component in the net TT-OSL signal. After residual dose correction (subtraction of $D_e$ remaining after 8 hours of solar simulator bleaching), the recovered-to-given dose ratios obtained are 1.11 ± 0.03, 1.13 ± 0.06 and 0.96 ± 0.07 for the three methods, respectively. The most reliable dose recovery results are therefore obtained using a BG evaluated from the last 2 s of the previous OSL decay curve. Based on these results, we have used the previous OSL BG subtraction method for all our single-aliquot TT-OSL $D_e$ evaluations.

***<u>TT-OSL thermal stability correction:</u>*** Although there is no direct evidence to suggest that the TT-OSL signals of our samples are instable, we have undertaken tentative lifetime corrections for the TT-OSL ages of the LEWP1 core samples, in order to show the impact of such a correction on the final ages. In performing the thermal stability correction, we have assumed that the kinematic parameters of our samples are similar to those reported by Adamiec et al. (2010), and have assumed that the long-term average burial temperature at Williams Point is 20 °C (see discussion in the main text). The lifetime of charge in the TT-OSL trap that is estimated using these trap parameters and mean burial temperature, which is obtained using equation:

$$\tau = \frac{1}{s} e^{(\frac{E}{kT})}$$

where $\tau$ is the lifetime of charge in the trap, s is the escape frequency, E is the trap depth, T is the average temperature and k is the Boltzmann constant. When assuming the TT-OSL signal grows linearly during burial, which is sound for the LEWP1 core samples (Fig. S10c), the TT-OSL age can be corrected for the thermal lifetime using the following equation (Ademiac et al., 2010; Duller et al., 2015):

$$Age_c = -\tau \cdot \ln(1 - \frac{Age_m}{\tau})$$

where $Age_m$ is the measured age and $Age_c$ is the corrected age.

We have applied the above correction method to the TT-OSL ages of six LEWP1 core samples, and compared the corrected and uncorrected TT-OSL ages in Table S5. It is observed that after the thermal stability correction, the TT-OSL ages has increase by ~10-25% for these samples. However, for all of these samples, the thermal lifetime corrected TT-OSL ages are still in agreement with the uncorrected TT-OSL ages and the corresponding replicate pIRIR ages at 1 or 2 $\sigma$. Therefore, the thermal stability corrected and uncorrected TT-OSL ages both equally support the K-feldspar pIRIR dating results.

### S3.4. Single-grain quartz OSL and TT-OSL dating

Application of the SAR quality-assurance criteria of Arnold et al. (2013, 2014) resulted in 5 – 9 % of the measured grains being accepted for $D_e$ determination (Table S4). The majority of remaining grains were eliminated for having very weak $T_n$ signals (60-82%), poor recycling ratios (5-12%) and poor / scattered dose-responses that could not be fitted with the Monte Carlo procedure (8-12%) (Table S4). The proportions of grains rejected during the dose recovery test for failing the various SAR quality-assurance criteria are broadly consistent with the corresponding proportions shown for the natural OSL and TT-OSL $D_e$ measurements of LE14-1.

Fig. S11 shows representative OSL and TT-OSL dose-response/decay curves for grains that passed the SAR quality assurance criteria and were used for dating purposes. The majority of accepted grains display rapidly decaying OSL curves (reaching background levels within 0.5 s) and reasonably bright natural test dose ($T_n$) intensities of 500 – 5000 cts / 0.17 s / 10 Gy

(Fig. S11a). The single-grain OSL dose response curves are generally well-represented by either a single saturating exponential function or a saturating exponential plus linear function, as has been widely reported for individual quartz grains (e.g., Jacobs et al., 2008; Arnold et al., 2011, 2016). The single-grain TT-OSL decay curves have lower $T_n$ intensities of 100 – 1000 cts / 0.17 s / 150 Gy, and the corresponding dose response curves are generally well characterised by single saturating exponential fitting functions and continued signal growth at high doses ($10^2$-$10^3$ Gy) (Fig. S11b).

Dose recovery tests performed on LE14-1 attest to the general suitability of the single-grain OSL and TT-OSL SAR procedures shown in Table S3d-e. A 184 Gy OSL dose recovery test was applied to 1000 artificially bleached quartz grains (bleached using 2 x 1000 s blue diode stimulation at 30$^o$C with a 10,000 s intervening pause), and yielded an accurate measured to given dose ratio of 1.06 ± 0.03 with an overdispersion of 15 ± 4% (Fig. 8a in the main text). A TT-OSL dose-recovery test was performed on a batch of 1000 unbleached grains owing to the long periods of light exposure needed to bleach natural TT-OSL signals down to low residual levels for all grains (e.g., Demuro et al., 2015). A known (218 Gy) laboratory dose of similar magnitude to the expected $D_e$ was added on top of the natural signal for these grains (Fig. 8b in the main text). The recovered dose was then calculated by subtracting the weighted mean natural $D_e$ of sample LE14-1 (194 ± 12 Gy) from the weighted mean $D_e$ of these unbleached and dosed grains (428 ± 26 Gy). This approach yielded a net (i.e., natural-subtracted) recovered-to-given ratio of 1.07 ± 0.09 and an overdispersion value of 27 ± 6% for the unbleached and dosed batch of grains.

## S4. Additional information on Bayesian modelling

### S4.1. Details for testing the two scenarios

Two modelling scenarios were tested for the LEWP sequence: Model 1 assumes continuous lacustrine deposition through time without any major hiatuses or erosional events between identified sedimentary units. For this purpose we inserted a series of *boundaries* within the *P_Sequence* model at -1670, -1400 and -1356 cm AHD to delineate sedimentological changes between Units E, D, C and A. Model 2 does not assume continuous lacustrine deposition and accommodates potential hiatuses and / or erosional discontinuities between the various sedimentary units. Model 2 is conceptually similar to Model 1 but the various units are represented by separate *P_Sequences*, each with delineating start and end *boundaries*, nested within a master *Sequence* according to stratigraphic priors. This model structure is designed to accommodate two potential event boundaries (e.g., the end of one depositional event and the beginning of a subsequent depositional event) at the same depth in the *Sequence* framework, thereby enabling hiatus events to be more explicitly represented in the model. Unit boundary depths were kept the same in both models for consistency.

### S4.2. Bayesian modelling results for Model 1

The Bayesian modelling results for Model 1 are summarised in Table S6, Table S7 and Fig.S12. The 1σ ranges of the posterior likelihood distributions are reduced by an average of 29% for Model 1 when compared with the original dating sample uncertainties. Model 1 returned mean boundary ages of 207.2 ± 15.8 ka to 189.6 ± 10.0 ka for the basal transgressive sediments (Unit E), 189.6 ± 10.0 ka to 170.7 ± 9.6 ka for the deep-water lacustrine phase (Unit D), 170.7 ± 9.6 ka to 145.7 ± 13.6 ka for the palaeo-playa deposits (Unit C), and 145.7 ± 13.6 ka to 127.2 ± 12.7 ka for the shallow-water lacustrine unit (Unit A) (Table S6). The average sedimentation rates of these four units (from bottom to top) are 0.04, 0.14, 0.02 and 0.20 m/ka using the posterior boundary age distributions of Model 1.

The Bayesian modelling results for Model 2 are summarised in Table 3 and Fig. 10 in the main text and Table S7. The main difference between the two modelling results is the identification of a potential 23 ka depositional hiatus between Units D and C (181-158 ka) in Model 2 (Table 3 in the main text). This temporal gap is confirmed as being statistically significant at the 95.4% CI using the *difference* query (modelled temporal range between the upper boundary of Unit D and the lower boundary of Unit C does not overlap with 0 ka at the 95.4% CI; see Table S7 footnote).

### S4.3. Assessing the statistical validity of the modelling results

In order to assess the statistical validity of the modelling results, we have used the model agreement index ($A_{model}$), which measures the overlap between the measurement data and the modelled posterior distributions as a whole, and the overall agreement index ($A_{overall}$), which is a product of the individual agreement indices ($A_i$: correspondence between individual likelihood and posterior distributions) for each modelled dating sample (Bronk-Ramsey, 2009). The continuous deposition model (Model 1) yielded $A_{model}$ and $A_{overall}$ values of 46 and 55%, which are below the recommended internal consistency threshold of 60%, and likely reflect the rigidity of the prior constraints (continuous deposition and absence of temporal hiatuses between units). The non-continuous deposition model (Model 2) produced $A_{model}$ and $A_{overall}$ values of 71 and 76%, which are higher than the preferable acceptance threshold value of 60% (Bronk-Ramsey, 2009) and are indicative of adequate modelling agreement. None of the likelihoods returned individual posterior outlier probabilities of 60-100%, which would potentially constitute major statistical outliers and would contribute relatively little to the modelled chronology when using the general *outlier* function (Table 3 in the main text and Table S6 in the SI).

We favour Model 2 (Table 3 and Fig. 10 in the main text) for reconstructing the final lacustrine chronological sequence at Williams Point based on its superior diagnostic indicators (agreement indices and posterior outlier probabilities), and the fact that the stratigraphic assumptions of this model (non-continuous deposition) are in better accordance with sedimentological interpretations for the LEWP1 core and the broader Lake Eyre record (Magee et al., 1995; Cohen et al., 2015).

## References


Adamiec, G., Duller, G.A.T., Roberts, H.M., Wintle, A.G., 2010. Improving the TT-OSL SAR protocol through source trap characterisation. Radiat. Meas. 45, 768–777.

Aitken, M.J., 1985. Thermoluminescence Dating. Academic Press, London.

Aitken, M.J., 1998. An Introduction to Luminescence Dating. Oxford University Press, London.

Arnold, L.J., Duval, M., Demuro, M., Spooner, N.A., Santonja, M., Pérez-González, A., 2016. OSL dating of individual quartz 'supergrains' from the Ancient Middle Palaeolithic site of Cuesta de la Bajada, Spain. Quat. Geochronol. 36, 78–101.

Arnold, L.J., Demuro, M., Parés, J.M., Pérez-González, A., Arsuaga, J.L., Bermúdez de Castro, J.M., Carbonell, E., 2015. Evaluating the suitability of extended-range luminescence dating techniques over early and Middle Pleistocene timescales: Published datasets and case studies from Atapuerca, Spain. Quat. Int. 389, 167–190.

Arnold, L.J., Demuro, M., Parés, J.M., Arsuaga, J.L., Aranburu, A., Bermúdez de Castro, J.M., Carbonell, E., 2014. Luminescence dating and palaeomagnetic age constraint on hominins from Sima de los Huesos, Atapuerca, Spain. J. Hum. Evol. 67, 85-107.

Arnold, L.J., Demuro, M., Navazo Ruiz, M., Benito-Calvo, A., Pérez-González, A., 2013. OSL dating of the Middle Palaeolithic Hotel California site, Sierra de Atapuerca, north-central Spain. Boreas 42, 285–305.

Arnold, L.J., Demuro, M., Navazo Ruiz, M., 2012. Empirical insights into multi-grain averaging effects from ‘pseudo’ single-grain OSL measurements. Radiat. Meas. 47, 652–658.

Arnold, L. J., Roberts, R. G., MacPhee, R. D. E., Haile, J. S., Brock, F., Möller, P., Froese, D. G., Tikhonov, A. N., Chivas, A. R., Gilbert, M. T. P., Willerslev, E., 2011. Paper II – Dirt, dates and DNA: OSL and radiocarbon chronologies of perennially frozen sediments in Siberia and their implications for sedimentary ancient DNA studies. Boreas 40, 417–445.

Arsuaga, J.L., Martínez, I., Arnold, L.J., Aranburu, A., Gracia-Téllez, A., Sharp, W.D., Quam, R.M., Falguères, C., Pantoja-Pérez, A., Bischoff, J., Poza-Rey, E., Parés, J.M., Carretero, J.M., Demuro, M., Lorenzo, C., Sala, N., Martinón-Torres, M., García, N., Alcázar de Velasco, A., Cuenca-Bescós, G., Gómez-Olivencia, A., Moreno, D., Pablos, A., Shen, C.-C., Rodríguez, L., Ortega, A.I., García, R., Bonmatí, A., Bermúdez de Castro, J.M., Carbonell, E. 2014., Neanderthal roots: Cranial and chronological evidence from Sima de los Huesos. Science, 344, 1358–1363.

Bowler, J.M., Johnston, H., Olley, J.M., Prescott, J.R., Roberts, R.G., Shawcross, W., Spooner, N.A., 2003. New ages for human occupation and climatic change at Lake Mungo, Australia. Nature 421, 837–840.

Brennan, B.J., Lyons, R.G., Phillips, S.W., 1991. Attenuation of alpha particle track dose for spherical grains. International Journal of Radiation Applications and Instrumentation. Part D. Nuclear Tracks and Radiation Measurements 18, 249–253.

Bronk Ramsey, C., 2009. Bayesian analysis of radiocarbon dates. Radiocarbon 51, 337–360.

Brown, N.D., Forman, S.L., 2012. Evaluating a SAR TT-OSL protocol for dating fine-grained quartz within Late Pleistocene loess deposits in the Missouri and Mississippi river valleys, United States. Quat. Geochronol. 12, 87–97.

Burbidge, C.I., Duller, G.A.T., Roberts, H.M., 2006. De determination for young samples using the standardised OSL response of coarse-grain quartz. Radiat. Meas. 41, 278–288.

Cohen, T.J., Jansen, J.D., Gliganic, L.A., Larsen, J.R., Nanson, G.C., May, J.-H., Jones, B.G., Price, D.M., 2015. Hydrological transformation coincided with megafaunal extinction in central Australia. Geology 43, 195–198.

Demuro, M., Arnold, L.J., Parés, J.M., Sala, R., 2015. Extended-range luminescence chronologies suggest potentially complex bone accumulation histories at the Early-to-Middle Pleistocene palaeontological site of Huéscar-1 (Guadix-Baza basin, Spain). Quat. Int. 389, 191–212.

Demuro, M., Arnold, L.J., Parés, J.M., Pérez-González, A., Ortega, A.I., Arsuaga, J.L., Bermúdez de Castro, J.M., Carbonell, E., 2014. New luminescence ages for the Galería Complex archaeological site: Resolving chronological uncertainties on the Acheulean record of the Sierra de Atapuerca, northern Spain. PLOS ONE 9, e110169.

Duller, G.A.T., 2003. Distinguishing quartz and feldspar in single grain luminescence measurements. Radiat. Meas. 37, 161–165.

Duller, G.A.T., 2007. Assessing the error on equivalent dose estimates derived from single aliquot regenerative dose measurements. Ancient TL 25, 15–24.

Duller, G.A.T., 2008. Single-grain optical dating of Quaternary sediments: why aliquot size matters in luminescence dating. Boreas 37, 589–612.

Duller, G.A.T., Tooth, S., Barham, L., Tsukamoto, S., 2015. New investigations at Kalambo Falls, Zambia: Luminescence chronology, site formation, and archaeological significance. J. Hum. Evol. 85, 111–125.

Fu, X., 2014. The De (T, t) plot: A straightforward self-diagnose tool for post-IR IRSL dating procedures. Geochronometria 41, 315–326.

Fu, X., Li, B., Li, S.H., 2012. Testing a multi-step post-IR IRSL dating method using polymineral fine grains from Chinese loess. Quat. Geochronol.10, 8–15.
Guérin, G., Mercier, N., Adamiec, G., 2011. Dose rate conversion factors: update. Ancient TL 29, 5–8.
Guérin, G., Mercier, N., Nathan, R., Adamiec, G., Lefrais, Y., 2012. On the use of the infinite matrix assumption and associated concepts: A critical review. Radiat. Meas. 47, 778–785.
Huntley, D.J., Hancock, R.G.V., 2001. The Rb content of K-feldspar grains being measured in optical dating. Ancient TL 19, 43–46
Ikeya, M., Oka, T., Omura, T., Okawa, M., Takeno, S., 1997. Evaluation of environment using electron spin resonance (ESR): microscope images of gypsum ($CaSO_4$ $2H_2O$) microcrystals in bore-hole cores at Konya Basin, Turkey. Japan Review 193–208.
Kreutzer, S., Schmidt, C., DeWitt, R., Fuchs, M., 2014. The a-value of polymineral fine grain samples measured with the post-IR IRSL protocol. Radiat. Meas. 69, 18–29.
Li, B., Li, S.H., 2011. Luminescence dating of K-feldspar from sediments: A protocol without anomalous fading correction. Quat. Geochronol. 6, 468–479.
Li, B., Roberts, R.G., Jacobs, Z., Li, S.H., 2015a. Potential of establishing a "global standardised growth curve" (gSGC) for optical dating of quartz from sediments. Quat. Geochronol. 27,
Li, B., Roberts, R.G., Jacobs, Z., Li, S.H., Guo, Y.J., 2015b. Construction of a "global standardised growth curve" (gSGC) for infrared stimulated luminescence dating of K-feldspar. Quat. Geochronol. 27, 119–130.
Jacobs, Z., Wintle, A.G., Roberts, R.G., Duller, G.A.T., 2008. Equivalent dose distributions from single grains of quartz at Sibudu, South Africa: context, causes and consequences for optical dating of archaeological deposits. J. Archaeol. Sci. 35, 1808–1820.
Magee, J.W., Bowler, J.M., Miller, G.H., Williams, D.L.G., 1995. Stratigraphy, sedimentology, chronology and palaeohydrology of Quaternary lacustrine deposits at Madigan Gulf, Lake Eyre, south Australia. Palaeogeogr. Palaeoclimatol. Palaeoecol. 113, 3–42.
Mahan, S., Kay, J., 2012. Building on previous OSL dating techniques for gypsum: A case study from Salt Basin playa, New Mexico and Texas. Quat. Geochronol. 10, 345–352.
Murray, A.S., Wintle, A.G., 2000. Luminescence dating of quartz using an improved single-aliquot regenerative-dose protocol. Radiat. Meas. 32, 57–73.
Murray, A.S., Wintle, A.G., 2003. The single aliquot regenerative dose protocol: potential for improvements in reliability. Radiat. Meas. 37, 377–381.
Nagar, Y.C., Sastry, M.D., Bhushan, B., Kumar, A., Mishra, K.P., Shastri, A., Deo, M.N., Kocurek, G., Magee, J.W., Wadhawan, S.K., Juyal, N., Pandian, M.S., Shukla, A.D., Singhvi, A.K., 2010. Chronometry and formation pathways of gypsum using Electron Spin Resonance and Fourier Transform Infrared Spectroscopy. Quat. Geochronol. 5, 691–704.
Prescott, J.R., Hutton, J.T., 1994. Cosmic ray contributions to dose rates for luminescence and ESR dating: Large depths and long-term time variations. Radiat. Meas. 23, 497–500.
Rees-Jones, J., 1995. Optical dating of young sediments using fine-grain quartz. Ancient TL 13, 9–14.
Tsukamoto, S., Duller, G.A.T., Wintle, A.G., 2008. Characteristics of thermally transferred optically stimulated luminescence (TT-OSL) in quartz and its potential for dating sediments. Radiat. Meas. 43, 1204–1218.
Wang, X.L., Wintle, A.G., Lu, Y.C., 2006. Thermally transferred luminescence in fine-grained quartz from Chinese loess: Basic observations. Radiat. Meas. 41, 649–658.
Zhao, H., Li, S.H., 2005. Internal dose rate to K-feldspar grains from radioactive elements other than potassium. Radiat. Meas. 40, 84–93.

Table S1 A summary of the dose rate results

| **Sample** | **Depth below surface (m)** | **AHD Depth (m)** | **Mineral** | **Grain size (μm)** | **Moisture content (%)**[a] | **Alpha dose rate (Gy/ka)**[b] | **Beta dose rate (Gy/ka)**[b] | **Uncorrected gamma dose rate(Gy/ka)**[b] | **Corrected Gamma dose rate (Gy/ka)**[b] | **Cosmic ray (Gy/ka)** | **External dose rate (Gy/ka)** | **Internal dose rate (Gy/ka)** | **Total dose rate (Gy/ka)** |
|---|---|---|---|---|---|---|---|---|---|---|---|---|---|
| **LE14-1** | 0.70 | -10.74 | Quartz | 212-250 | 60 | - | 0.85±0.04 | 0.47±0.02 | - | 0.03±0.01 | 1.35±0.08 | 0.03±0.01 | 1.38±0.08 |
| **LEWP 0.50** | 0.50 | -13.93 | Quartz | 45-63 | 47 | 0.06±0.01 | 0.74±0.07 | 0.44±0.04 | 0.47±0.06 | 0.20±0.02 | 1.47±0.10 | 0.02±0.01 | 1.49±0.10 |
| | | | K-feldspar | 45-63 | | 0.15±0.06 | 0.74±0.07 | 0.44±0.04 | 0.47±0.06 | | 1.56±0.11 | 0.29±0.04 | 1.85±0.12 |
| **LEWP 0.89** | 0.89 | -14.32 | Quartz | 45-63 | 36 | 0.10±0.02 | 0.96±0.08 | 0.61±0.05 | 0.58±0.07 | 0.18±0.02 | 1.82±0.11 | 0.02±0.01 | 1.84±0.11 |
| | | | K-feldspar | 90-180 | | 0.11±0.05 | 0.93±0.08 | 0.61±0.05 | 0.58±0.07 | | 1.80±0.12 | 0.64±0.17 | 2.44±0.21 |
| **LEWP 1.21** | 1.21 | -14.64 | K-feldspar | 63-90 | 49 | 0.15±0.06 | 0.92±0.09 | 0.60±0.06 | 0.62±0.08 | 0.18±0.02 | 1.87±0.14 | 0.39±0.06 | 2.26±0.15 |
| **LEWP 1.40** | 1.40 | -14.83 | Quartz | 45-63 | 48 | 0.12±0.03 | 1.10±0.11 | 0.74±0.07 | 0.85±0.10 | 0.17±0.02 | 2.24±0.15 | 0.02±0.01 | 2.26±0.15 |
| | | | K-feldspar | 45-63 | | 0.30±0.13 | 1.10±0.11 | 0.74±0.07 | 0.85±0.10 | | 2.42±0.19 | 0.29±0.04 | 2.72±0.20 |
| **LEWP 1.58** | 1.58 | -15.01 | Quartz | 45-63 | 50 | 0.38±0.11 | 2.36±0.24 | 1.81±0.18 | 1.47±0.19 | 0.17±0.02 | 4.38±0.33 | 0.02±0.01 | 4.40±0.33 |
| | | | K-feldspar | 45-63 | | 0.95±0.47 | 2.36±0.25 | 1.81±0.18 | 1.47±0.19 | | 4.96±0.56 | 0.29±0.04 | 5.25±0.56 |
| **LEWP 1.77** | 1.77 | -15.20 | K-feldspar | 90-180 | 50 | 0.22±0.11 | 1.36±0.14 | 1.02±0.10 | 1.04±0.13 | 0.16±0.02 | 2.80±0.20 | 0.64±0.17 | 3.41±0.28 |
| **LEWP 2.15** | 2.15 | -15.58 | Quartz | 45-63 | 53 | 0.11±0.03 | 0.95±0.10 | 0.65±0.06 | - | 0.15±0.02 | 1.85±0.12 | 0.02±0.01 | 1.88±0.12 |
| | | | K-feldspar | 45-63 | | 0.27±0.11 | 0.95±0.10 | 0.65±0.06 | - | | 2.02±0.16 | 0.29±0.04 | 2.31±0.17 |
| **LEWP 2.35** | 2.35 | -15.78 | K-feldspar | 90-180 | 49 | 0.11±0.05 | 0.95±0.10 | 0.64±0.06 | - | 0.15±0.02 | 1.85±0.13 | 0.64±0.17 | 2.49±0.21 |
| **LEWP 2.73** | 2.73 | -16.16 | Quartz | 45-63 | 48 | 0.13±0.03 | 1.09±0.11 | 0.76±0.07 | - | 0.14±0.01 | 2.13±0.14 | 0.02±0.01 | 2.15±0.14 |
| | | | K-feldspar | 45-63 | | 0.33±0.14 | 1.09±0.11 | 0.76±0.07 | - | | 2.33±0.19 | 0.29±0.04 | 2.63±0.20 |
| **LEWP 3.63** | 3.63 | -17.06 | Quartz | 45-63 | 36 | 0.06±0.02 | 0.48±0.04 | 0.33±0.03 | 0.35±0.04 | 0.13±0.01 | 1.03±0.06 | 0.02±0.01 | 1.05±0.06 |
| | | | K-feldspar | 45-63 | | 0.15±0.06 | 0.49±0.04 | 0.33±0.03 | 0.35±0.04 | | 1.12±0.09 | 0.29±0.04 | 1.41±0.10 |
| **LEWP 3.82** | 3.82 | -17.25 | Quartz | 45-63 | 37 | 0.08±0.02 | 0.66±0.06 | 0.45±0.04 | 0.44±0.05 | 0.13±0.01 | 1.30±0.08 | 0.02±0.01 | 1.32±0.08 |
| | | | K-feldspar | 63-90 | | 0.14±0.06 | 0.65±0.06 | 0.45±0.04 | 0.44±0.05 | | 1.36±0.10 | 0.39±0.06 | 1.75±0.12 |

[a] The relative uncertainty for the moisture contents is set to be 25%.

[b] For the LEWP1 core samples, no HF etching was conducted on the quartz and K-feldspar grains. The alpha, beta and gamma dose rates are calculated using U, Th and K contents measured using ICP-MS and ICP-OES (Table 1 in the main text). For samples which have heterogeneous gamma dose rates within 30 cm, the gamma dose rate is corrected using the model of Aitken (1985, p289-293) (see section S2.2.) For sample

LE14-1, HF etching has been conducted on the measured quartz grains. Therefore, no alpha dose rate is included for this sample. The beta dose rate of this sample has been measured using low-level beta counting and the gamma dose rate has been determined using *in situ* gamma spectrometry measurements. Any spatial heterogeneity in the gamma dose rate of this sample will have been adequately represented using *in situ* gamma spectrometry; hence there is no need to incorporate a gamma dose rate correction for this sample. The cosmic dose rate of LE14-1 is much smaller than the other samples because it was sampled from the lacustrine sequence underlying the Williams Point cliff exposure – i.e. it is overlain by 16 m of overburden thickness, whereas the other samples have been collected from the lake floor and hence were devoid of this overburden thickness.

Table S2 A summary of the HRGS results

| | $^{238}$U (Bq/kg) | $^{226}$Ra (Bq/kg) | $^{210}$Pb (Bq/kg) | $^{228}$Ra (Bq/kg) | $^{228}$Th (Bq/kg) | $^{40}$K (Bq/kg) |
|---|---|---|---|---|---|---|
| LEWP0.89 | 48.53 ± 2.41 | 51.70 ± 0.79 | 53.69 ± 3.40 | 18.66 ± 0.96 | 19.47 ± 0.69 | 293.62 ± 8.23 |
| LEWP1.21 | 45.74 ± 3.01 | 51.37 ± 0.80 | 55.61 ± 4.48 | 28.73 ± 1.03 | 28.91 ± 0.85 | 331.50 ± 9.06 |
| LEWP1.40 | 75.67 ± 3.77 | 73.75 ± 1.10 | 75.43 ± 4.00 | 28.18 ± 1.19 | 27.71 ± 0.94 | 354.16 ± 10.11 |
| LEWP1.58 | 264.77 ± 6.47 | 264.20 ± 3.27 | 268.49 ± 9.23 | 28.46 ± 1.32 | 29.40 ± 1.27 | 364.16 ± 10.39 |
| LEWP1.77 | 124.23 ± 3.61 | 124.39 ± 1.62 | 124.67 ± 6.11 | 28.68 ± 1.06 | 27.74 ± 0.99 | 329.53 ± 9.01 |
| LEWP2.73 | 81.16 ± 3.63 | 87.41 ± 1.27 | 95.34 ± 4.90 | 26.09 ± 1.20 | 26.18 ± 0.97 | 297.70 ± 9.24 |
| LEWP3.82 | 45.42 ± 2.36 | 45.13 ± 0.70 | 46.43 ± 2.80 | 11.85 ± 0.75 | 12.46 ± 0.57 | 173.20 ± 5.68 |

Table S3 Summary of single-aliquot $D_e$ measurement procedures for the LEWP1 core samples and the single-grain $D_e$ measurement procedures for sample LE14-1.

| | **(a) Single-aliquot OSL** | **(b) Single-aliquot MET-pIRIR** | **(c) Single-aliquot TT-OSL** | **(d) Single-grain OSL** | **(e) Single-grain TT- OSL** |
|---|---|---|---|---|---|
| ***Step*** | ***Treatment / Observed*** | ***Treatment / Observed*** | ***Treatment/Observed*** | ***Treatment / Observed*** | ***Treatment / Observed*** |
| 1 | Dose (natural or regenerative) | Dose (natural or regenerative) | Dose (natural or regenerative) | Dose (natural or regenerative) | Dose (natural or regenerative) |
| 2 | Preheat (260°C, 10s) | Preheat (300°C, 10s) | Preheat (260°C, 10s) | IRSL (50ºC, 60s) [a] | Preheat (260°C, 10s) |
| 3 | **OSL (125°C, 40s) / $L_x$** | IRSL (50°C, 100s) / $L_{x50}$ | OSL (125°C, 100s) | Preheat (260°C, 10s) | SG OSL (125°C, 3s) |
| 4 | Test dose | IRSL (100°C, 100s) / $L_{x100}$ | Preheat (260°C, 10s) | **SG OSL (125°C, 2s) / $L_x$** | Preheat (260°C, 10s) |
| 5 | Cutheat (220 °C) | IRSL (150°C, 100s) / $L_{x150}$ | **OSL (125°C, 100s) / $L_x$** | Test dose | **SG OSL (125°C, 3s) / $L_x$** |
| 6 | **OSL (125°C, 40s) / $T_x$** | IRSL (200°C, 100s) / $L_{x200}$ | Test dose | Preheat (160°C, 10s) | OSL (280ºC, 400 s) |
| 7 | OSL hot bleach (280°C, 40s) | **IRSL (250°C, 100s) / $L_{x250}$** | Preheat (220°C, 10s) | **SG OSL (125°C, 2s) / $T_x$** | Test dose |
| 8 | Return to step 1 | Test dose | **OSL (125°C, 100s) / $T_x$** | Return to step 1 | Preheat (260°C, 10s) |
| 9 | | Preheat (300°C, 10s) | Thermal treatment (350°C, 200s) | | SG OSL (125°C, 3s) |
| 10 | | IRSL (50°C, 100s) / $T_{x50}$ | Return to step 1 | | Preheat (260°C, 10s) |
| 11 | | IRSL (100°C, 100s) / $T_{x100}$ | | | **SG OSL (125°C, 3s) / $T_x$** |
| 12 | | IRSL (150°C, 100s) / $T_{x150}$ | | | OSL hot bleach (290 $^o$C, 400s) |
| 13 | | IRSL (200°C, 100s) / $T_{x200}$ | | | |
| 14 | | **IRSL (250°C, 100s) / $T_{x250}$** | | | |
| 15 | | IRSL hot bleach (320°C, 100s) | | | |
| 16 | | Return to step 1 | | | |

[a] Step 2 is only included in the single-grain OSL SAR procedure when measuring the OSL-IR depletion ratio (Duller, 2003). For single-aliquot OSL, single-aliquot TT-OSL and single-grain TT-OSL $D_e$ measurements, feldspar contamination was checked by measuring the OSL-IR depletion ratio separately and in the standard manner shown for single-grain OSL measurements.

Table S4 Summary of the single-grain OSL and TT-OSL classification statistics for the natural $D_e$ and dose recovery test (DRT) measurements of sample LE14-1. The proportion of grains that were rejected from the final $D_e$ estimation after applying the various SAR quality assurance criteria of Arnold et al. (2013, 2014) are shown in rows 5-14.

| **Sample name** | **LE14-1** | **LE14-1** | **LE14-1** | **LE14-1** |
|---|---|---|---|---|
| **SAR measurement type** | OSL $D_e$ | OSL DRT | TT-OSL $D_e$ | TT-OSL DRT |
| **Total measured grains** | 1000 | 1000 | 1500 | 1000 |
| **Reason for rejecting grains from $D_e$ analysis** | % | % | % | % |
| $T_n$ <3$\sigma$ background | 60 | 63 | 82 | 82 |
| Low-dose recycling ratio ≠ 1 at ±2$\sigma$ | 8 | 7 | 5 | 4 |
| High-dose recycling ratio ≠ 1 at ±2$\sigma$ | 4 | 2 | – [a] | – [a] |
| OSL-IR depletion ratios <1 at ±2σ | 3 | 3 | 0 | 0 |
| 0 Gy $L_x/T_x$ >5% $L_n/T_n$ | 2 | 1 | <1 | 0 |
| Non-intersecting grains ($L_n/T_n$ > dose response curve saturation) | <1 | <1 | 0 | 0 |
| Saturated grains ($L_n/T_n \geq$ dose response curve $I_{max}$ at ±2σ) | <1 | <1 | 0 | 0 |
| Anomalous dose response / unable to perform Monte Carlo fit | 12 | 15 | 8 | 9 |
| **Sum of rejected grains (%)** | 91 | 92 | 95 | 95 |
| **Sum of accepted grains (%)** | 9 | 8 | 5 | 5 |

[a] The high-dose recycling ratio criteria was not applied to the single-grain TT-OSL $D_e$ estimation procedure (see Arnold et al., 2014).

Table S5 Summary of single-aliquot TT-OSL thermal stability correction results

| **Sample** | **K-feldspar pIRIR age (ka)** | **Uncorrected TT-OSL age ($Age_m$, ka)** | **Thermal lifetime corrected TT-OSL age ($Age_c$, ka)** | **Increase of age after correction (%)** |
|---|---|---|---|---|
| LEWP 0.50 | 147.68±12.04 | 132.71 ± 14.48 | 150.79 ± 18.80 | 14 |
| LEWP 0.89 | 192.41±19.55 | 216.76 ± 18.10 | 271.72 ± 29.00 | 25 |
| LEWP 1.58 | 120.09±14.13 | 101.89 ± 11.35 | 112.10 ± 13.79 | 10 |
| LEWP 2.15 | 182.30±15.83 | 167.62 ± 17.70 | 197.98 ± 24.96 | 18 |
| LEWP 2.73 | 182.58±16.82 | 169.86 ± 13.56 | 201.14 ± 19.26 | 18 |
| LEWP 3.82 | 223.49±17.71 | 188.18 ± 23.70 | 227.69 ± 35.20 | 21 |

Table S6 Summary of Bayesian modelling results obtained using a continuous deposition modelling scenario (Model 1). The unmodelled and modelled age estimates have been rounded to the nearest 50 years.

| Boundary | Dating sample | Depth (cm AHD) | Unmodelled age (years before AD2014) | | | Modelled age (years before AD2014) | | | Agreement index ($A_i$) (%) | Posterior outlier probability (%) |
|---|---|---|---|---|---|---|---|---|---|---|
| | | | 68.2% range | 95.4% range | Mean ± 1σ | 68.2% range | 95.4% range | Mean ± 1σ | | |
| Unit A | | -985 | | | | 117900 – 140350 | 103850 – 150800 | 127200 ± 12650 | | |
| | LE14-1 (SG OSL+SG TT-OSL) | -1074 | 122300 – 140800 | 113450 – 149700 | 131550 ± 9050 | 122750 – 142450 | 110850 – 153500 | 131650 ± 11100 | 100.5 | 4 |
| Unit A – Unit C | | -1356 | | | | 132350 – 159250 | 121750 – 172550 | 145700 ± 13550 | | |
| | LEWP 0.5 (pIRIR) | -1393 | 135400 – 159950 | 123600 – 171750 | 147700 ± 12050 | 157650 – 174950 | 147750 – 182300 | 165500 ± 8600 | 57.1 | 0 |
| Unit C – Unit D | | -1400 | | | | 161550 – 180950 | 151450 – 188750 | 170650 ± 9550 | | |
| | LEWP 0.89 (pIRIR) | -1432 | 172450 – 212350 | 153300 – 231500 | 192400 ± 19550 | 164550 – 182150 | 155600 - 190000 | 173000 ± 8550 | 85.6 | 7 |
| | LEWP 1.21 (pIRIR) | -1464 | 186450 – 220250 | 170250 – 236450 | 203350 ± 16550 | 167250 – 183450 | 159650 – 190900 | 175250 ± 7750 | 37.8 | 18 |
| | LEWP 2.15 (pIRIR) | -1558 | 166150 – 198450 | 150650 – 213950 | 182300 ± 15850 | 174350 – 189400 | 167250 – 196050 | 181800 ± 7250 | 133.2 | 2 |
| | LEWP 2.35 (pIRIR) | -1578 | 180850 – 221450 | 161350 – 240950 | 201150 ± 19900 | 175550 – 191100 | 168000 – 198050 | 183200 ± 7500 | 92.6 | 6 |
| | LEWP 2.73 (pIRIR) | -1616 | 165400 – 199750 | 148950 – 216200 | 182600 ± 16800 | 177200 – 194200 | 169100 – 202600 | 185800 ± 8300 | 129.7 | 1 |
| Unit D – Unit E | | -1670 | | | | 178800 – 198750 | 170500 - 209650 | 189550 ± 9950 | | |
| | LEWP 3.63 (pIRIR) | -1706 | 156400 – 193000 | 138800 – 210600 | 174700 ± 17950 | 187050 – 208050 | 177200 – 218450 | 197800 ± 10300 | 68.8 | 1 |
| | LEWP 3.82 (pIRIR) | -1725 | 205450 – 241550 | 188050 – 258900 | 223500 ± 17700 | 189100 – 214050 | 178300 – 228050 | 202700 ± 12550 | 71.5 | 11 |
| Unit E bottom | | -1743 | | | | 189700 – 220050 | 179800 – 237100 | 207200 ± 15750 | | |

Table S7 Bayesian modelled posterior age ranges and depositional durations for the LEWP stratigraphic units. The modelled durations of potential temporal hiatuses between successive unit boundaries are also shown for Model 2 (Unit A – Unit C boundary etc). Posterior ages/durations are presented as the 68.2% and 95.4% highest probability density ranges. The mean and 1σ uncertainty ranges of the modelled posterior distributions are shown for comparison (assuming a normally distributed probability density function).

| **Unit / boundary** | **Time variable** | **Modelled age (years before AD2014)** [a] | | | **Modelled duration (years)** [a, b] | | |
|---|---|---|---|---|---|---|---|
| | | **68.2% range** | **95.4% range** | **Mean ± 1σ** | **68.2% range** | **95.4% range** | **Mean ± 1σ** |
| *(a) Model 1 – continuous deposition* | | | | | | | |
| Unit A | age range | 125450 – 148550 | 112450 - 162250 | 136400 ± 12700 | | | |
| Unit A | duration | | | | -9 – 23200 | -1 – 48300 | 18450 ± 15100 |
| Unit C | age range | 147600 – 171300 | 133950 – 181050 | 158150 ± 12150 | | | |
| Unit C | duration | | | | 2900 – 35300 | -10 – 52850 | 25000 ± 15650 |
| Unit D | age range | 170600 – 189500 | 160550 – 199850 | 180100 ± 9750 | | | |
| Unit D | duration | | | | 10 – 23950 | 2 – 44750 | 18900 ± 13450 |
| Unit E | age range | 184750 – 208450 | 174700 – 223750 | 198400 ± 12600 | | | |
| Unit E | duration | | | | 1 – 21850 | -9 – 47900 | 17700 ± 15500 |
| *(b) Model 2 – Non-continuous deposition* | | | | | | | |
| Unit A | age range | 114000 – 141700 | 80800 – 149000 | 121500 ± 17600 | | | |
| Unit A | duration | | | | 12 – 19750 | 2 – 49000 | 16850 ± 16200 |
| Unit A – Unit C boundary | duration | | | | -9 – 15500 | -9 – 35250 | 12850 ± 11500 |
| Unit C | age range | 140000 – 163300 | 125750 – 174450 | 150300 ± 12300 | | | |
| Unit C | duration | | | | -9 – 17700 | -9 - 43550 | 15050 ± 13950 |
| Unit C – Unit D boundary | duration | | | | 7150 – 34450 | 2 – 45500 | 22900 ± 12800 |
| Unit D | age range | 177800 - 194750 | 168900 – 202500 | 185950 ± 8500 | | | |
| Unit D | duration | | | | -9 – 12700 | -9 – 29250 | 10350 ± 9200 |
| Unit D – Unit E boundary | duration | | | | -9 – 11500 | -9 – 26000 | 9450 ± 8050 |
| Unit E | age range | 196750 – 220500 | 186450 – 237350 | 210900 ± 14150 | | | |
| Unit E | duration | | | | 4 – 24600 | -9 – 55000 | 20750 ± 19900 |

[a] Modelled age ranges were calculated from the posterior probabilities of the upper and lower boundaries (top and bottom) of each stratigraphic unit (see Table S6 for Model 1 and Table 3 in the main text for Model 2) using the *date* query function in OxCal v4.2. Modelled durations were calculated using the *difference* query function, and provide the temporal range between the posterior probability density distributions of successive stratigraphic boundaries.

[b] The OxCal *difference* function can be used to test whether or not the posterior probability distributions of successive stratigraphic boundaries are significantly different from each other at a given confidence interval. When the *difference* function is applied to adjacent boundaries of two different stratigraphic units in Model 2 (e.g. Unit C – Unit D boundary), it provides a statistical indication of the presence or absence of potential depositional hiatuses (given the available dating evidence). Calculated duration ranges that overlap with 0 at the 95.4% confidence interval suggest that the boundaries of successive units are not separated by a statistically significant temporal hiatus. Calculated duration ranges that do not overlap with 0 at the 95.4% confidence interval indicate potentially missing material and / or a temporal gap between the boundaries of successive units. When the *difference* function is applied to the upper and lower boundaries of the same stratigraphic unit (as opposed to the adjacent boundaries of successive units), a calculated duration of >0 years indicate a statistically significant temporal difference between the onset and termination of the depositional event. In contrast, calculated duration ranges that overlap with 0 indicate statistically indistinguishable onset and termination ages for the depositional event at a given confidence interval.

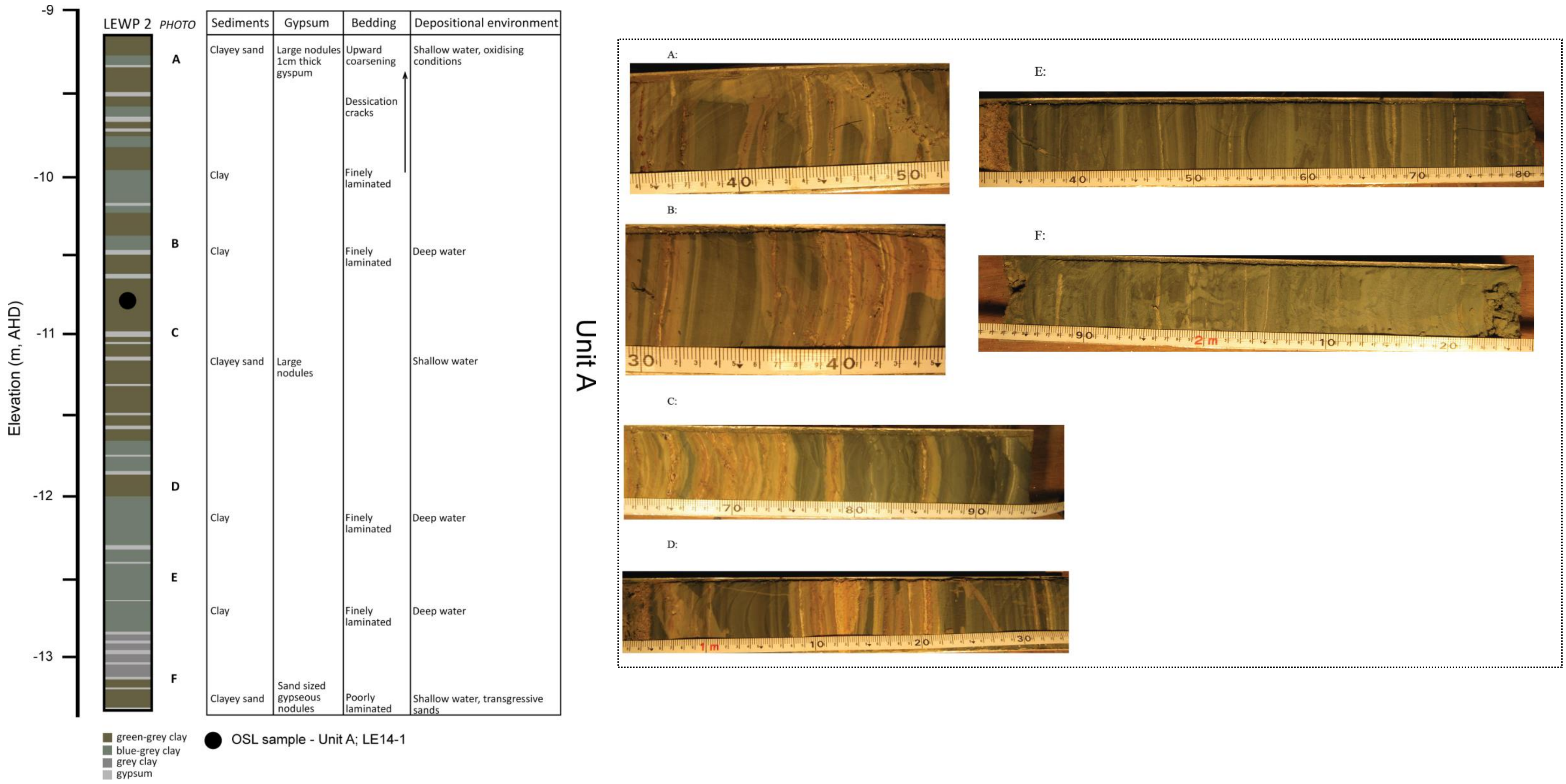


Fig. S1. A schematic sedimentary log of the LEWP2 core and photos of the LEWP2 core. Note that sample LE14-1 was collected from the William Point exposure rather than LEWP2 core. The AHD position of LE14-1 is equal to the black filled circle in the schematic profile.

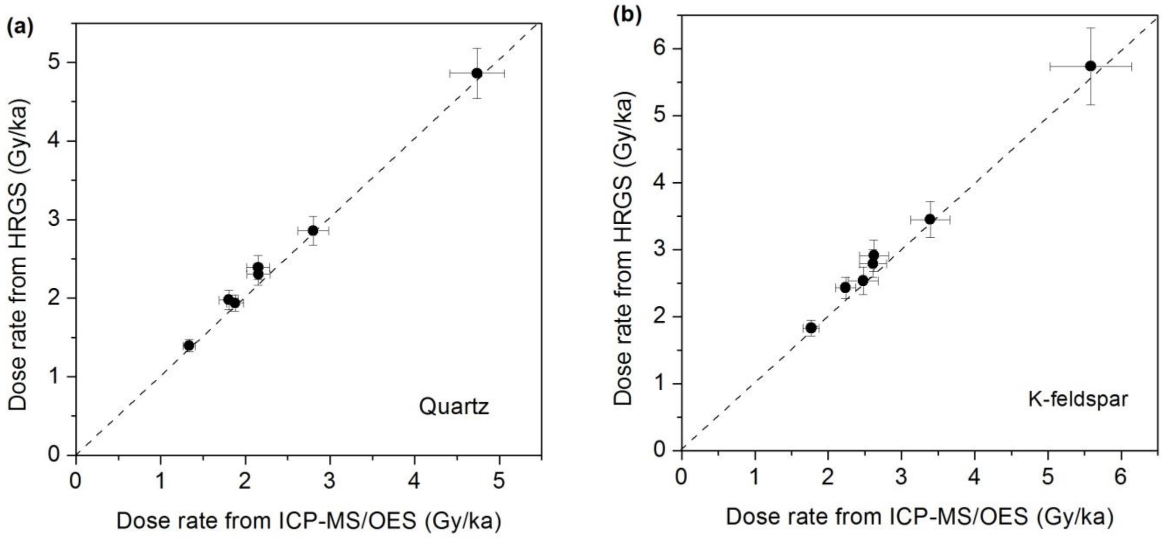


Fig. S2. Comparison of final dose rates (after moisture and grain size attenuations) estimated using the ICP-MS/OES technique and the HRGS technique for quartz (a) and K-feldspar (b) fractions of 7 replicate samples. See details of moisture contents and used grain sized in Table S1.

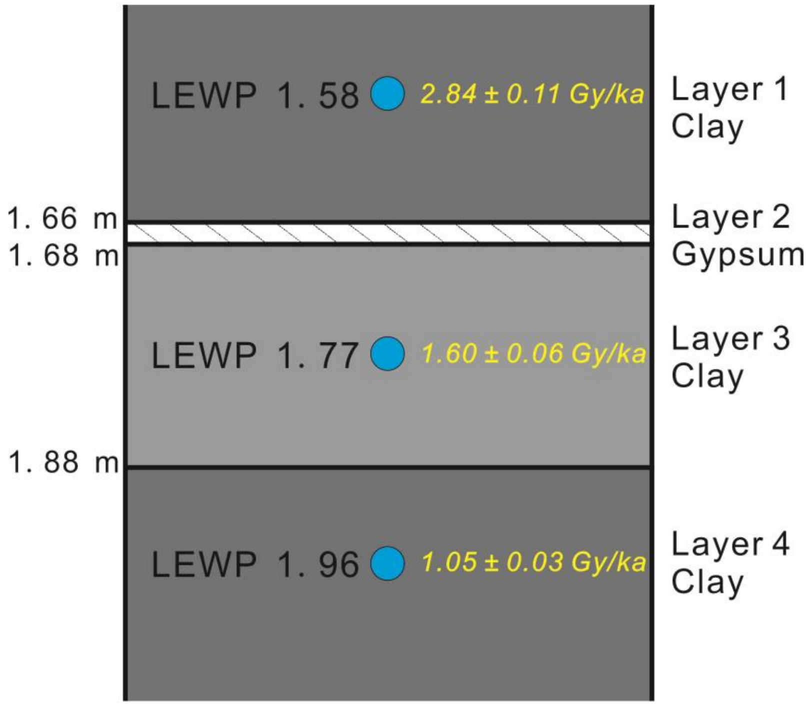


Fig. S3. Schematic figure showing the stratigraphic setting of sample LEWP 1.77. This sample was collected from a position where the gamma dose rate is affected by four sedimentary layers with heterogeneous radioactivity. The numbers on the left show boundary depths of different layers. The yellow numbers show dry gamma dose rates for different samples collected from different layers. The gamma dose rate of sample LEWP 1.77 was revised following Aitken (1985), see details in section S2.2.

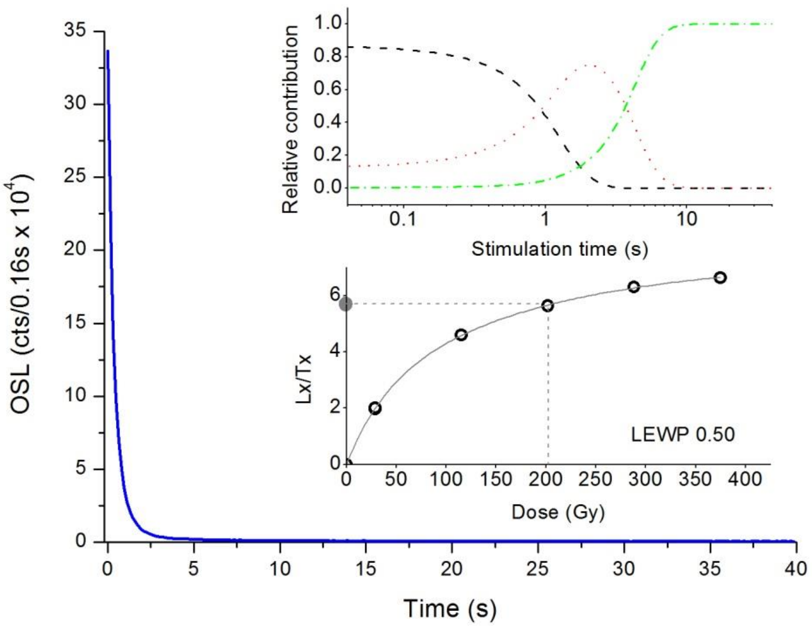


Fig. S4. Natural quartz OSL decay curve for one aliquot of sample LEWP 0.50, which is representative for the LEWP1 core samples. The upper inset shows the relative contribution of the fast (black dashed line), medium (red dotted line) and slow (includes background; green dash-dotted line) components when the decay curve is fitted using a three exponential decay function (note the logarithmic scale for the x-axis). The lower inset shows the corresponding dose response curve of this aliquot. The sensitivity corrected natural signal is plotted on the y-axis.

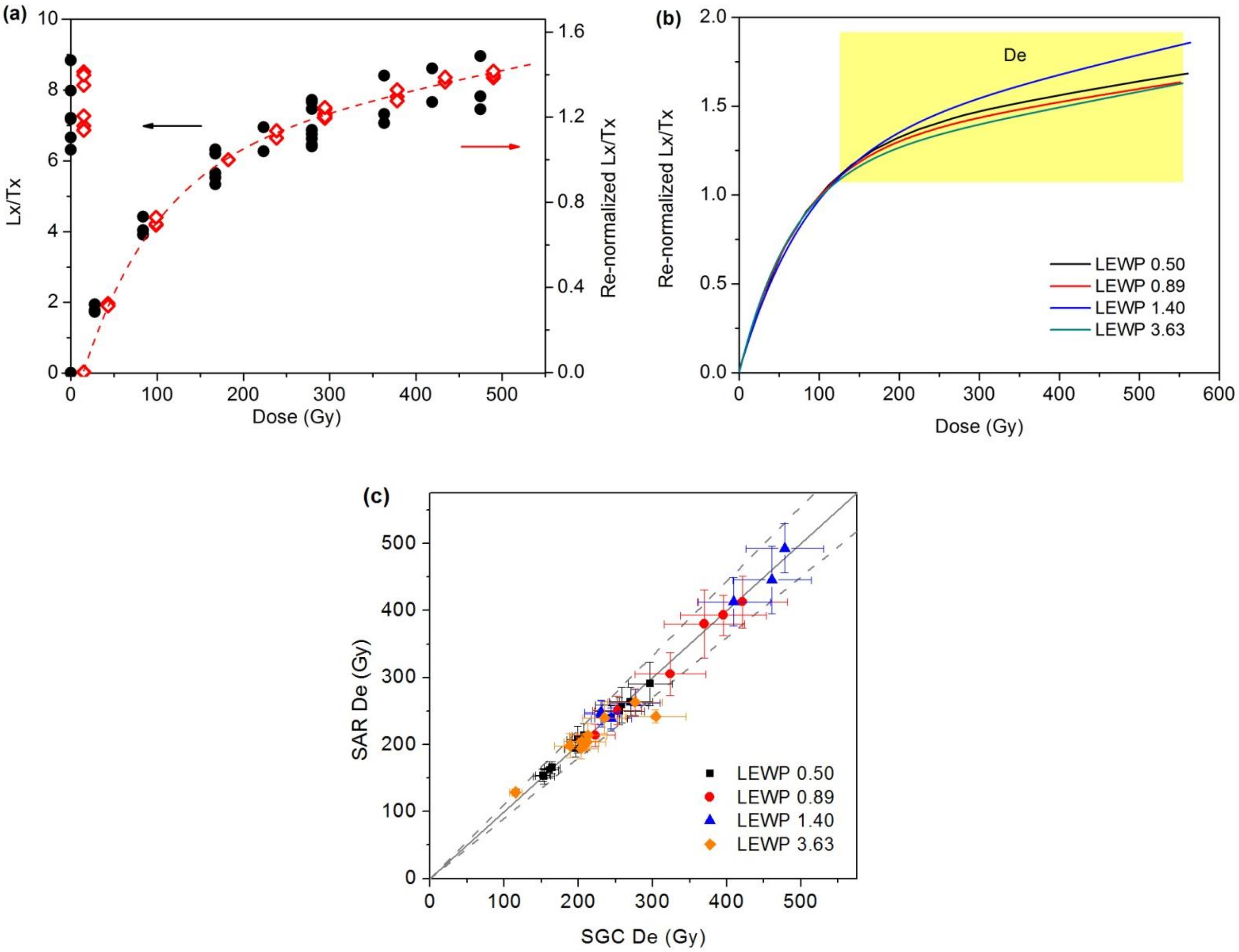


Fig. S5. Performance of the re-normalisation SGC method for single-aliquot quartz OSL dating. (a) Sensitivity corrected natural and regenerative signals of sample LEWP 1.40 before (filled circles) and after (open diamonds) re-normalisation. The latter were calculated using a re-normalisation dose of 168 Gy. The natural signals are plotted on the y-axis. Note that the re-normalised data are offset slightly to the right on the x-axis for clarity. The dashed line is the re-normalised SGC, which is best fitted using an exponential plus linear function. (b) The re-normalised SGCs of four samples from the LEWP1 core. All SGCs are multiplied by a factor that makes the SGCs pass through a value of unity at 100 Gy. This is equal to normalising all SGCs using a regenerative dose signal at 100 Gy. The yellow band indicates the dose range in which the individual $D_e$ values of the four samples lie. (c) A comparison of the $D_e$ values obtained using the SGC method and the full conventional SAR method for 34 aliquots from four samples. The solid line represents the 1:1 line and the dashed lines represent 10% deviation from the 1:1 line.

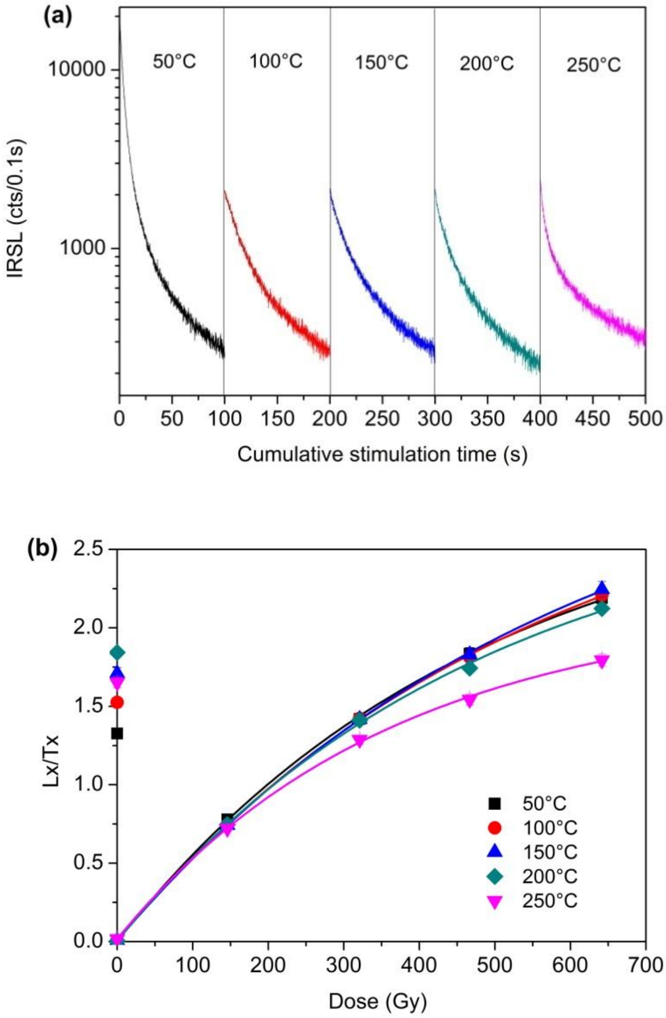


Fig. S6. (a) Natural K-feldspar IRSL and pIRIR decay curves for one aliquot of sample LEWP 0.89, which is representative for the LEWP1 core samples. Before each IRSL measurement, an 'IR-off' period of 10-50 s was applied to avoid any significant interference from isothermal-luminescence signals for the IRSL and pIRIR signals (Fu et al., 2012). (b) Dose response curves corresponding to different signals in (a). The sensitivity corrected natural signals are plotted on the y-axis.

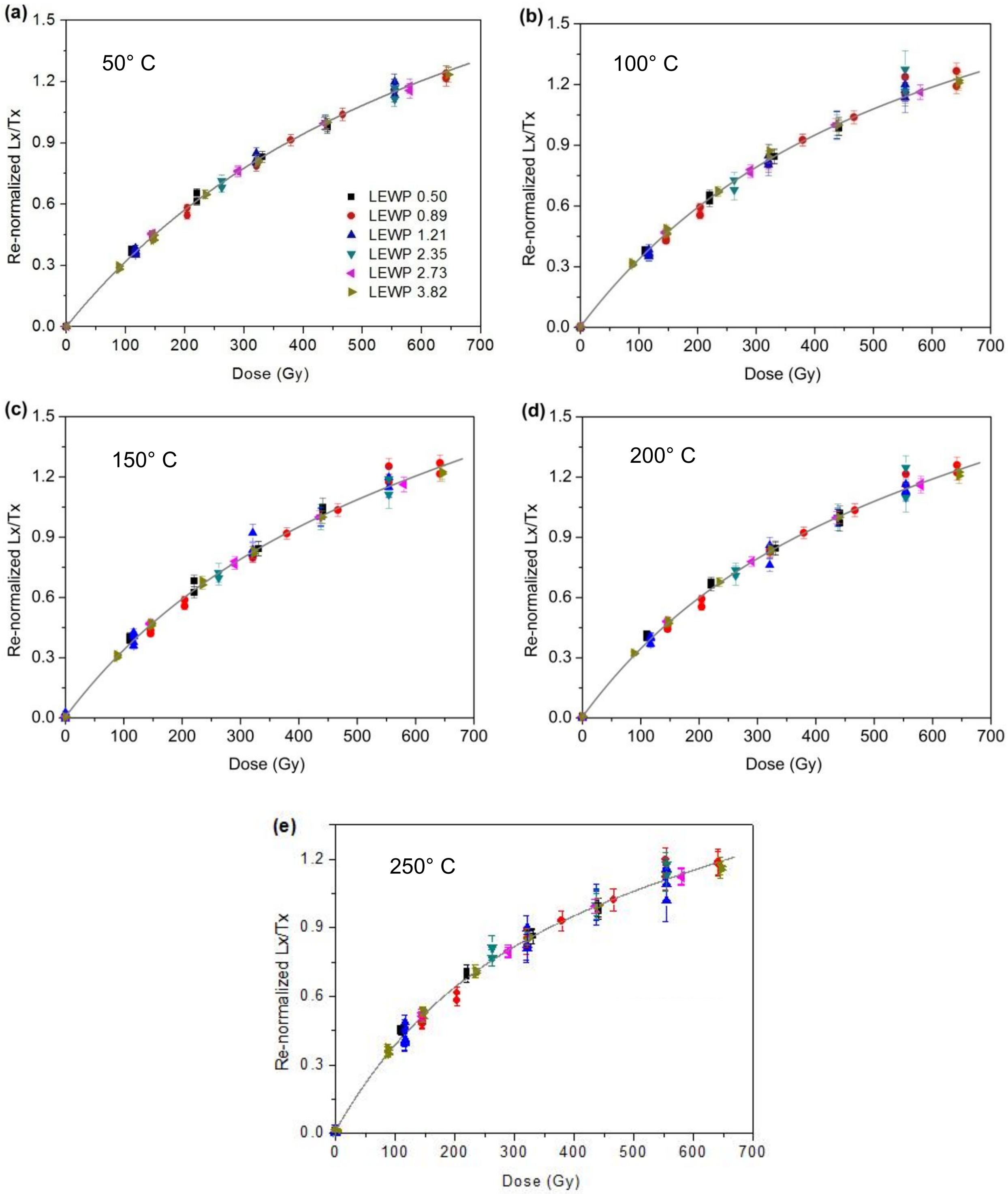


Fig. S7. Re-normalised $IRSL_{50}$ (a), $pIRIR_{100}$ (b), $pIRIR_{150}$ (c), $pIRIR_{200}$ (d) and $pIRIR_{250}$ (e) signals for six LEWP1 core samples. All signals are normalised using a regenerative dose signal at 442 Gy. The solid lines represent common SGCs for different signals, which can be best fitted using an exponential plus linear function.

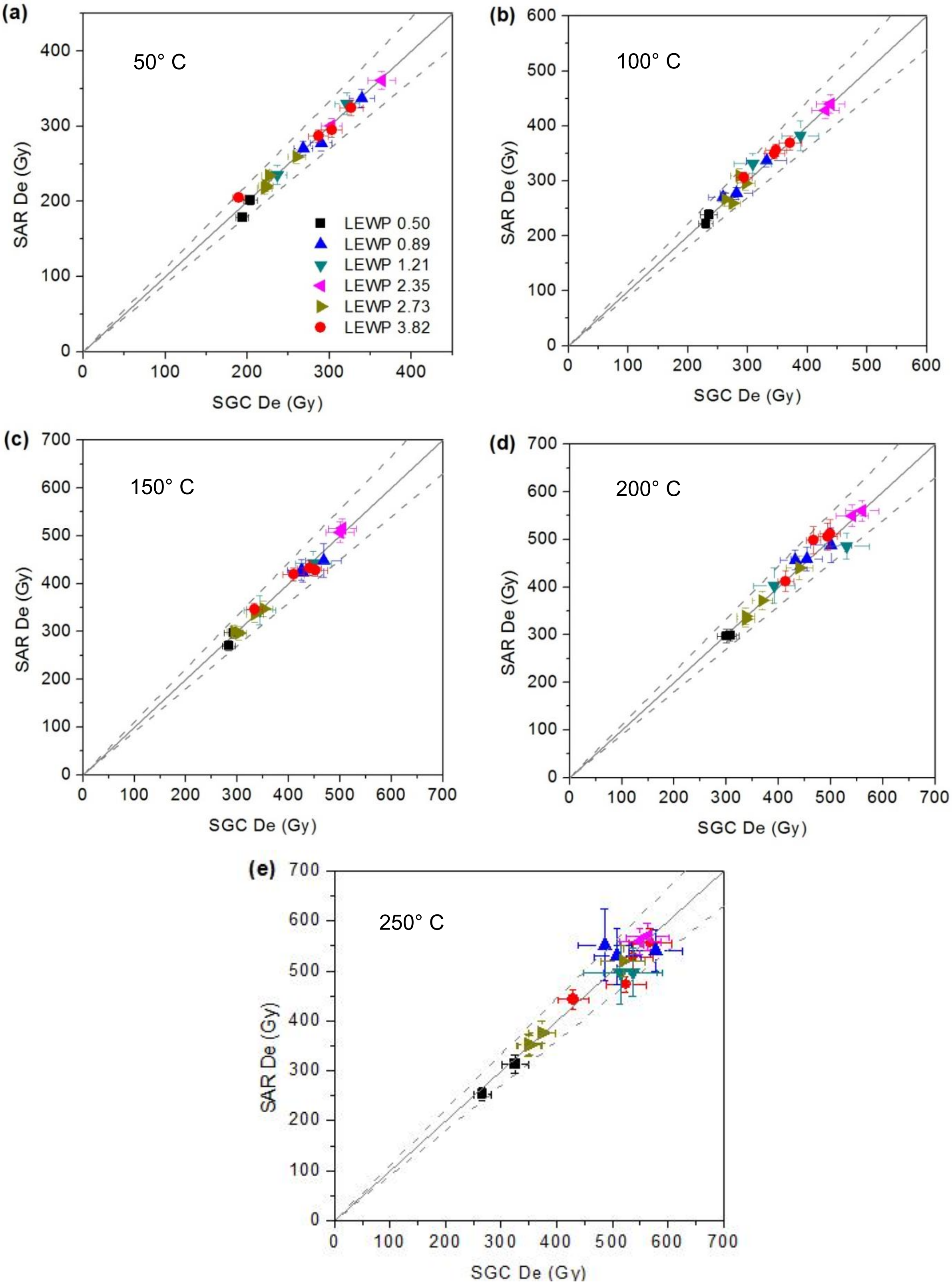


Fig. S8. Comparison of the $IRSL_{50}$ (a), $pIRIR_{100}$ (b), $pIRIR_{150}$ (c), $pIRIR_{200}$ (d) and $pIRIR_{250}$ (e) $D_e$ values for 17 aliquots of six samples obtained using the re-normalisation SGC method and the full MET-pIRIR method. The solid line represents the 1:1 line and the dashed lines represent 10% deviation from the 1:1 line.

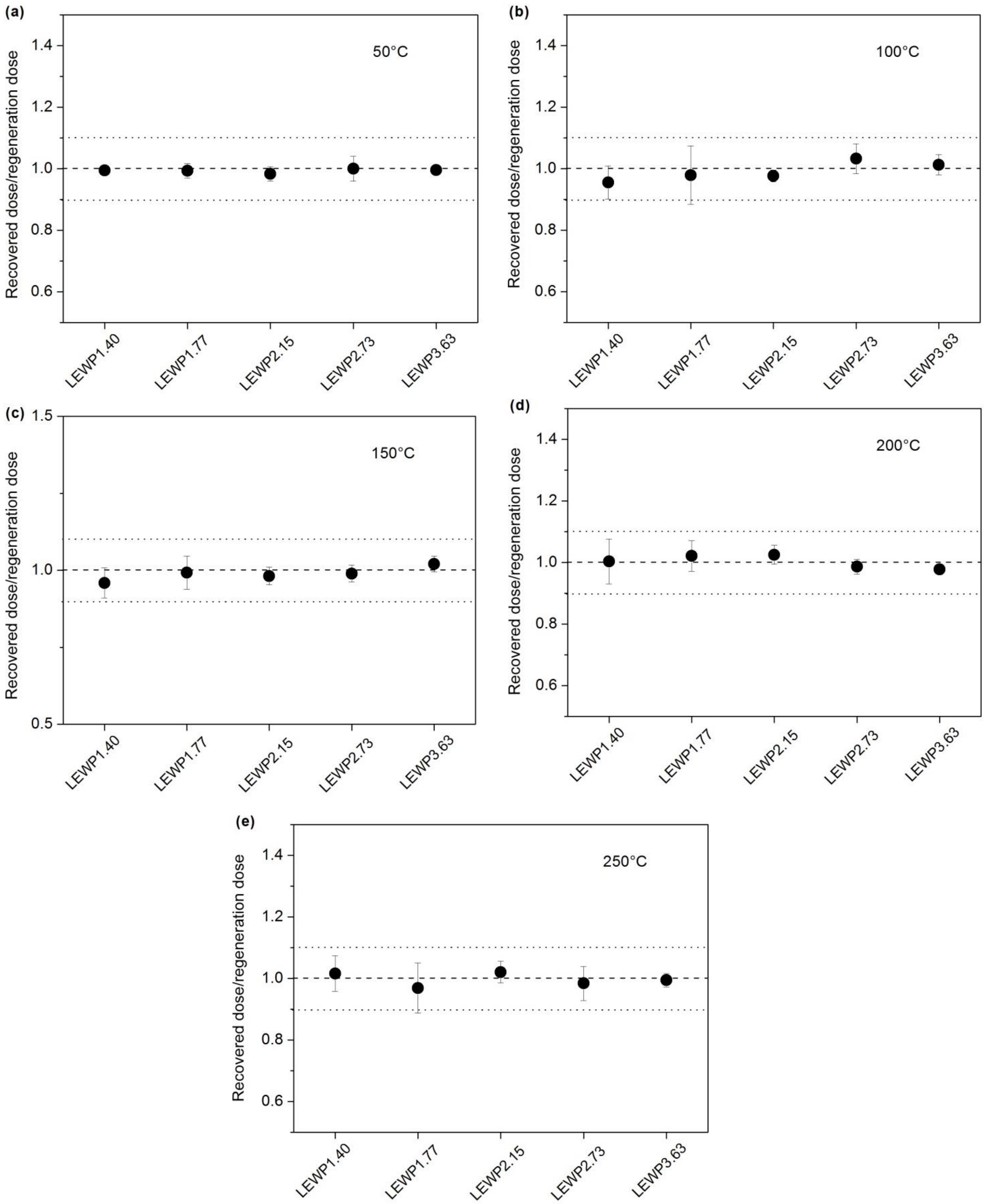


Fig. S9. Regenerative dose recovery test results for five LEWP1 core samples measured using the MET-pIRIR procedure and the re-normalisation method. (a) $IRSL_{50}$ signal; (b) $pIRIR_{100}$ signal; (c) $pIRIR_{150}$ signal; (d) $pIRIR_{200}$ signal and (e) $pIRIR_{250}$ signal. Individual data points (black circles) each represent the average of 3-6 aliquot measurements. See experimental details in section S3.2.

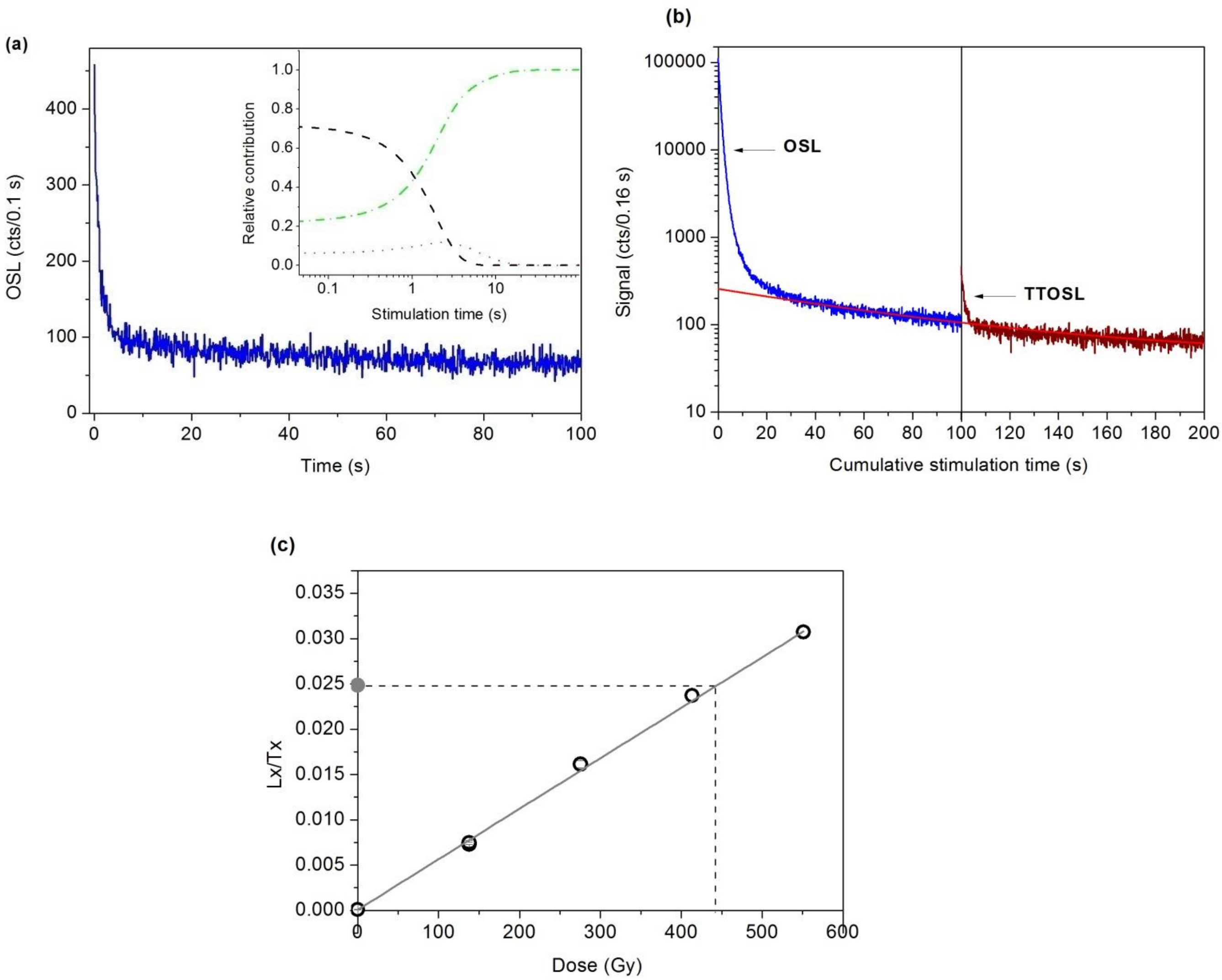


Fig.S10. (a) Natural single-aliquot TT-OSL decay curve for one aliquot of sample LEWP 0.89, which is representative for the LEWP1 core samples. The inset shows the relative contribution of the fast (black dashed line), medium (red dotted line) and slow (includes background; green dash-dotted line) components when the decay curve is fitted using a three exponential decay function (note the logarithmic scale for the x-axis). (b) A comparison of natural OSL decay curve and TT-OSL decay curve for the same aliquot shown in (a) (note the logarithmic scale for the y-axis). The x-axis is the cumulative blue-light stimulation time rather than the real measurement time. The red line indicates the decay of the slow component of the OSL signal which underlies the following TT-OSL signal. This inherited signal forms a major part of the slow component for the TT-OSL signal; hence it has been removed by subtracting a background evaluated from the last 2 seconds of the previous OSL decay curve (see section S3.3). (c) TT-OSL dose response curve of the same aliquot shown in (a) and (b). The sensitivity corrected natural signal is plotted on the y-axis.

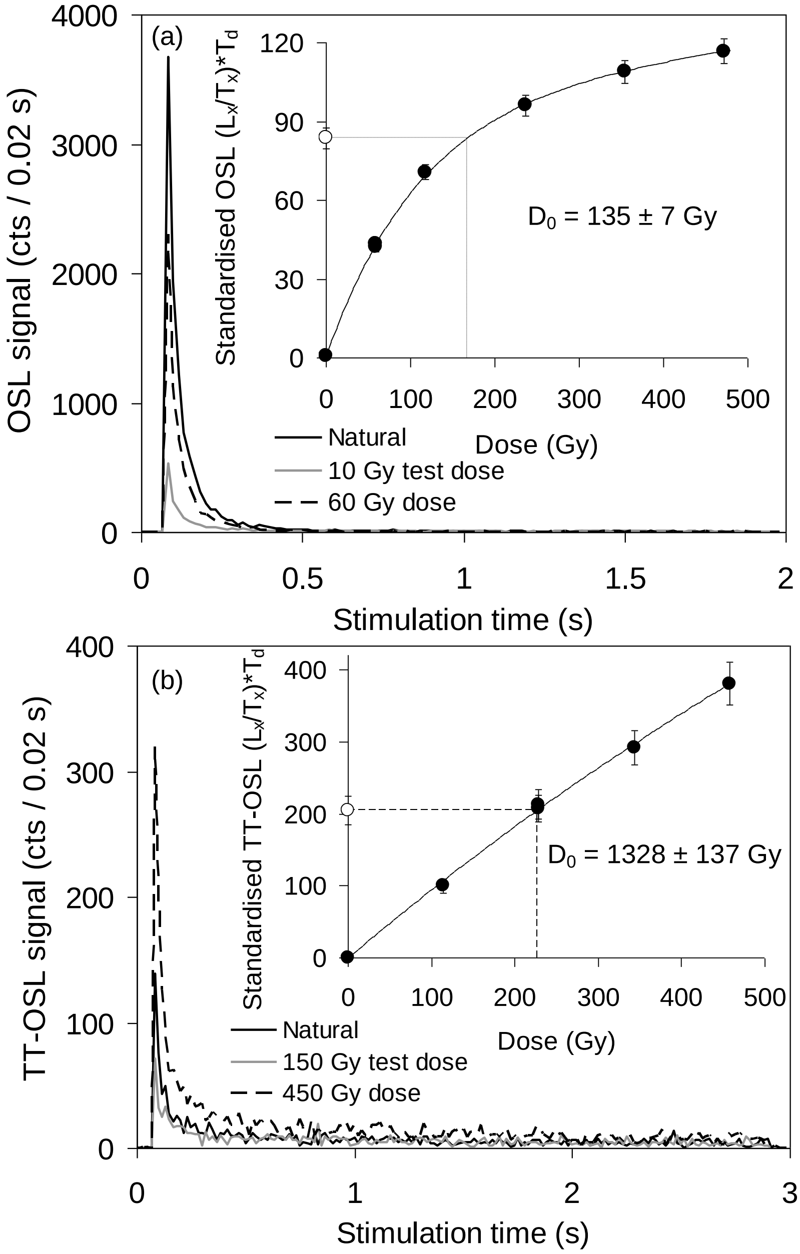


Fig. S11. Representative OSL and TT-OSL decay and dose-response curves for individual quartz grains from LE14-1. (a) Quartz grain from sample LE14-1 with typical OSL signal brightness ($T_n$ intensity = ~1350 counts / 0.17 s / 10 Gy), decay shape and dose-response curve saturation properties. (b) Quartz grain from sample LE14-1 with typical TT-OSL signal brightness ($T_n$ intensity = ~350 counts / 0.17 s / 150 Gy), decay shape and dose-response curve saturation properties. The $D_0$ value characterises the rate of signal saturation with respect to administered dose and equates to the dose value for which the dose-response curve slope is 1/e (or ~0.37) of its initial value. The $D_0$ values shown here have been calculated using a single saturating exponential dose-response curve fitting function.

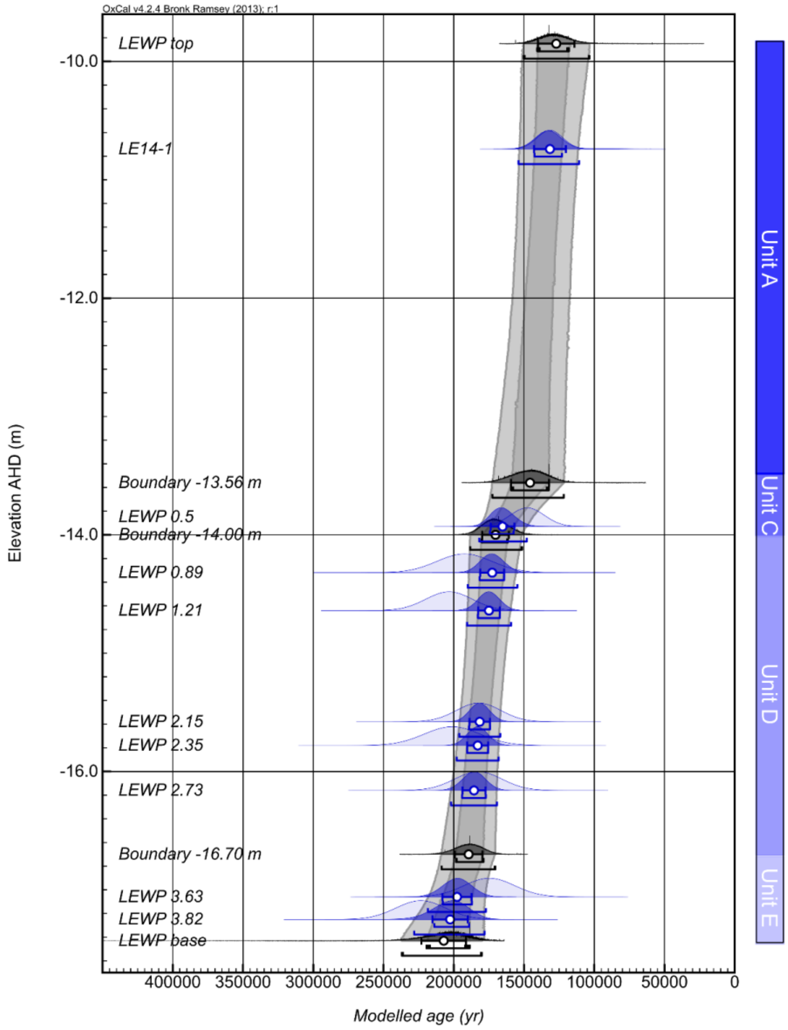


Fig. S12. Bayesian age-depth modelling results for the Lake Eyre Williams Point sequence obtained using a continuous deposition modelling scenario (Model 1, see section 5.2 in the main text). The likelihoods are based on the pIRIR dating results of eight core samples from LEWP1 (excluding three samples that exhibit potentially complicated dosimetry results) and the combined (weighted mean) single-grain OSL and TT-OSL ages of sample LE14-1 from the base of the Williams Point outcrop. The right-hand column shows the boundaries of different sedimentary units (see Fig. 3 and Table 1 in the main text). The prior age distributions for the dating samples (likelihoods) are shown in light blue. The modelled posterior distributions for the dating sample and unit boundaries are shown in dark blue and grey, respectively. Likelihood and posterior ages are shown on a calendar year timescale and are both expressed in years before sample collection (AD2014). The white circles and associated error bars represent the mean ages and 1σ uncertainty ranges of the PDFs. The 68.2% and 95.4% ranges of the posterior probabilities are indicated by the horizontal bars underneath the PDFs.